U.PORTO

FEUP FACULDADE DE ENGENHARIA
UNIVERSIDADE DO PORTO

Micro-mechanical modeling of interlaminar crack propagation

Luís Filipe Tavares Portela Vasques Varandas

Supervisor:
Dr. Nuno André Curado Mateus Correia

Co-Supervisor:
Prof. Dr. António Torres Marques

A Thesis submitted for the degree of
Master of Science in Mechanical Engineering
to the Faculty of Engineering, University of Porto

Porto, July 2016

Abstract

Keywords: Composites, micro-mechanics, representative volume element (RVE), homogenization, hybrid-modeling, delamination, fiber-matrix interface, crack, fracture, deflection.

Composite materials are replacing standard engineering metals and alloys for many applications. Fiber-reinforced polymers, for their inherent ability to be custom tailored for any application, are a very viable material option. Their superior specific strength, stiffness and thermal characteristics have made them very competitive in the aerospace industry.

While properties in the plane of the fibrous reinforcements are strong, stiff, and tailorable, the interlaminar region is relatively weak and compliant, leading to failure due to delamination and other damage modes, thus being the interlaminar fracture toughness the primary limitation of fiber reinforced composites. Delamination failures are common due to the nature of composite construction. A variety of manufacturing techniques are available to make composites. Generally, all these methods employ a layered stacking of fiber-reinforced polymers in a primary plane. The interface between these layers is typically not reinforced with fibers and is the source of delamination or interlaminar fracture. Porosity and other manufacturing related defects also introduce nucleation sites for delamination.

This thesis aims to increase the understanding of the interlaminar failure of uni- and multi-directional composites in single- and mixed-mode delamination. To achieve this goal several models with increasing complexity have been developed and implemented. A three-dimensional computational micro-mechanics framework, with a special focus on the elastic-plastic and damage constitutive behaviors of the matrix and on the response of the fibre-matrix interface, is used in the present analysis.

Since the objective is to model interlaminar fracture mechanisms, the fibrous reinforcements are assumed to be linear-elastic and a thermo-visco-plastic model is implemented to simulate the mechanical behavior of the matrix, based on experimental evidence. Failure of the matrix is modeled using a damage evolution law developed in the framework of thermodynamics of admissible processes.

Representative volume elements (RVEs) with random fiber distributions were created by an algorithm developed to study the sequence of mechanisms leading to interlaminar failure in composite materials and to validate the implemented models. These RVEs are representative of the reinforcements and of the matrix at the

micro-scale of the composite, capable of modeling laminates with different stacking orientations. This model was combined with homogenized meso-scale parts, forming a hybrid model that represents different experimental tests, such as the double cantilever beam, end notched flexure and mixed mode bending.

The models were implemented in a commercial finite element software. In order to validate the models, an Explicit analysis was performed to observe the propagation of damage along the matrix in the RVE.

Resumo

Palavras-chave: Compósitos, micromecânica, elemento representativo de volume (ERV), homogenização, modelos híbridos, delaminagem, interface fibra-matriz, fratura.

Graças à sua capacidade de customização, os materiais compósitos têm vindo a substituir os metais (e ligas relacionadas) nas mais variadas aplicações, tendo-se vindo a destacar o uso de compósitos de matriz polimérica reforçados por fibras contínuas. Estes tornaram-se bastante competitivos na indústria aeroespacial devido à sua elavada resistência específica, rigidez e caracteristicas térmicas.

Apesar destes compósitos avançados apresentarem boas propriedades mecânicas, a zona entre camadas, i.e., a zona interlaminar é relativamente fraca. A tenacidade interlaminar é por isso um dos parâmetros mais limitantes deste tipo de material. Falhas por delaminagem são também comuns devido aos processos de fabrico dos materiais compósitos. Para além destes processos envolverem o empilhamento de diversas camadas entre as quais não existe reforço, a porosidade e outros defeitos de fabrico podem também levar à delaminagem.

O objetivo deste trabalho é aumentar o conhecimento dos processos de fratura interlaminar em compósitos unidirecionais e multidirecionais em modo simples ou misto. Para isso, foi desenvolvido ao nível tridimensional um modelo computacional micromecânico com uma atenção especial ao comportamento elasto-plástico e de dano da matriz polimérica. A análise da interface fibra-matriz foi também tida em conta.

Dado que o objetivo é simular mecanismos de fratura interlaminar, assume-se que as fibras têm um comportamento linear-elástico. De maneira a simular o comportamento da matriz polimérica, é implementado um modelo termo-visco-plástico com fortes bases em evidência experimental.

Durante a elaboração desta tese foi desenvolvido um algoritmo que permite criar elementos de volume representativos (ERVs) com distribuições de fibras aleatórias. Desta maneira, é possível estudar diversos mecanismos de falha interlaminar neste tipo de materiais. Estes ERVs descrevem, ao nível microscópico, as heterogeneidades do material e são capazes de representar camadas de laminados com diferentes orientações. Juntou-se a este modelo micromecânico um modelo homogeneizado à escala meso, constituindo assim um modelo híbrido. Desta maneira, o modelo em causa consegue representar diferentes testes experimentais para avaliar a tenacidade do material, tais como o *double cantilever beam*, *end notched flexure* e *mixed mode bending*.

Os modelos em causa foram desenvolvidos e implementados num *software* comercial de elementos finitos. De maneira a validar os modelos, foi feita uma análise Explícita que é capaz de modelar a propagação do dano interlaminar na matriz.

Acknowledgements

I take this opportunity to express my gratitude to my co-supervisor, Dr. Nuno André Curado Mateus Correia, for the opportunity to develop my MSc thesis in such an interesting field and for giving me all the best conditions to work at INEGI.

To Dr. Giuseppe Catalanotti, for his help, encouragement and attention that he gave me during the development of this thesis and for providing me all of his knowledge, that without it, nothing of this would be possible. For giving me all the support and guidance when I didn't even know what I was doing.

To Dr. Albertino Arteiro, for all his time spent on the review of this thesis and for teaching me all the tricky aspects of the software that was used throughout the development of the thesis.

To Masoud Bodaghi, PhD candidate, who gave me the initial insight about the thematics of my study and for always being available to discuss any topic, usually over a cup of coffee.

To all my friends that I made during college. A special thanks to Miguel Carvalho for all the valuable discussions and for the unique perspectives, to Tomás Chuaqui for making these past five years a much easier journey and to Marco Alves for the good company and for always having the will to share his knowledge with everyone. To Sílvia Tavares that, despite not being present during the development of this thesis, was always there to support me during the time passed. To Mariana Soares for making tiresome moments the most joyful. Thank you all for the unforgettable moments.

To my longtime friends Francisco Santos, Daniel Moura, Jorge Pereira, Mark Botros and cousin Pedro Varandas for having the ability of making me escape the constant feeling of responsibility.

Finally, I want to dedicate all my work that I have done throughout this past five years to all my family with a special focus to my parents, journey that would not be possible to be taken without their support. To my father for providing me all the best interests and knowledge. To my mother for having the patience and will to take good care of me when I most needed. Thank you both for acknowledging everything that I have done during my entire life.

I also gratefully acknowledge the funding of Project DRONES SAFE FLIGHT, financed by LAETA the Associated Laboratory of Space, Transports and Aeronautics, through the multiannual funding to the laboratory supported by the National Foundation for Science and Technology (FCT) and Project NORTE-01-0145-FEDER-000022 - SciTech - Science and Technology for Competitive and Sustainable Industries, cofinanced by Portuguese North Operational Programme (NORTE2020), through the European Social Fund (ESF).

Contents

List of Symbols

Chapter 2

a	Crack length;
a_{eq}	Equivalent crack length;
$\mathcal{G}$	Energy release rate;
$\mathcal{G}_I^m$	Mode I energy release rate in the MMB test;
$\mathcal{G}_{II}^m$	Mode II energy release rate in the MMB test;
$\mathcal{G}_T^m$	Total energy release rate in the MMB test;
$\mathcal{G}_{_C}$	Critical energy release rate or fracture toughness;
$\mathcal{G}_{I_C}$	Mode I fracture toughness;
$\mathcal{G}_{II_C}$	Mode II fracture toughness;
$\mathcal{G}_{III_C}$	Mode III fracture toughness;
u	Axial displacement in the x direction;
v	Axial displacement in the y direction;
w	Axial displacement in the z direction;
$\langle \boldsymbol{\varepsilon} \rangle$	Macroscopic gradient of strain;
$\langle \boldsymbol{\sigma} \rangle$	Macroscopic gradient of stress;
$\boldsymbol{\varepsilon}'(x)$	Microscopic field of strain;
$\boldsymbol{\sigma}'(x)$	Microscopic field of stress;
$\langle \boldsymbol{\sigma}' \rangle$	Volume average of microscopic fluctuations of strain;
$\langle \boldsymbol{\varepsilon}' \rangle$	Volume average of microscopic fluctuations of strain;
$f(x)$	Some variable;
$\langle f \rangle$	Volume average of some variable;
E	Young's modulus;
E_f	Flexural Young modulus;
G	Shear modulus;
ν	Poisson's ratio;
b	Width of the specimen;
h	Height of the specimen;
L	Length of the specimen;
P	Applied load;
$P_{_C}$	Critical load;
C	Compliance;
C_0	Initial compliance;
c	Load distance;
δ	Displacement at a loading point;
L_{inh}	Size of the inhomogeneities;
L_{RVE}	Characteristic size of the RVE;

L_{macro}	Size of the macroscopic domain;
Ω_s	Volume of the region under consideration;
Γ_s	Surface of the region under consideration;
$\mathbf{u}(x)$	Deformation vector;
$\mathbf{t}(x)$	Surface traction vector;
$\mathbf{n}_\Gamma(x)$	Surface normal vector;
$\boldsymbol{D}$	Elastic tensor;
$\boldsymbol{D}^*$	Effective elastic tensor;
$\boldsymbol{H}$	Compliance tensor;
$\boldsymbol{H}^*$	Effective compliance tensor;
E_A^*	Axial effective Young modulus;
E_T^*	Transverse effective Young modulus;
ν_A^*	Axial effective Poisson's ratio;
ν_T^*	Transverse effective Poisson's ratio;
K_T^*	Effective transverse (plane strain) bulk modulus;
v_f	Fiber volume fraction;
d	Damage variable;
$\mathbf{t}$	Nominal traction stress vector;
τ_1	Out of plane shear traction;
τ_2	In plane shear traction;
τ_3	Normal traction;
τ_1^0	Out of plane interface maximum strength;
τ_2^0	In plane interface maximum strength;
τ_3^0	Normal interface maximum strength;
δ_1	Out of plane shear separation;
δ_2	In plane shear separation;
δ_3	Normal separation;
δ_1^0	Out of plane interface maximum separation;
δ_2^0	In plane interface maximum separation;
δ_3^0	Normal interface maximum separation;
δ_m	Effective separation;
δ_m^f	Effective separation at complete failure;
δ_m^0	Effective separation at the initiation of damage;
δ_m^{max}	Maximum effective separation attained during loading history;
δ_m^{1f}	E. separation at complete failure considering normal traction;
δ_m^{2f}	E. separation at complete failure considering first shear traction;
δ_m^{3f}	E. separation at complete failure considering second shear traction;
$\boldsymbol{K}$	Interface stiffness tensor;
T_{eff}^0	Effective traction at damage initiation;
$\mathcal{G}_0$	Elastic energy release rate at damage initiation;
β	Rate of damage evolution;
η	Mixed-mode interaction parameter;

Chapter 3

r	Radius of a fiber;
H	Width of the RVE;
E	Real width of the RVE;
h	Heigth of the RVE;
DE	Extrusion depth of the RVE;
$rotation$	Variable that defines the orientation of the ply;
$\boldsymbol{v}_i^{mn}$	Bi-dimensional coordinates of a fiber inside of the Compact RVE;
$\bar{\boldsymbol{v}}_i^{mn}$	Bi-dimensional coordinates of a fiber inside of the Initial RVE;
$\bar{\bar{\boldsymbol{v}}}_i^{mn}$	Bi-dimensional coordinates of a fiber inside of the Final RVE;
M	Number of fibers in the x direction inside the Compact RVE;
N	Number of fibers in the y direction inside the Compact RVE;
Np_{trial}	Initial number of fibers that are in the Compact RVE;
Np	Number of fibers that are in the Compact RVE;
f_x	Correction factor for the x direction;
f_y	Correction factor for the y direction;
K	Times that the "perturbation" process is iterated;
$\mathbf{u}$	Displacement that the fibers are submitted;
ρ	Radial coordinate of the displacement;
$\bar{\rho}$	Initial radial coordinate of the displacement to start the algorithm;
ρ_{max}	Maximum input value of the radial coordinate of the displacement;
$\Delta\rho$	Increment of the displacement;
θ	Azimuthal angle;
d_{ij}	Euclidean distance between fibers;
a	Variable defined according to Figure 3.21;
b	Variable defined according to Figure 3.21;
num_lines	Number of fibers inside the Final RVE;
dcb_depth	Extrusion depth of the homogenized parts;

Chapter 4

$\boldsymbol{\sigma}$	Stress tensor;
$\tilde{\boldsymbol{\sigma}}$	Tensile load applied to the material;
σ_{Y_C}	Compressive yield strength;
σ_{Y_T}	Tensile yield strength;
σ_{Y_S}	Shear yield strength;
σ_{vm}	Von Mises equivalent stress;
$\boldsymbol{\varepsilon}$	Strain tensor;
$\boldsymbol{\varepsilon}^e$	Elastic strain tensor;
$\boldsymbol{\varepsilon}^p$	Plastic strain tensor;
$\boldsymbol{\varepsilon}_d^e$	Elastic deviatoric strain tensor;
$\boldsymbol{\varepsilon}_e^p$	Equivalent plastic strain;
ε_ν^e	Elastic volumetric strain;
$\boldsymbol{D}^e$	Elasticity fourth order tensor;
$\boldsymbol{S}$	Deviatoric stress tensor;
p	Hydrostatic stress;
E_m	Matrix Young modulus;

ν_m Matrix Poisson's ratio;
G_m Matrix shear modulus;
d_m Damage variable defined for the matrix;
K Bulk modulus;
$\mathscr{G}$ Deformation energy;
$\mathscr{G}_p$ Plastic deformation energy
$\boldsymbol{I}$ Identity matrix;
I_1 First stress invariant;
J_2 Second invariant of the deviatoric stress tensor;
J_3 Third invariant of the deviatoric stress tensor;
$\boldsymbol{I}_4$ Fourth-order tensor defined in Equation (4.35);
a Interdependent parameter defined in Equation (4.10);
b Interdependent parameter defined in Equation (4.11);
α Parameter that defines the volumetric component of the plastic flow;
$\Delta\lambda$ Plastic multiplier;
T Temperature;
$\boldsymbol{H}_m$ Compliance tensor of the matrix;
$\boldsymbol{H}_m^0$ Compliance tensor of the undamaged matrix;
$\boldsymbol{C}_m$ Stiffness tensor of the matrix;
$\boldsymbol{C}_m^0$ Undamaged stiffness tensor of the matrix;
G_d Parameter defined in Equation (4.24);
λ_d Parameter defined in Equation (4.24);
F_m^d Damage activation function;
ϕ_m^d Loading function;
r_m Internal variable defined according to the damage variable;
X_m^c Matrix compressive strength;
X_m^c Matrix tensile strength;
$\tilde{J}_2$ Invariant that is determined using the effective stress tensor;
$\tilde{I}_1$ Invariant that is determined using the effective stress tensor;
Ξ_m Rate of energy dissipation per unit volume;
Ψ_m Amputated dissipated energy of the matrix;
$\mathcal{G}_m$ Energy release rate of the matrix;
l^e Characteristic element length;
Y_m Complementary free energy of the matrix;
A_m Parameter that needs to be computed from solving Equation (4.30);
$(\cdot)_p$ Quantity that is in the plane of isotropy;
$(\cdot)_t$ Quantity that is transversal to the plane of isotropy;
Δ Determinant of the stiffness matrix;
K Interface stiffness;

Chapter 5

ρ Density of the material;
μ_τ Interface friction coefficient;
Δ Applied displacement;
d_r Relative displacement;

List of Figures

List of Tables

Chapter 1

Introduction

1.1 Background

Advanced composite materials are becoming increasingly used in the critical structures of both civilian and military aircraft, as they often have a higher strength-to-weight ratio compared to conventional materials, are corrosion resistant and are able to be tailored to meet specific mechanical criteria. Under severe loading conditions, composite materials are often vulnerable to interlaminar fracture. Interlaminar fracture occurs when the plies or layers separate due to the applied loading condition, potentiated by the presence of voids, pores or other small defects between layers.

The interlaminar fracture toughness of a composite is generally thought to be resin-dominated. Epoxy systems are used with carbon fibers to build advanced composites that are usually considered the best performing. Although the contribution of the fibers to the interlaminar fracture toughness is very small, it is not completely negligible. Alternating the orientation of the fiber layers provides mechanical interlocking from layer to layer and restricts delamination propagation (Cook, 2001).

Historically, delamination in composite laminates has been treated as an individual damage mechanism. Numerous test methods have been developed for characterizing delamination. The majority of these methods have common features such as enforcement of delamination initiation and growth at a single unidirectional ply interface and the use of the critical energy release rate for defining a laminate's interlaminar fracture toughness (Andersons and Konig, 2004). This has led to several testing standards for characterizing delamination under quasi-static and cyclic loading conditions. Analysis methods have been developed based on linear-elastic fracture mechanics and these combined efforts have led to significant advances towards a practical means for assessing the damage tolerance of composite structures from a fracture mechanics perspective.

Failure of composite structures involving delamination, however, typically involves multiple delamination cracks, which often grow, propagate, deflect around the fibers, or migrate into different ply interfaces (delamination relocation). This propagation of damage can also induce the debonding between the fibers and the matrix.

Deflection of matrix cracks at the fiber-matrix interface depends on the relative strengths of the matrix, fibers and interface, as well as on the bonding characteristics between the constituent layers. Several approaches have been proposed to estimate the conditions of crack propagation versus deflection. A often cited approach proposed by Ming-Yuan He and Hutchinson (1988) employs traditional fracture mechanics to define a criterion for crack deflection at the fiber-matrix interface in an isotropic material according to $\frac{\mathcal{G}_d}{\mathcal{G}_p} \leq \frac{\Gamma_i}{\Gamma_f}$ where, $\mathcal{G}_d$ and $\mathcal{G}_p$ are the energy release rates for deflection and propagation and Γ_f and Γ_i are the critical energy release rates or surface energies for the fiber and for a deflecting crack at the interface between two semi-infinite planes with traction free boundary conditions. Several authors analyzed and modified the previous approach and were successful, however, none of the approaches, for crack deflection, consider an interface of finite thickness. A few studies have demonstrated that a finite interface can have a significant influence on the overall response (e.g. Martin et al. (1998) and Parthasarathy et al. (2007)). Studies for a secondary debonding or cracking in the interface or at interface boundaries in many materials were made by several authors. Pagano and Brown (1993), for example, simulated cracking with and without the secondary cracking or interfacial debonding mechanism and predicted much higher energy release rates in the case of debonding of the interface ahead of the crack tip.

The crack migration mechanism has been documented in several cases, including low-velocity impact, skin/stiffener debonding, delamination growth from notches and multidirectional laminates under shear. Many methods such as the finite element method may provide a practical means of simulating damage mechanisms such as delamination migration, however it is necessary to know the fundamental driving mechanisms for delamination propagation and migration at multidirectional ply interfaces. In the literature, two different mechanisms leading to perceived delamination relocation to a different ply interface are described. In various studies (e.g. Hallett et al. (2009)), delamination was observed to propagate through the thickness of a laminate by migrating through pre-existing ply splits, and in other studies (e.g. Greenhalgh et al. (2009)) it was reported that the delamination relocated to other interfaces. In this last mechanism, delamination "kinks out" of the original interface into one of the adjacent plies, without the necessary presence of pre-existing ply splits. Delamination kinking, and subsequent migration, can be explained by the micro-mechanism of crack formation leading to delamination, where the term "kinking" refers to the passage of delamination from a ply to its subsequent and "migration" refers to the complete process of thecrack relocation from its current interface to another. Under pure shear or mixed-mode loading conditions, the resolved tensile stress is oriented out of the laminate plane. Consequently, the microcracks are angled with respect to the laminate plane and the resulting delamination tends to propagate out of the plane of the interface, through the thickness of a laminate. The orientation of the resolved tensile stress at the delamination front determines into which of the adjacent plies the microcracks are driven towards. If the fiber orientation in this ply precludes containment of the microcracks, migration occurs. If, instead, the fibers are aligned and can block intralaminar fracture, then delamination stays at the interface, and propagates along the fiber direction (He et al., 1991). For a deeper analysis on the experimental study on delamination migration in composite laminates, the reader is referred to Pernice et al. (2015).

Another issue in delamination can be the debonding between the fiber and matrix interface. This interface is the key region which determines, to a great extent, the set of properties of all heterogeneous systems, including composite materials. In a composite material, the fibers ensure the strength of the material, while the matrix ensures load transferring between the fibers and keeps the shape of the part. The interface, as a key element of the composite, transfers the load from the matrix to the fibers, providing them with the required stability.

In recent years, experimental methods for measuring the adhesion between a rigid fiber and a more ductile polymer matrix have been progressively developed, and intensively investigated. Currently, several micro-mechanical techniques exist, such as the single-fiber composite (or fragmentation) test (Zhandarov et al., 1992), the microbond test (Miller et al., 1987), the fiber-pull out test (Alberti et al., 2016), and the microindentation test (Yuan et al., 2014). Wagner and Lustiger (1994) have presented an energy balance scheme for the analysis of the initial interfacial debonding that arises as fibers progressively begin to break during the fragmentation test, but they neglected to include the likely contribution of the matrix in their energy balance scheme, and, moreover, the fiber stress profile in the build-up region around the fiber break was assumed, for simplicity, to be linear. More recently, Wagner et al. (1995) developed a new model that includes the contribution of the matrix to the energy balance scheme and has a more realistic stress profile in the stress build-up region around the fiber breaks. The authors demonstrated that the degree of fiber-matrix bonding can be quantified by means of the interface energy for the initiation of debonding, rather than by using a stress-based interfacial parameter. The interface energy for the initiation of debonding is shown to be function of the fiber and matrix geometrical and material characteristics, and of the initial debonding length. The values of these interface fracture energies, although somewhat low, are justified not only by experimental evidence (see e.g. Varna et al. (1997)), but also from previous micro-mechanical numerical analyses (Melro et al., 2013b), which have demonstrated that the brittle behavior in transverse tension typical of composites is only captured for such low values of interfacial toughness (Arteiro et al., 2014).

Thanks to the recent advances in the computational techniques, it is possible, with the right modeling strategy, to simulate these fracture mechanisms without having to fabricate and test the material under different loading conditions to study the desired mechanisms.

1.2 Rational

With the aim of understanding the different interlaminar damage mechanisms, a representative micro-mechanical computational model, that is able to account for the properties and distribution of the constituents of the composite, is created. A plasticity model with damage was used for the epoxy resin, which allows to tackle the non-linear behavior of the composite associated to the matrix material.

1.3 Problem Statement

Due to the sophistication of the modeling techniques and to the ever increasing technological power, computational micro-mechanics has been emerging as an accurate and reliable tool to study the mechanical response of laminated composites. Testing procedures, failure criteria, and finite element analysis techniques are at the engineers disposal to evaluate and predict interlaminar fracture of composite materials. The models developed in this thesis are intended to, with the proper inputs, simulate conditions that are very difficult to achieve by means of controlled practical tests. With the appropriate model it is possible to describe the overall behavior of the composite and the inhomogeneities that are present in the micro-structure, in order to evaluate interlaminar fracture mechanisms.

1.4 Objectives

Given the current state of art in micro-mechanical analyses of long-fiber reinforced composite materials, this thesis aims to develop models that are capable of adequately represent each constituent, i.e. the fibers, matrix and interfaces of the composite, as well as creating a modeling strategy for a representative volume element that represents the plies of the composite with different stacking orientations.

The analysis of the mechanical behavior of the epoxy resin matrix under different loading conditions that induce interlaminar damage is one of the objectives of this thesis. After understanding the different damage mechanisms and material models used to represent the mechanical behavior of the matrix and with the characterization of the modes of fracture in composite materials, this thesis has the objective, with the aid of the finite element method, of understanding in which circumstances for unidirectional (UD) fiber-reinforced composites the different interlaminar fracture mechanisms, such as, debonding between matrix and fibers, matrix cracking or migration between the different processes can happen. In addition, multidirectional (MD) composites can also be considered to analyze the propagation of a crack through the matrix and the delamination migration of interlaminar cracks between plies of different orientation.

1.5 Thesis layout

This thesis is organized by chapters. It includes a bibliography, as well as a set of appendices.

Chapter 2 presents the state of art in fracture mechanics. Different topics are addressed, including a brief recall on the Linear Elastics Fracture Mechanics (LEFM), typical failure mechanisms in composite materials, delamination, ways to identify it and existing toughening mechanisms. The concept of the representative volume element is introduced, as well as a brief description of homogenization and hybrid models. The damage between cohesive surfaces is addressed, as well as the plastic response of epoxy polymers, to understand which material models are available in the literature.

Chapter 3 is dedicated to the generation and development of the mechanical models. First, it is explained in detail the algorithm that generates the RVE with random distribution of fibers and geometrical periodic side boundaries. Then, another explanation is presented to treat the case of the 3D RVE. This RVE can be composed of a single-ply laminate or a double-ply laminate with any give orientation, with $\theta \in [-180; 180]$. Finally, the hybrid models are are described, as well as the geometrical models studied in this thesis.

Chapter 4 presents and describes the damage and material models that are used to model the matrix and the fiber/matrix interface. The fibrous reinforcements are addressed as well, but, since the case under study involves matrix-dominated interlaminar damage, they are considered linear-elastic.

Chapter 5 presents the numerical simulations that were done for the delamination fracture mechanism. Simulations were made for the case of the single mode (I and II) and mixed-mode delamination. Due to the lack of time, it was only analyzed, for these three cases, the ply orientation of $(0°/0°)$ and $(0°/90°)$. The purpose was to observe the propagation of the damage along the epoxy resin by observing the initiation and evolution of damage.

Finally, in Chapter 6, the main conclusions regarding the work carried out during this thesis are presented and some follow-up work for more detailed study of interlaminar fracture mechanisms of composites is proposed.

Chapter 2

Fracture in Composites - State of Art

Linear Elastic Fracture Mechanics (LEFM) applies to the growth of cracks in homogeneous materials. Hence, applying LEFM to the propagation of interlaminar cracks in a composite materials implies that these are treated as homogeneous materials. With such assumption, the LEFM can be used to describe and characterize (with the proper value of fracture toughness) the interlaminar fracture of the composite material by using different experimental tests, such as the DCB (Double Cantilever Beam), ENF (End Notched Flexure) and MMB (Mixed Mode Bending) tests.

Naturally, at the microscopical level, the fracture process is much more complex, but the possibility of "capturing" what happens at the level of the constituents (micro-scale) is important for further understanding the different mechanisms that govern interlaminar damage in general composite laminates. A RVE (Representative Volume Element) is used to describe the inhomogeneities of the material at the micro-scale, and the concept of homogenization is introduced in order to obtain the effective material properties of the material at a higher scale (meso or macro scale).

With this chapter, the reader is able to understand several concepts about the micro-mechanics of fracture in composite laminates, as well as the several damage mechanisms that govern failure of composites, with a special focus in delamination.

2.1 Failure mechanisms in composite materials

Fracture of fiber-reinforced composites is sometimes controlled by numerous microcracks that are distributed throughout the material rather than a single macroscopic crack. One advantage of composite materials is that fracture seldom occurs catastrophically without warning, but tends to be progressive, with subcritical damage widely dispersed through the material (Anderson, 2012). Tensile loading can produce matrix cracking, fiber rupture, pullout and fiber/matrix debonding (Figure 2.1). Compressive loading can produce microbuckling of fibers (Figure 2.2) and/or transverse cracking in the matrix. For instance, if the material contains a preexisting delaminated region, it is probable that compressive loading leads to macroscopic delamination buckling.

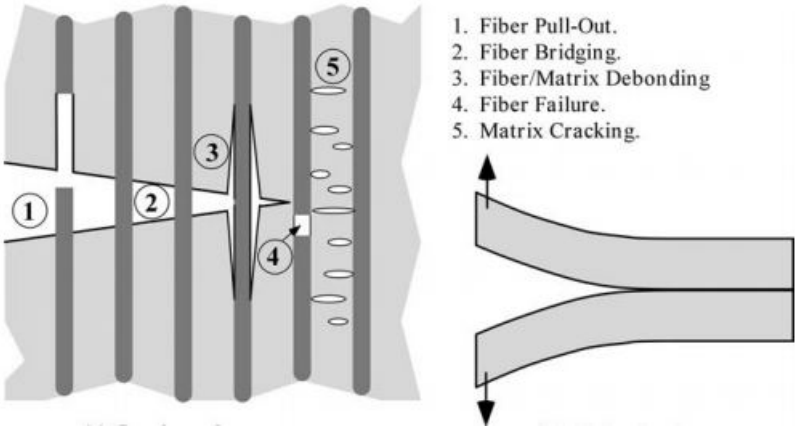

Figure 2.1: In-plane damage and delamination fracture mechanisms (Anderson, 2012).

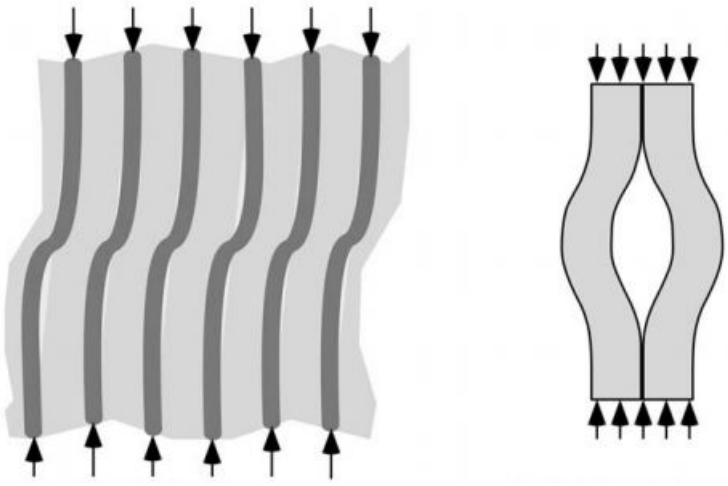

Figure 2.2: Microbuckling and buckling delamination fracture mechanisms (Anderson, 2012).

2.2 Delamination

Delamination is one of the predominant forms of failure in laminated composites due to the lack of reinforcement in the thickness direction (Camanho and Davila, 2002). Delamination as a result of impact, manufacturing defects (voids, pores, or other small defects that are present between layers) or from geometry discontinuities can induce early laminate failure and cause a significant reduction in the compressive load carrying capacity of a structure, making it an important failure mechanism in composites (Anderson, 2012). Besides mechanical loads, the moisture and temperature may also cause interlaminar stresses in a laminate. These may be caused by (1) residual thermal stresses due to cool down of the laminate from the elevated curing temperature or due to the difference between test and stress free temperatures, (2) residual stresses created by the moisture absorption in the laminate and (3) moisture gradient through the thickness of the laminate (Garg, 1988). This type of damage reduces the natural frequency, as a direct result of the reduction of stiffness, which may cause resonance if the reduced frequency is close to the working frequency. It is therefore also important to understand the performance of delaminated composites in a dynamic environment. A comprehensive review of analytical models and numerical analyses of the vibration behavior of delaminated composite structures has been provided by Della and Shu (2007).

2.2.1 Modes of fracture

Delamination can occur in different modes of fracture. There are three distinct modes of fracture that are related directly to the type of loading. These modes are denoted as mode I (normal tension), mode II (in-plane shear) and mode III (out-of-plane shear). Figures 2.3 - 2.5 show all three modes, as well as the type of loading required to induce them.

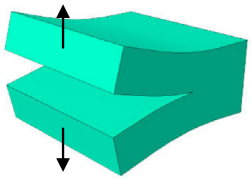

Figure 2.3: Mode I.

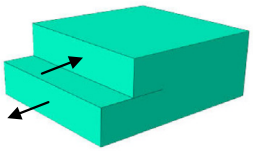

Figure 2.4: Mode II.

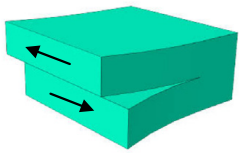

Figure 2.5: Mode III.

The mode I type fracture, is the most common fracture mode and used in the fracture toughness testing. In this mode type fracture, a normal stress field induces an opening effect. The mode I fracture toughness is evaluated by imposing a simple uniaxial stress state to the specimens. The DCB (Double Cantilever Beam) (Figure 2.9) test is used to obtain this material property.

Mode II fracture is caused by in-plane shear or a sliding motion between two surfaces. This failure mode is particularly relevant in laminated composites due to its layered construction. To evaluate the mode II fracture toughness, a three point bending apparatus is typically used to conduct ENF tests (Figure 2.11).

Mode III fracture testing has been the greatest challenge in characterization of the three basic modes. Normally, ensuring a pure mode III fracture is extremely difficult. Two commonly used test methods for characterizing mode III are the split cantilever beam (SCB) test and the edge crack torsion (ECT) test. The SCB test for mode III delamination characterization was first proposed by Donaldson (1988), which used the same type of specimen as the DCB test in mode I and the ENF test in mode II. However, further studies on the SCB test showed that it did not yield a 'pure' mode III delamination, and a substantial mode II component at the edges of the specimen existed. To eliminate the mode II component, Sharif et al. (1995) and Robinson and Song (1994) proposed a new loading scheme in the SCB test that consisted of two sets of loads on each arm, with one being twice the magnitude of the other at one-half of the distance from the crack tip. This eliminated the moment at the crack tip, eliminating the mode II component. The true value of the mode III fracture toughness, could therefore be determinated.

Delaminations in service seldom occur in pure mode I, II or III, but rather in a mixture of the three modes. However, most studies of mixed mode delamination have been limited to a mixture of modes I and II. Of the many tests, the MMB, proposed by Reeder and Crews (1990), appears to be the most promising one. These authors analyzed the MMB specimen (Figure 2.12) using a simple superposition of the stress analysis of the DCB and the ENF specimens. A wide range of ratios of mixed mode I and II can be achieved simply by moving the loading point on the lever.

2.2.2 Instability of crack growth and the R-curve

One important parameter to analyze is the stability of the crack growth. The crack growth can be stable or unstable depending on how the energy release rate ($\mathcal{G}$) varies with crack size. Crack extension occurs when $\mathcal{G} = R$, where R is the material resistance to crack extension. The relation between R and the crack length (a) is called *crack resistance curve* or R-curve. The corresponding relation between $\mathcal{G}$ and a is the *driving force curve*. Figures 2.6 and 2.7 show schematic driving curves for a fixed initial crack length (a_0), and the R-curves for two types of material behavior. Figure 2.6 shows a flat R-curve. In this case the crack propagation is unstable. Figure 2.7 shows a material with a rising R-curve. The crack grows a small amount before unstable growth.

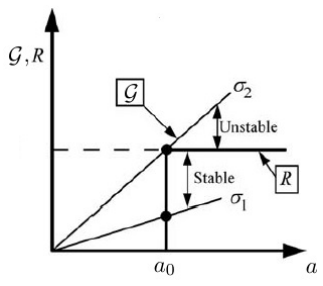

Figure 2.6: Flat R curve (Anderson, 2012).

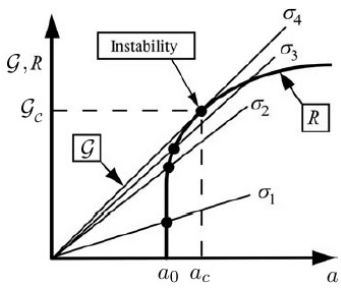

Figure 2.7: Rising R curve (Anderson, 2012).

So, unstable crack growth occurs when

$$\frac{\partial \mathcal{G}}{\partial a} > \frac{\partial R}{\partial a} \tag{2.1}$$

When a material is characterized by a rising R-curve, it cannot be uniquely characterized with a single fracture toughness value. According to Equation (2.1) unstable crack growth occurs when the driving force curve is tangent to the R curve, but this point of tangency is not universal, it depends on the shape of the driving force curve, which depends on the configuration of the structure.

2.2.3 Interlaminar fracture toughness

The interlaminar fracture toughness of a composite is very often treated as same of the matrix. The matrix and composite toughness are seldom equal, however, the contribution of the fibers to the fracture toughness it is not completely negligible. For example, Drzal et al. (1992) observed that in IM6/epoxy composites, the mode two fracture toughness ($\mathcal{G}_{II_C}$) increases with increasing levels of fiber surface treatment. Depending on the type of resin, if it is brittle or tough, the overall material (composite) presents different values of the fracture toughness (Figure 2.8), but, if a composite has a high ductility matrix, only a small fraction of its toughness is transferred to the composite. The failure of tough matrix is sometimes related with the matrix/fibers bond. The bonding between the constituents has a weaker toughness comparing with the matrix, contributing for a lower interlaminar fracture toughness.

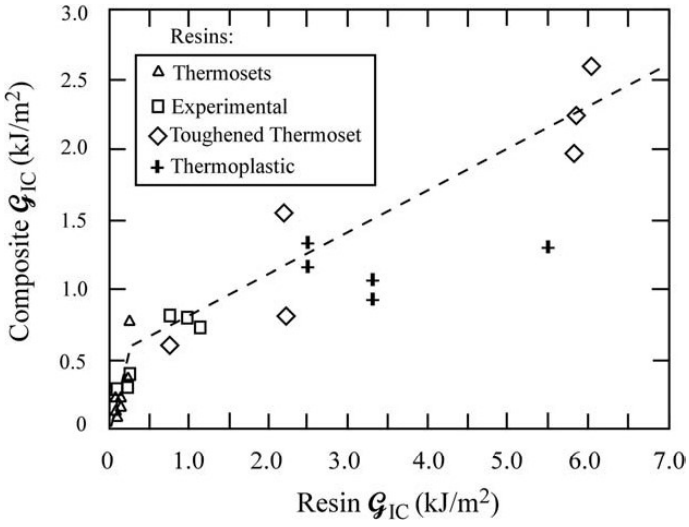

Figure 2.8: Mode I fracture toughness of the matrix material vs the one of the composite (Anderson (2012)).

The mode II fracture toughness it is typically 2 to 10 times higher than the mode I fracture toughness. Mode II delamination strongly affects the structural behavior under out-of-plane loading, especially from low-velocity impact. From the standpoint of the failure mechanisms involved, the deformation and fracture behavior of the resin between fibers at the microscopic level must critically control the macroscopic composite behavior related to this failure mode (Lee, 1997).

2.2.4 Identification/evaluation methods

As delamination is one of the primary failure types in laminated composite structures, occurring under severe conditions of performance (oscillating load, strain, stress, impact of foreign objects), an early detection and continuous monitoring of this fracture mechanism can avoid significant financial losses and emergency situations. However, delamination may not be visible or barely visible on the surface, since the plies are embedded within the composite structures. Therefore, there are various ways to detect and locate this type of fracture mechanism.

Damage identification techniques based on ultrasonic waves represent the most frequently adopted structural health monitoring (SHM) approach. Such popularity is due to well-known virtues of ultrasonic methods such as rapid inspection of large parts with a few piezoelectric transducers and high sensitivity to damage. However, the desirable features of ultrasonic wave-based damage detection techniques are severely undermined when multilayered composite structures are considered. The inhomogeneity/anisotropy of these structures together with complex geometrical shapes are reflected into a high complexity of the acquired signals when ultrasonic wave-based techniques are adopted, thus requiring time-demanding signal processing and interpretation techniques (Pasquali and Lacarbonara, 2015). In the context of ultrasonic waves-based methodologies, Rayleigh-Lamb waves, forced to propagate along a path defined by the material boundaries of the structure, are the most widely used diagnostic waves in SHM problems (e.g. Staszewski et al. (2004)).

Another non-destructive evaluation (NDE) methods using damage-sensitive features are based on mechanical vibrations. These methods exploit the fact that the vibrational characteristics of a structure are determined by its geometry, boundary conditions, and viscoelastic (storage and loss) properties. In composites, internal damage can have consequences to all of these. Dramatic downward shifts in some of the narutal vibrational frequencies and/or significant increases in damping have been found to occur as a result of the introduction of delaminations or other damage in the composite (Penn et al., 1999).

Transfer function or impedance in frequency domain using a distributed array of piezoelectric actuators and sensors have been, as well, successfully used to detect and locate internal delamination (Shang et al., 2010). The introduction of these smart materials for adaptive structures may significantly improve the reliability and safety of structural systems. Many studies in this field, until now, have focused on the experimental investigation of the change in the data of piezoelectric sensors due to damage and on the illustration of the possible detection of the presence of damages. For instance, the vibration data (natural frequency data) from sensors have been used. More information about this topic is provided by Hu (2006), Joseph et al. (1996) or Hu et al. (2008).

2.2.5 Matrix toughening methods

Since delamination is common in some types of loading conditions, it is important to overcome or avoid it. One effective way to do this is to increase the matrix toughness by incorporating secondary phase particles into the polymer matrices. Toughened

epoxy matrices can normally result in high interlaminar fracture toughness and delamination growth resistance (Ye et al., 2010). Key toughening mechanisms have been identified as:

- Crack front bowing or crack pinning (Fu et al., 2008);
- Crack path deflection (Zamanian et al., 2013);
- Particle/matrix de-bonding and subsequent void growth;
- Localized shear yielding (Huang and Kinloch, 1992);
- Bridging of the crack surfaces by the particles (Launey and Ritchie, 2009);

It is important to note that the relevance of this mechanisms varies between the different combinations of the matrix of the composite and their reinforcements. It has been shown that the size and stiffness of the particles significantly affects the ability of the crack to be pinned or to deflect (Zuev, 2012). Various studies have been made related to the improvement of the matrix bulk toughness by systematically varying the reinforcement volume fractions, stiffness and size, and it has been shown that the bulk toughness is possible to control with these parameters. In addition, the incorporation of these particles between the plies of a composite, called interlayering, has been shown by several authors to increase the interlaminar fracture toughness (Singh and Partridge (1995), Hojo et al. (2006) and Yasaee et al. (2012)). However, the increase of interlayer toughness can be ineffective if the cracks propagate by avoiding the toughened interlayer (Sela and Ishai, 1989).

2.3 Evaluation of the interlaminar fracture toughness

In order to use the prediction methods for delamination growth and to compare the performance of different materials, it is necessary that a correct assessment of delamination fracture toughness is made by using test methods. In this section it is described three different experimental fracture tests that are used to evaluate the interlaminar fracture toughness of a composite material. They are:

- DCB - Double Cantilever Beam;
- ENF - End Notched Flexure;
- MMB - Mixed Mode Bending.

2.3.1 DCB - Double Cantilever Beam

The double cantilever beam (DCB) specimen is probably the most common configuration to measure the interlaminar fracture toughness. It is often used to determine the mode I critical energy release rate ($\mathcal{G}_{I_C}$). It consists in applying symmetrical opening tensile forces at the ends of a pre-delaminated DCB (Figure 2.9). These forces are going to induce a growth on the initial debond length allowing the establishment of a direct relationship between a given force, a vertical displacement and a debond length (a). Figure 2.10 represents the boundary conditions applied to the model.

The boundary conditions applied are:

- lower edge displacements in the x and z directions are prevented, i.e., $u = w = 0$;
- a z-wise displacement w was applied to the upper edge, for which $u = 0$;
- to prevent rigid body motion, $v = 0$ was imposed to the lower edge.

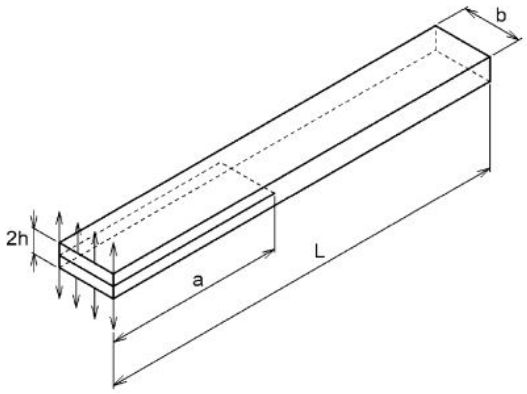

Figure 2.9: The DCB specimen (De Morais (2003)).

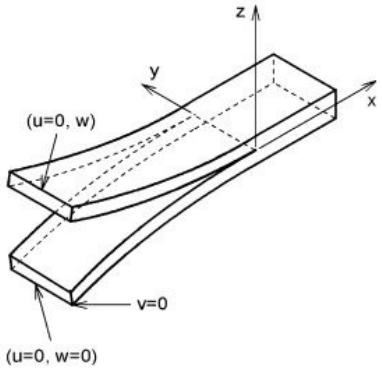

Figure 2.10: Scheme illustrating the DCB boundary conditions (De Morais (2003)).

The energy release rate for an orthotropic DCB specimen, with the fiber direction coincident with the axial direction is defined as:

$$\mathcal{G}_I = \frac{12P^2}{b^2h^3E_1}\left[a^2 + \frac{h^2E_1}{10G_{13}}\right] \tag{2.2}$$

For the case of an isotropic specimen, i.e., $E_1 = E$ and $G = E/(2(1+\nu))$, the strain release rate is defined by:

$$\mathcal{G}_I = \frac{12a^2P^2}{b^2h^3E} \tag{2.3}$$

2.3.2 ENF - End Notched Flexure

The ENF fracture test it is a simple test that consists on a pre-cracked specimen under three point bending loading. One of its disadvantages consists of an unstable crack propagation. In fact, to obtain a stable crack propagation, the length of the pre-cracked region (initial crack length) has to be be higher that 70% of the total length of the specimen ($a_0/L > 0.7$) (Carlsson et al. (1986)). The delaminated section is placed at the end of the specimen to accomodate the sliding deformation resulting from the flexure of the delaminated region. Like the DCB test, the derivation of the energy release rate for this test is based on the change in compliance with crack extension. The position of the load and the displacement to be analyzed are represented in Figure 2.11.

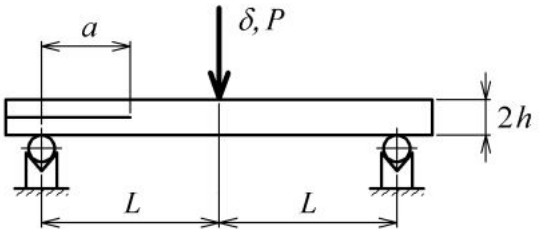

Figure 2.11: Dimensions and load definitions in the ENF test (de Moura et al. (2006)).

The flexural modulus of an ENF specimen can be calculated as a function of the initial compliance, ($C_0 = \frac{\delta_0}{P}$), and the initial crack length a_0 as:

$$E_f = \frac{3a_0^3 + 2L^3}{8bh^3}\left(C_0 - \frac{3L}{10G_{13}bh}\right)^{-1} \tag{2.4}$$

Some phenomena that affect the specimen behavior and consequently affect the $P - \delta$ curve, such as the influence of the stress concentration near the crack tip and the variability of the material between different specimens, are taking into account in the flexural modulus. Some phenomena (e.g. micro cracking or inelastic processes) happen in the FPZ (Fracture Process Zone), the region ahead of crack tip, during propagation that need as well to be taken into account (Hu and Duan (2008)).

So, the compliance during crack propagation can be defined as:

$$C = \frac{3(a + a_{FPZ})^3 + 2L^3}{8E_f bh^3} + \frac{3L}{10G_{13}bh} \tag{2.5}$$

and consequently, an equivalent crack length can be defined as:

$$a_{eq} = a + a_{FPZ} = \left[\frac{C_{corr}}{C_{0\,corr}}a_0^3 + \frac{2L^3}{3}\left(\frac{C_{corr}}{C_{0\,corr}} - 1\right)\right]^{\frac{1}{3}} \tag{2.6}$$

where $C_{0\,corr}$ and C_{corr} are given by:

$$C_{corr} = C - \frac{3L}{10G_{13} + bh} \quad ; \quad C_{0\,corr} = C_0 - \frac{3L}{10G_{13} + bh} \tag{2.7}$$

The critical energy release rate for mode II loading can then be defined as:

$$\mathcal{G}_{II_C} = \frac{9P_c^2 a_{eq}^2}{16b^2 E_f h^3} \tag{2.8}$$

Neglecting the effect of the flexural modulus, E_f, and what happens in the FPZ zone, the expression of the strain energy release rate of an orthotropic specimen, with the fiber direction parallel to the axial direction, can be simplified as:

$$\mathcal{G}_{II} = \frac{9P^2}{16b^2h^3E_1}\left[a^2 + \frac{0.2h^2E_1}{G_{13}}\right] \tag{2.9}$$

For the case of an isotropic specimen:

$$\mathcal{G}_{II} = \frac{9P^2a^2}{16b^2Eh^3} \tag{2.10}$$

2.3.3 MMB - Mixed Mode Bending

This experimental test accounts for delamination with combined tensile normal stress (mode I) and sliding shear stress (mode II). The mixed-mode behavior is achieved by adding an additional load the ENF test specimen that separates the arms of the split unidirectional laminate as in a DCB test. By applying these two loads through a lever and hinge apparatus as shown in Figure 2.12 the test can be done by applying a single load (P). The load distance c determines the relative magnitude of the two resulting loads on the specimen and the mixed-mode ratio at the delamination front. Pure mode I loading occurs when the beam is removed and the hinge is pulled up. Pure mode II loading occurs when the load P is applied directly above the beam midspan ($c = 0$).

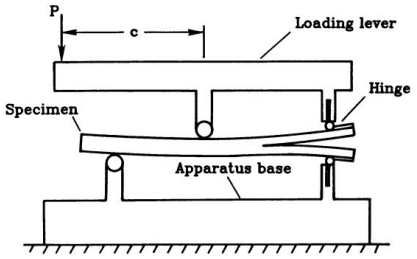

Figure 2.12: MMB experimental test (Reeder and Crews, 1990).

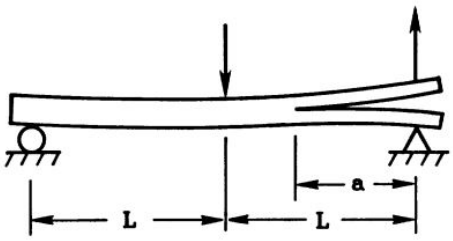

Figure 2.13: Scheme illustrating the MMB boundary conditions (Reeder and Crews, 1990).

The MMB loading can be represented by a superposition of a simple mode I and mode II loadings, used with DCB and ENF tests, respectively. Knowing that the mode I component of the loading P (Reeder and Crews (1990)) is:

$$P_I = \left(\frac{3c - L}{4L}\right)P \tag{2.11}$$

and substituting P in Equation (2.2) by P_I, it leads to the following equation for $\mathcal{G}_I$ of the MMB test:

$$\mathcal{G}_I^m = \frac{3P^2(3c - L)^2}{4b^2h^3L^2E_1}\left[a^2 + \frac{h^2E_1}{10G_{13}}\right] \tag{2.12}$$

Analogously, for the case of mode II, using the energy release rate defined by Equation (2.8), knowing that the mode II component of the loading P (Reeder and Crews (1990)) is:

$$P_{II} = \left(\frac{c + L}{L}\right)P \tag{2.13}$$

and substituting P in Equation (2.8), it leads to the following equation for $\mathcal{G}_{II}$ of the MMB test:

$$\mathcal{G}_{II}^{m} = \frac{9P^2(c+L)^2}{16b^2h^3L^2E_1}\left[a^2 + \frac{0.2h^2E_1}{G_{13}}\right] \tag{2.14}$$

The total energy release rate for the MMB test is obtained adding Equations (2.12) and (2.14):

$$\mathcal{G}_{T}^{m} = \frac{P^2}{16b^2h^3L^2E_1}\left(117c^2a^2 + \frac{12.6c^2h^2E_1}{G_{13}} - 54cLa^2 - \frac{3.6cLh^2E_1}{G_{13}} + 21L^2a^2 + \frac{3L^2h^2E_1}{G_{13}}\right) \tag{2.15}$$

For the isotropic specimens it is obtained adding Equations (2.3) and (2.10):

$$\mathcal{G}_{T}^{m} = \frac{3a^2P^2}{16b^2h^3L^2E}[4(3c-L)^2 + 3(c+L)^2] \tag{2.16}$$

2.4 Micro-mechanical and Hybrid Modeling

2.4.1 Modeling approach

Fiber reinforced composites (FRC) can be analyzed at different scales:

- Micro-scale - At this scale, the material is described as a heterogeneous medium, meaning that the two constituents (fibers and matrix) are seen as individual homogeneous materials. The mechanical behavior of the two constituents is the main focus of the analyses performed at this scale taking into account the interactions between them. Debonding of the interface between the constituents and/or yielding or cracking of the matrix can be modeled at this scale.
- Meso-scale - This scale is related to the lamina of the composite. Each ply is considered as an homogeneous material (transversal isotropic for an UD composite). At this scale, the interaction between constituents is not accounted explicitly. Normally delamination is predicted at this length-scale.
- Macro-scale - The whole composite material is treated as a homogeneous one and the effects of the constituents materials are represented only by averaged apparent properties of the laminate.

In hybrid models, micro- and meso-scale modeling strategies are employed in the same model to reduce the computational cost while ensuring a correct material and geometrical representation of the problem under study. As shown in Figure 2.14, homogenized regions are combined with a detailed micro-scale description of the composite material ahead of the crack tip.

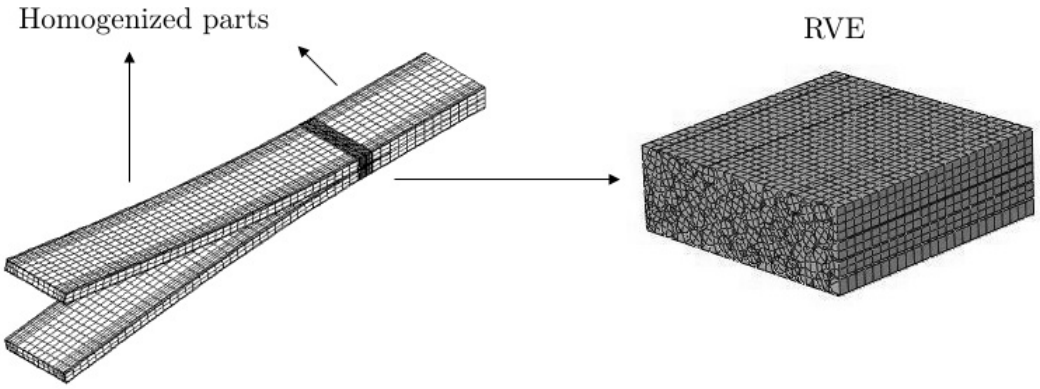

Figure 2.14: Representation of the hybrid model and detail of the region discretized at the micro-scale.

2.4.2 RVE - Representative Volume Element

The concept of RVE (Representative Volume Element) was first introduced by Hill (1963) and represents a sample that is structurally entirely typical of the whole mixture on average. It represents a mathematical point of a continuum field that has the objective of characterizing the microstructure of the material. The size of the RVE is an important parameter and cannot be neglected. According to Hill (1963) the RVE only properly characterizes the microstructure if it is statistically representative of the mixture of constituents and if it has a dimension that contains a sufficient number of inclusions that represent, in average, the material microstructure:

$$L_{inh} << L_{RVE} << L_{macro} \tag{2.17}$$

Equation (2.17), designated by *Scale Separation Principle* proposed by Hashin (1983), states that the characteristic size of the RVE (L_{RVE}) has to be much larger than the size of the inhomogeneities (L_{inh}), e.g. the diameter of circular inclusions, and has to be much smaller than the size of the macroscopic domain (L_{macro}). In addition, an RVE must be sufficiently large to allow a meaningful sampling of the microfields and sufficiently small for the influence of macroscopic gradients to be negligeble and for an analysis of the microfields to be possible.

The spatial arrangement of the fibers in the matrix is usually not periodic and it is highly dependent of the manufacturing process. There are a several fiber distribution patterns available inside a RVE, some that are periodic (quadrangular and hexagonal periodic), some that are periodic inside unit cells (point and Y-distribution (Matsuda et al. (2003))) and some are completely random. In terms of the macro-scale response of laminates, Matsuda et al. (2003) showed that the spatial distribution of fibers inside the RVE does not affect it, but also concluded that it affects the microscopic distribution of stress. Thus when studying the evolution of damage in the matrix it is important that the RVE considers the transverse randomness of the fiber distribution. Figure 2.15 and 2.16 represent examples of a 2D and a 3D RVE, respectively.

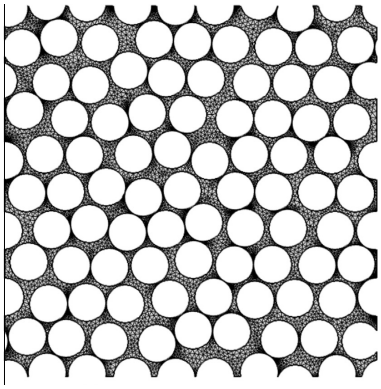

Figure 2.15: 2D RVE (Catalanotti (2016)).

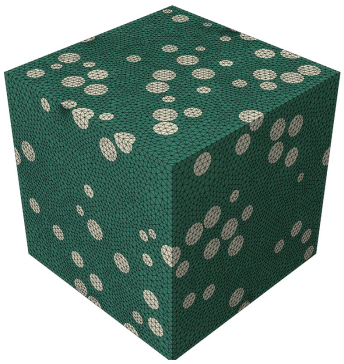

Figure 2.16: 3D RVE (Catalanotti (2016)).

2.4.3 Homogenization

Homogenization is a basic concept of the multi-scale models. It allows the transition between entities defined at micro-scale to the meso or macro scale (Nemat-Nasser et al. (1996)) deducing the effective material properties (e.g., stiffness, thermal expansion and strength properties, electrical, magnetic and electromagnetic properties) of multiphase materials from the corresponding material behavior of the constituents (and of the interfaces between them) and from the geometrical arrangement of the phases. Homogenization procedures can be interpreted as finding a homogeneous comparison material that is energetically equivalent to a given inhomogeneous material. In micro-mechanical approaches, the stress and strain fields in an inhomogeneous material are split into contributions corresponding to different length scales. For each pair of length scales there is:

- Microfields - fluctuating stress and strain fields at the smaller length scale ("fast variables");
- Macrofields - gradients of the stress and strain fields at the larger length scales ("slow variables").

Formally, this splitting of the strain and stress fields into slow and fast contributions can be written as:

$$\boldsymbol{\varepsilon}(x) = \langle \boldsymbol{\varepsilon} \rangle + \boldsymbol{\varepsilon}'(x) \quad \text{and} \quad \boldsymbol{\sigma}(x) = \langle \boldsymbol{\sigma} \rangle + \boldsymbol{\sigma}'(x) \tag{2.18}$$

where $\langle \boldsymbol{\varepsilon} \rangle$ and $\langle \boldsymbol{\sigma} \rangle$ are the macroscopic fields, whereas $\boldsymbol{\varepsilon}'$ and $\boldsymbol{\sigma}'$ stand for the microscopic fluctuations. For any region of an inhomogeneous material that has a linear elastic behavior, the microscopic strain and stress fields, $\varepsilon(x)$ and $\sigma(x)$, and the corresponding macroscopic responses, $\langle \boldsymbol{\varepsilon} \rangle$ and $\langle \boldsymbol{\sigma} \rangle$, can be formally linked by localization relations of the type:

$$\boldsymbol{\varepsilon}(x) = \boldsymbol{A}(x) \langle \boldsymbol{\varepsilon} \rangle \quad \text{and} \quad \boldsymbol{\sigma} = \boldsymbol{B}(x) \langle \boldsymbol{\sigma} \rangle \tag{2.19}$$

$\boldsymbol{A}(x)$ and $\boldsymbol{B}(x)$ are called mechanical strain and stress concentration tensors (Hill, 1963), respectively.

For a volume element Ω_s of an inhomogeneous material that is sufficiently large, contains no significant gradients of composition and shows no significant variation in the applied loads, homogenization relations take the form of volume averages of some variable $f(x)$.

$$\langle f \rangle = \frac{1}{\Omega_s} \int_{\Omega_s} f(x) \, \mathrm{d}\Omega \tag{2.20}$$

The homogenization relations for the stress and strain tensors can be given as,

$$\langle \boldsymbol{\varepsilon} \rangle = \frac{1}{\Omega_s} \int_{\Omega_s} \boldsymbol{\varepsilon}(x) \, \mathrm{d}\Omega = \frac{1}{2\Omega_s} \int_{\Gamma_s} (\mathbf{u}(x) \otimes \mathbf{n}_\Gamma(x) + \mathbf{n}_\Gamma(x) \otimes \mathbf{u}(x)) \, \mathrm{d}\Gamma \tag{2.21a}$$

$$\langle \boldsymbol{\sigma} \rangle = \frac{1}{\Omega_s} \int_{\Omega_s} \boldsymbol{\sigma}(x) \, \mathrm{d}\Omega = \frac{1}{\Omega_s} \int_{\Gamma_s} \mathbf{t}(x) \otimes \boldsymbol{x} \, \mathrm{d}\Gamma \tag{2.21b}$$

where $\otimes$ represents the vector cross product, Ω_s and Γ_s stand for the volume and the surface of the region under consideration, $\mathbf{u}(x)$ represents the deformation vector, $\mathbf{t}(x) = \boldsymbol{\sigma}(x) \times \mathbf{n}_\Gamma(x)$ are the surface traction vector and $\mathbf{n}_\Gamma(x)$ are surface normal vectors.

Equations (2.18) and (2.21) imply that volume averages of microscopic fluctuations vanish for sufficiently large integration volumes:

$$\langle \boldsymbol{\varepsilon}' \rangle = \frac{1}{\Omega_s} \int_{\Omega_s} \boldsymbol{\varepsilon}'(x) \, \mathrm{d}\Omega = 0 \tag{2.22a}$$

$$\langle \boldsymbol{\sigma}' \rangle = \frac{1}{\Omega_s} \int_{\Omega_s} \boldsymbol{\sigma}'(x) \, \mathrm{d}\Omega = 0 \tag{2.22b}$$

Similarly, surface integrals over the microscopic fluctuations of the field variables tend to zero for appropriate volume elements.

It is important to note that the microgeometries of real inhomogeneous materials are at least to some extent random and teir detailed phase arrangements are highly complex. As a consequence, exact expressions for $\boldsymbol{A}(x)$, $\boldsymbol{B}(x)$, $\boldsymbol{\varepsilon}(x)$ and $\boldsymbol{\sigma}(x)$, etc. in general cannot be provided with reasonable effort and approximations have to be introduced. They are based on ergodic hypothesis, i.e., the heterogeneous material is assumed to be statistically homogeneous. This implies that sufficiently large volume elements selected at random positions within the sample have statistically equivalent phase arrangements and give rise to the same averaged material properties. Basically, they need to be a subvolume of Ω_s that is sufficiently large to be statistically representative of the microgeometry.

Overall behavior

The homogenized strain and stress fields of an elastic inhomogeneous material as obtained by Equation (2.21), can be linked by effective elastic tensor $\boldsymbol{D}^*$ and the effective compliance tensor $\boldsymbol{H}^*$ as:

$$\langle \boldsymbol{\sigma} \rangle = \boldsymbol{D}^* \langle \boldsymbol{\varepsilon} \rangle \quad \text{and} \quad \langle \boldsymbol{\varepsilon} \rangle = \boldsymbol{H}^* \langle \boldsymbol{\sigma} \rangle \tag{2.23}$$

which may be viewed as the elastic tensors of an appropriate equivalent homogeneous material. Using Equation (2.21) these effective elastic tensors can be obtained from the local elastic tensors and from the concentration tensors as volume averages:

$$\boldsymbol{D}^* = \frac{1}{\Omega_s} \int_{\Omega_s} \boldsymbol{D}(x)\boldsymbol{A}(x) \, \mathrm{d}\Omega \quad \text{and} \quad \boldsymbol{H}^* = \frac{1}{\Omega_s} \int_{\Omega_s} \boldsymbol{H}(x)\boldsymbol{B}(x) \, \mathrm{d}\Omega \tag{2.24}$$

Other effective properties of inhomogeneous materials can be obtained by analogous operations.

The resulting homogenized behavior of many multiphase materials can be idealized as being statistically isotropic or quasi-isotropic or statistically transversely

isotropic (e.g. for composites reinforced with aligned fibers). The effective elasticity for statistically transversely isotropic materials have the structure:

$$\boldsymbol{D}^* = \begin{bmatrix} C_{11}^* & C_{12}^* & C_{12}^* & 0 & 0 & 0 \\ C_{12}^* & C_{22}^* & C_{23}^* & 0 & 0 & 0 \\ C_{12}^* & C_{23}^* & C_{22}^* & 0 & 0 & 0 \\ 0 & 0 & 0 & C_{44}^* & 0 & 0 \\ 0 & 0 & 0 & 0 & C_{44}^* & 0 \\ 0 & 0 & 0 & 0 & 0 & C_{66}^* = \frac{1}{2}(C_{22}^* - C_{23}^*) \end{bmatrix} \tag{2.25}$$

where 1 is the axial direction and $2-3$ is the transverse plane of isotropy. This matrix is described by five independent elastic constants. Appropriate elastic parameters in this context are, e.g., the axial and transverse effective Young's moduli, $E_A^* = C_{11}^* - \frac{2C_{12}^{*2}}{C_{22}^* + C_{23}^*}$ and $E_T^* = C_{22}^* - \frac{C_{11}^* C_{23}^{*2} + C_{22}^* C_{12}^{*2} - 2C_{23}^* C_{12}^{*2}}{C_{11}^* C_{22}^* - C_{12}^{*2}}$, the axial and transverse shear moduli, $G_A^* = C_{44}^*$ and $G_T^* = C_{66}^*$, the axial and transverse effective Poisson numbers, $\nu_A^* = \frac{C_{12}^*}{C_{22}^* + C_{23}^*}$ and $\nu_T^* = \frac{C_{11}^* C_{23}^* - C_{12}^* C_{12}^{*2}}{C_{11}^* C_{22}^* - C_{12}^{*2}}$, as well the effective transverse (plane strain) bulk modulus $K_T^* = \frac{C_A^*}{2[(1-\nu_T^*)(C_A^*/C_T^*) - 2\nu_A^{*2}]}$. For the special case of materials reinforced by aligned continuous fibers, however, Hill (1964) derived the relations:

$$E_A^* = v_f E_A^{(\mathrm{f})} + (1 - v_f) E^{(\mathrm{m})} + \frac{4(\nu_A^{(\mathrm{f})} - \nu^{(\mathrm{m})})^2}{(1/K_T^{(\mathrm{f})} - 1/K_T^{(\mathrm{m})})^2} \left(\frac{v_f}{K_T^{(\mathrm{f})}} + \frac{1 - v_f}{K_T^{(\mathrm{m})}} - \frac{1}{K_T^*} \right) \tag{2.26a}$$

$$\nu_A^* = v_f \nu_A^{(\mathrm{f})} + (1 - v_f) \nu^{(\mathrm{m})} + \frac{\nu_A^{(\mathrm{f})} - \nu^{(\mathrm{m})}}{1/K_T^{(\mathrm{f})} - 1/K_T^{(\mathrm{m})}} \left(\frac{v_f}{K_T^{(\mathrm{f})}} + \frac{1 - v_f}{K_T^{(\mathrm{m})}} - \frac{1}{K_T^*} \right) \tag{2.26b}$$

which allow the effective modulus E_A^* and ν_A^* to be expressed by K_T^*, some constituent properties, and the fiber volume fraction v_f. Note that E^* represents the effective Young's modulus. These equations can be used to reduce the number of independent effective elastic parameters required for describing the behavior of unidirectional continuously reinforced composites to three.

The influence of the overall symmetry of the phase arrangement on the overall mechanical behavior of inhomogeneous materials can be marked, especially on the nonlinear responses to mechanical loads. Accordingly, it is good practice to aim at approaching the symmetry of the actual material as closely as possible in any modeling effort.

The evaluation of the local responses of the constituents (in the ideal case, at any material point) for a given macroscopic state of a sample or structure, i.e., localization, is especially important for identifying local deformation mechanisms and for studying as well as evaluating local strength relevant behavior, such as the onset and progress of plastic yielding or of damage, which, of course, can have major repercussions on the macroscopic behavior.

Modeling strategies in continuum micro-mechanics

The analysis of the spatial variations of the microfields in large volume elements tends to be very complicated, so, approximations have to be used. For a completelly detailed information about these methods see Böhm (2004). The author fully described in a detailed way most of the used methods. The modeling approaches that are used to turn around this problem are methods that describe interactions, e.g., between phases or between individual reinforcements, in a collective way in terms of phase-wise uniform fields and methods that are based on studying discrete microgeometries, fully accounting for the interactions between phases. The first methods are:

- Mean-Field Approaches (MFAs): The microfields within each constituent of an inhomogeneous material are approximatted by their phase averages $\langle \boldsymbol{\varepsilon} \rangle^{(p)}$ and $\langle \boldsymbol{\sigma} \rangle^{(p)}$. In these methods the localization relations take the form:

$$\begin{aligned} \langle \boldsymbol{\varepsilon} \rangle^{(p)} &= \bar{\boldsymbol{A}} \langle \boldsymbol{\varepsilon} \rangle, \\ \langle \boldsymbol{\sigma} \rangle^{(p)} &= \bar{\boldsymbol{B}} \langle \boldsymbol{\sigma} \rangle \end{aligned} \tag{2.27}$$

  These phase concentration tensors are not functions of the spatial coordinates. The homogenization relations can be written as

$$\begin{aligned} \langle \boldsymbol{\varepsilon} \rangle^{(p)} &= \frac{1}{\Omega^{(p)}} \int_{\Omega^{(p)}} \boldsymbol{\varepsilon}(x) \, \mathrm{d}\Omega \quad \text{with} \quad \langle \boldsymbol{\varepsilon} \rangle = \sum_p v_f^{(p)} \langle \boldsymbol{\varepsilon} \rangle^{(p)}, \\ \langle \boldsymbol{\sigma} \rangle^{(p)} &= \frac{1}{\Omega^{(p)}} \int_{\Omega^{(p)}} \boldsymbol{\sigma}(x) \, \mathrm{d}\Omega \quad \text{with} \quad \langle \boldsymbol{\sigma} \rangle = \sum_p v_f^{(p)} \langle \boldsymbol{\sigma} \rangle^{(p)} \end{aligned} \tag{2.28}$$

  where (p) denotes a given phase of the material, $\Omega^{(p)}$ is the volume occupied by this phase, and $v_f^{(p)} = \frac{\Omega^{(p)}}{\sum_k \Omega^{(k)}} = \frac{\Omega^{(p)}}{\Omega_s}$ is the volume fraction of the phase.

- Variational Bounding Methods: Variational principles are used to obtain upper and lower bounds on the overall elastic tensors, elastic moduli and other physical properties of inhomogeneous materials the microgeometries of which are described by statistical parameters. In many cases one of the bounds provides good estimates for the physical property under consideration

The second group of approximations are:

- Periodic Microfields Approaches (PMAs): These methods, also referred to as periodic homogenization schemes or unit cell methods, the inhomogeneous material is approximated by an infinitely extended model material with a periodic phase arrangement. The resulting periodic microfields are usually evaluated by analyzing repeating unit cells via analytical or numerical methods. Unit cell approaches are often used for performing materials characterization of inhomogeneous materials in the nonlinear range, but they can also be employed as micro-mechanically based constitutive models. The high resolution of the microfields provided by PMAs can be very useful in studying the initiation of damage at the microscale.

- Windowing Approaches: They represent subregions of the phase arrangement. They are randomly chosen from a given phase arrangement and subjected to boundary conditions that guarantee energy equivalence between the micro- and macroscales. Accordingly, windowing methods describe the behavior of individual inhomogeneous samples rather than of inhomogeneous materials and give rise to apparent rather than effective macroscopic responses.

- Embedded Cell or Embedding Approaches: The inhomogeneous material is approximated by a model consisting of a core containing a discrete phase arrangement that is embedded within some outer region to which far field loads are applied. The material properties of this outer region may be described by some macroscopic constitutive law, they can be determined self-consistently or quasi-self-consistently from the behavior of the core, or the embedding region may take the form of a coarse description and/or discretization of the phase arrangement. This type of method can be used for materials characterization, and they are usually the best choice for studying regions of special interest in inhomogeneous materials, such as the surroundings of tips of macroscopic cracks.

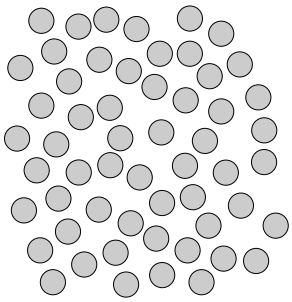

Figure 2.17: Distribution of the constituents.

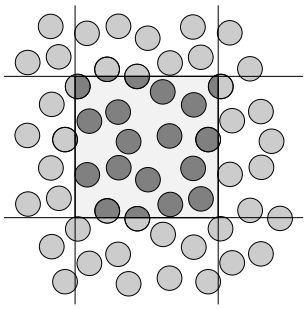

Figure 2.18: Periodic approximation unit cell.

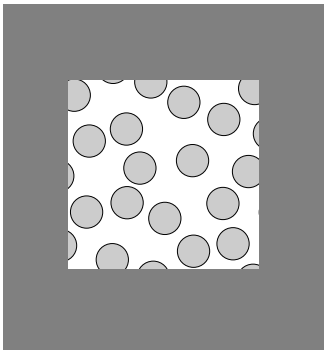

Figure 2.19: Embedded configuration.

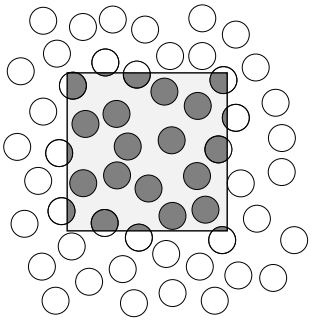

Figure 2.20: Window configuration.

2.4.4 Hybrid meso/micro models

With the given state of art regarding the concept of homogenization, it is possible to introduce the concept of hybrid models. Hybrid multi-scale approach, in which a small-scale model with high resolution is utilized in a fraction of the overall domain and is linked to a large-scale model with coarse resolution over the remainder of the overall domain, can provide necessary efficiency of characterization and computation that will render solution of these problems practical (Scheibe et al., 2007). The models that are at the larger scale represent nothing more than the elastic behavior of the part that is at the micro-scale. These models are sometimes necessary to have in order to focus the study in a desirable part, i.e. the microstructure and use the large scale part to simplify the computational cost of the hole model. The RVE used is assumed to be a representative portion of the composite.

Since this concept about hybrid modeling is somewhat new, there is little information available in the literature. Some authors have exploited this type of models with some success, e.g. Arteiro et al. (2014), Camanho and Lambert (2006), Wisnom et al. (2008) and Arteiro et al. (2015).

2.5 Damage at interfaces

Failure and fracture is a big part of many fields in engineering. It is therefore important to understand and to be able to do calculations on failure processes. This section is dedicated to the description of the damage and cohesive behavior that the interface between the fibers and the matrix can have, as well as the different damage models that can and are used throughout this thesis. The described criterion and models of damage initiation and evolution of cohesive surfaces are defined by the commercial software Abaqus® (ABAQUS (2011)).

Damage mechanics is used in order to model stiffness degradation of the material and material failure refers to the complete loss of load carrying capacity that results from progressive degradation of the material stiffness. To analyze these phenomena efficiently in arbitrary geometries, a general numerical method is needed that can describe the initiation and evolution of a crack. The method should include and be able to simulate the initial loading, the damage initiation with initial debonding, and the damage evolution until complete separation and failure.

The traction-separation model assumes initially elastic behavior followed by the initiation and evolution of damage. The elastic behavior is written in terms of an elastic constitutive matrix that relates the normal and shear stresses to the normal and shear separation across the interface.

The vector **t** represents the nominal traction stress vector and consists of three components:

- τ_1 - Out of plane shear traction;
- τ_2 - In plane shear traction;
- τ_3 - Normal traction;

The corresponding separations are denoted by δ_1, δ_2 and δ_3.

The elastic behavior can then be written as:

$$\mathbf{t} = \left\{ \begin{array}{c} \tau_1 \\ \tau_2 \\ \tau_3 \end{array} \right\} = \begin{bmatrix} K_{11} & K_{12} & K_{13} \\ K_{21} & K_{22} & K_{23} \\ K_{31} & K_{32} & K_{33} \end{bmatrix} \left\{ \begin{array}{c} \delta_1 \\ \delta_2 \\ \delta_3 \end{array} \right\} = \boldsymbol{K\delta} \tag{2.29}$$

This elasticity matrix represents a fully coupled behavior between all components of the traction vector and separation vector since all of the non-diagonal terms are non null values. In order to have an uncoupled traction-separation behavior, the non-diagonal terms of the elasticity matrix have to be zero, i.e., $K_{12} = K_{21} = K_{13} = K_{31} = K_{23} = K_{32} = 0$. This behavior generates pure normal separation or pure shear slip, thus not giving rise to cohesive forces in the shear and normal directions, respectively.

In the next sections ahead, the damage is always specified as a mixed-mode delamination. If one desires to treat it as a single mode fracture, for example mode I, all the terms that involve the contribution of mode II and mode III must be zero or vice-versa.

2.5.1 Damage initiation

The damage initiation defines the point of initiation of degradation of stiffness and it does not actually lead to damage unless damage evolution is also specified. Several damage initiation criteria exist and are explained bellow. Each damage initiation has an output variable associated with it to indicate whether the criterion is met. A value of 1 or higher indicates that the initiation criterion has been met.

So, to fully describe the damage initiation, it is necessary to chose the proper criterion and to chose the peak values of the contact stress when the separation is either purely normal to the interface or purely in the first or the second shear direction. These values are denoted as τ_1^0, τ_2^0 and τ_3^0 and are called interface maximum strengths (Zhandarov and Mader (2005)). Likewise, δ_1^0, δ_2^0 and δ_3^0 represent the peak values of the contact separation.

Maximum stress criterion

Damage is assumed to initiate when the maximum contact stress ratio reaches a value of one:

$$\max\left\{\frac{\langle\tau_3\rangle}{\tau_3^0}, \frac{\tau_2}{\tau_2^0}, \frac{\tau_1}{\tau_1^0}\right\} = 1 \tag{2.30}$$

Quadratic stress criterion

Damage is assumed to initiate when a quadratic interaction function involving the contact stress ratios reaches a value of one (Cui et al., 1992):

$$\left\{\frac{\langle\tau_3\rangle}{\tau_3^0}\right\}^2 + \left\{\frac{\tau_2}{\tau_2^0}\right\}^2 + \left\{\frac{\tau_1}{\tau_1^0}\right\}^2 = 1 \tag{2.31}$$

Maximum separation criterion

Damage is assumed to initiate when the maximum separation ratio reaches a value of one:

$$\max\left\{\frac{\langle\delta_3\rangle}{\delta_3^0}, \frac{\delta_2}{\delta_2^0}, \frac{\delta_1}{\delta_1^0}\right\} = 1 \tag{2.32}$$

Quadratic separation criterion

Damage is assumed to initiate when a quadratic interaction function involving the separation ratios reaches a value of one:

$$\left\{\frac{\langle\delta_3\rangle}{\delta_3^0}\right\}^2 + \left\{\frac{\delta_2}{\delta_2^0}\right\}^2 + \left\{\frac{\delta_1}{\delta_1^0}\right\}^2 = 1 \tag{2.33}$$

The symbol $\langle\cdot\rangle$ used in the equations above represents the Macaulay operator, which is defined as (for every $x \in \Re$):

$$\langle x\rangle = \begin{cases} 0 & \Leftarrow x \leq 0 \\ x & \Leftarrow x > 0 \end{cases}$$

This operator is used to state that the compressive stress or negative separations do not contribute to damage initiation.

2.5.2 Damage evolution

Once any of the damage initiation criteria is satisfied, Equations (2.30) - (2.33), further loading will cause degradation of material stiffness coefficients, basically, damage evolution defines the post damage initiation material behavior. The formulation is based on scalar damage approaches:

$$\tau_i = (1-d)\bar{\tau}_i \ \text{, where } i = 1, 2, 3 \tag{2.34}$$

where $\bar{\tau_1}$, $\bar{\tau_2}$ and $\bar{\tau_3}$ are the contact stresses due to undamaged response predicted by the elastic traction-separation behavior and d is a scalar damage variable that represents the overall damage at the contact point that initially has a value of 0. During the evolution the value of this variable goes from 0 to 1, when fracture occurs. To describe the evolution of damage under a combination of normal and shear separations across the interface, it is useful to introduce an effective separation defined by Camanho and Davila (2002) as:

$$\delta_m = \sqrt{\langle \delta_3 \rangle^2 + \delta_2^2 + \delta_1^2} \tag{2.35}$$

The damage evolution can be specified either in terms of:

- Fracture energy (per unit area);
- Equivalent plastic displacement or effective separation;

The first one involves the energy dissipated due to failure, $\mathcal{G}_C$, and the second the effective separation at complete failure, δ_m^f, relative to the effective separation at the initiation of damage, δ_m^0.

As it has been previously stated, these damage type evolutions are typically described by a traction-separation law. The choosing of which law to use depends on the material in order to represent correctly the fracture behavior of the particular material. In this thesis are only stated the traction-separation laws that are common to both specifications of evolutions, that are the linear and exponential traction-separation behavior.

Evolution based on energy

Damage evolution can be defined based on the energy that is dissipated as a result of the damage process, also called the fracture energy. The fracture energy is equal to the area under the traction-separation curve.

For a linear damage evolution (Figure 2.21) the evolution of the damage variable can be defined as:

$$d = \frac{\delta_m^f(\delta_m^{max} - \delta_m^0)}{\delta_m^{max}(\delta_m^f - \delta_m^0)}, \tag{2.36}$$

$\delta_m^f = \dfrac{2\mathcal{G}_C}{T_{eff}^0}$, where T_{eff}^0 represents the effective traction at damage initiation, δ_m^{max} is the maximum value of the effective separation attained during loading history. $\mathcal{G}_C$ is the mixed mode fracture energy which equals the area below the traction-separation curve. Stiffness matrix is reduced based on damage variable d (Bakis, 2013).

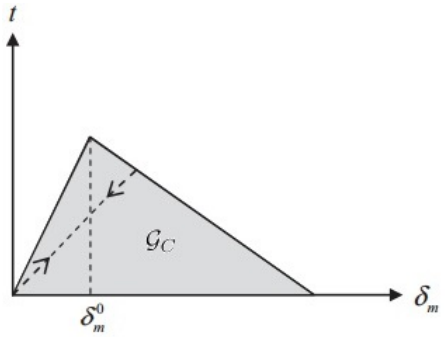

Figure 2.21: Linear traction-separation evolution.

For exponential softening the damage variable, d, reduces to:

$$d = \int_{\delta_m^0}^{\delta_m^f} \frac{T_{eff}}{\mathcal{G}_C - \mathcal{G}_0} \, \mathrm{d}\delta \tag{2.37}$$

In the expression above T_{eff} and δ are the effective traction and separation, respectively. $\mathcal{G}_0$ is the elastic energy release rate at damage initiation. This type of evolution is evidenced in Figure 2.22.

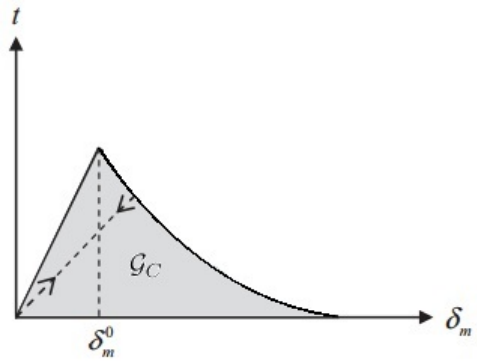

Figure 2.22: Exponential traction-separation evolution.

Evolution based on the effective separation

This evolution represents the damage variable d as a function of the effective separation at complete failure, that is, $\delta_m^f - \delta_m^0$, where has been said before δ_m^f represents the effective separation at complete failure and δ_m^0 the effective separation at damage initiation.

Like the evolution based on energy, the damage variable for a bi-linear traction separation law can be reduced as:

$$d = \frac{\delta_m^f(\delta_m^{max} - \delta_m^0)}{\delta_m^{max}(\delta_m^f - \delta_m^0)}, \tag{2.38}$$

At last, for exponential softening for a evolution based on effective separation, the damage variable, as well in the case of damage evolution under a constant mode mix can be represented as:

$$d = 1 - \left\{ \frac{\delta_m^0}{\delta_m^{max}} \right\} \left\{ 1 - \frac{1 - \exp\left(- \beta \left(\frac{\delta_m^{max} - \delta_m^0}{\delta_m^f - \delta_m^0} \right) \right)}{1 - \exp(-\beta)} \right\} \tag{2.39}$$

In the expression above β is a non-dimensional parameter that defines the rate of damage evolution and $\exp(x)$ is the exponential function.

Fracture criterion

Although there are single and mixed-mode delamination, it is only analyzed the mixed-mode fracture criterion, because the case of single mode fracture is a simplification of the mixed-mode.

The criteria used to predict damage propagation under mixed-mode loading conditions are usually established in terms of the energy release rates and fracture toughness. The most widely used criterion to predict delamination propagation under mixed-mode loading is the *power law* criterion, which is established in terms of an interaction between the energy release rates (Wu and Reuter Jr., 1965):

$$\left(\frac{\mathcal{G}_I}{\mathcal{G}_{I_C}} \right)^{\alpha} + \left(\frac{\mathcal{G}_{II}}{\mathcal{G}_{II_C}} \right)^{\alpha} + \left(\frac{\mathcal{G}_{III}}{\mathcal{G}_{III_C}} \right)^{\alpha} = 1 \tag{2.40}$$

However, the power law criterion is not suited to accurately capture the dependence of the mixed-mode fracture toughness (Camanho and Davila, 2002). In order to account for this variation of fracture toughness as a function of mode ration in epoxy composites, it is used the Benzeggagh-Kenane (BK) criterion (Benzeggagh and Kenane, 1996). This criterion is expressed of the Mode I and II fracture toughness and a mixed-mode interaction parameter η obtained from MMB tests at different mode ratios:

$$\mathcal{G}_{I_C} + (\mathcal{G}_{II_C} - \mathcal{G}_{I_C}) \left(\frac{\mathcal{G}_{II}}{\mathcal{G}_I + \mathcal{G}_{II}} \right)^{\eta} = \mathcal{G}_C \tag{2.41}$$

If Mode III occurs, the criterion is:

$$\mathcal{G}_{I_C} + (\mathcal{G}_{II_C} - \mathcal{G}_{I_C}) \left(\frac{\mathcal{G}_{II} + \mathcal{G}_{III}}{\mathcal{G}_I + \mathcal{G}_{II} + \mathcal{G}_{III}} \right)^{\eta} = \mathcal{G}_C \tag{2.42}$$

In these previous equations, $\mathcal{G}_{I_C}$, $\mathcal{G}_{II_C}$ and $\mathcal{G}_{III_C}$ represent the interface critical energy release rates in Mode I, II and III, respectively. The energy release rates corresponding to total decohesion are obtained from:

$$\mathcal{G}_I = \int_0^{\delta_m^{1f}} \tau_1 \, \mathrm{d}\delta_1 \tag{2.43}$$

$$\mathcal{G}_{II} = \int_0^{\delta_m^{2f}} \tau_2 \, \mathrm{d}\delta_2 \tag{2.44}$$

$$\mathcal{G}_{III} = \int_0^{\delta_m^{3f}} \tau_3 \, \mathrm{d}\delta_3 \tag{2.45}$$

δ_m^{if}, where $i = 1, 2, 3$ represents the effective separation at complete failure only considering the contribution of normal , first shear and second shear traction respectively.

By using four parameters, $\mathcal{G}_{I_C}$, $\mathcal{G}_{II_C}$, $\mathcal{G}_{III_C}$ and η, the BK criterion represents the mixed-mode fracture toughness over a comprehensive range of mode mixity, whereas the two-parameter power law criterion that is usually implemented in decohesion elements can lead to inaccurate results over a large range of mode ratios (Camanho and Davila, 2002).

2.6 Plastic response of epoxy resins

This section is dedicated to the review over the most relevant findings in the literature regarding the plastic response of epoxy resins.

For elastic-plastic materials damage manifests in two forms, that are, softening of the yield stress or degradation of the elasticity (Figure 2.23). It is important for a material model to capture all these behaviors.

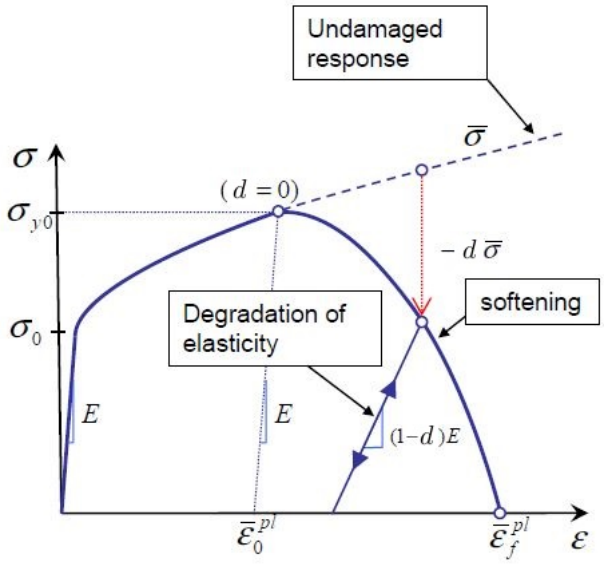

Figure 2.23: Schematic representation of elastic-plastic material with progressive damage.

Asp et al. (1995) developed an experimental set-up which allowed the submission to epoxy matrices of a triaxial stress state when the composite is loaded in the transverse direction. this stress state occurs due to the random distribution of fibers in the transverse cross-section which creates a non-uniform stress state in the surrounding material, i.e. the matrix. In a posterior work, Asp et al. (1996) showed that the material behavior for all epoxy systems tested is non-linear under several loading conditions, and that each system has a different yield behavior. The authors proposed the use of the dilatational energy density criterion to predict failure of polymers under multiaxial tensile loads. However, the criterion is not completely general as it can not predict the material's behavior under more complex stress-states such as the combined effect of shear and normal stresses.

It is difficult to conduct compressive tests on epoxy materials, so Duncan et al. (1998) conducted an experimental investigation to obtain material data for the numerical methods that predict the performance of adhesive bonded joints under impact loading. In this work, it was found that there is a strong influence of the strain rate on the yield behavior of epoxy adhesives.

Duncan et al. (1998) and Charalambides, M. N., Olusanya (1997) introduced the concept of plastic Poisson's ratio. It is defined as the symmetric of the ratio between the plastic transverse strain and the plastic longitudinal strain in an uniaxial tensile test. This quantity varies as hardening progresses. Duncan et al. (1998) also determined that the ratio of the yield compressive stress to the yield tensile stress is independent of the strain rateand that the plastic Poisson's ratio varies between 0.3 and 0.5 , indicating that the volume increases during yielding.

In order to fully characterize the yield and failure behavior of epoxies used in composites, Fiedler et al. (2001) conducted a more vast study on the behavior of epoxy materials subjected to tensile, compressive and shear loadings. The results for the tensile tests show the non-linearity of these specimens under such loading conditions, while the thicker specimens behave in a brittle manner. The torsion test revealed that if the material in cause has a high ductile capacity under a pure shear load, then the specimen did not fail at all. It presented a non-linear behavior with hardening for lower strains, behaving like an elastic-plastic material.

Ghorbel (2008) made a comparative study of different yield criteria with experimental results for polymers. With the results, one can conclude that a good yield criterion for epoxy polymers must account for any dependency of yielding on the hydrostatic component of the applied stress state, it must state that epoxy polymers present a greater yield strength in compression than in tension and that the increasing of strain rates increases yield strength and Young modulus of the polymer.

Mascarenhas et al. (2004) stated that both conic and parabolic criteria are best suited for the yield behavior of polymers. The previous work of Ghorbel (2008) concluded that the paraboloidal variant provided better estimates for yield strengths than the Drucker-Prager.

The paraboloidal yield criterion was first defined by Tschoegl (1971). In the principal stress space, it is represented by a paraboloid whose axis coincides with the hydrostatic axis. A cylindrical surface corresponds to the Von Mises yield criterion and an hexagonal prism represents the Tresca criterion, both applicable to materials whose plastic flow is independent of hydrostatic pressure such as some metals. An hexagonal pyramid is a modified version of the Tresca criterion and represents the Mohr-Coulomb yield criterion. A modified Von Mises gives origin to the Drucker-Prager criterion represented by a conical surface. Figure 2.24 represents the inner surface as the yield surface and the failure surface as outer surface. This surface is particularly attractive because, unlike Tresca, Drucker-Prager or Mohr-Coulomb it does not contain any geometrical features such edges or vertices. This makes the surface differentiable in all of its domain, simplifying the process of implementation into a constitutive model.

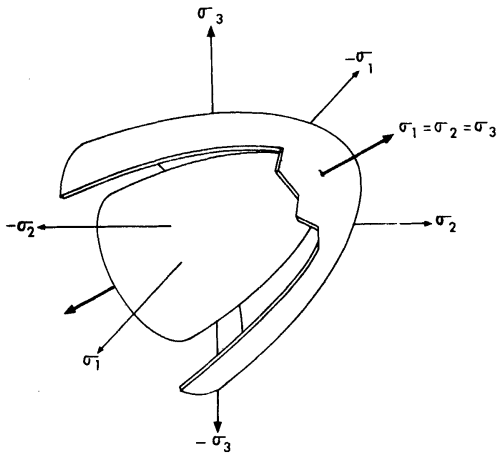

Figure 2.24: Paraboloidal failure surfaces coaxial with the hydrostatic stress (Tschoegl, 1971).

More recent yield criterions were developed based in the paraboloidal yield criterion. Melro et al. (2013a) developed and implemented a constitutive model for epoxy matrices that uses a thermodynamically consistent elasto-plastic pressure dependent that is typically for unidirectional composites. The authors also added isotropic damage to the constitutive model and comparing with available experimental data, it is presented proven to adequately capture the yield behavior of a typical epoxy matrix, including shear non-linear behavior and hydrostatic pressure dependency.

The recent work of Bai et al. (2015) experimental validated at the micro-scale the visco-thermo-mechanical behavior of polymer matrix composites under different loading conditions. The authors developed a new constitutive law for the matrix material taking into account the pressure dependence of the material as well as strain-rate and temperature dependence. The model is proposed using an extension to the paraboloidal model so that the predictive ability of the micro-scale analyses is improved. The authors concluded that is essential to capture the matrix behavior under multi-axial stress states to accuractely predict the composite material behavior. The plasticity model is experimentally validated by considering two different epoxy resin. A complicated longitudinal compression simulation is also considered, and the result indicated that local plastic shear triggers the initiation of the kink band.

Chapter 3

Micro-mechanical Models

Modeling of composite materials is a difficult task due to the complexity of the arrangement of the constituents (fiber and matrix) and the interactions between them. However, with the proper knowledge, it is possible to have models that are able to predict the process, at the micro-scale, of the interlaminar fracture in order to understand in which kind of situations different damage mechanisms appear.

This chapter focuses on the extensive explanation of all the algorithms proposed in this thesis, namely the generation of the 2D and 3D RVEs, as well as the generation of the hybrid models.

3.1 Generation of the RVE

Many methods have been developed for the generation of the RVE models of composites. Gusev et al. (2000) and Wongsto and Li (2005) presented a scheme for the generation of fiber distribution by disturbing an initially regular fiber distribution randomly. Also, Melro et al. (2008) proposed an algorithm to generate periodic random distribution of fibers reaching higher volume fractions ($v_f \approx 0.65$). Recently, Catalanotti (2016) proposed an algorithm that is able to represent the randomness of the material and creates random distributions of uniform spherical or circular particles from a reinforcement volume fraction of 0 to its highest theoretical value, i.e. $v_f \approx 0.74$ for spherical and $v_f \approx 0.91$ for circular particles.

The algorithm proposed in this thesis is capable of generating RVEs with random distribution of fibers in long-fiber reinforced composites, more properly laminates with a desired fiber volume fraction, width and height of the RVE, providing an extension to another algorithm that generates 3D RVEs with a desired ply orientation. This orientation depends on an input variable named *rotation* that will be explained in detail later on the thesis.

3.1.1 Bi-dimensional RVE

This algorithm represents a modification to the work of Catalanotti (2016) who developed one that creates cubic or quadrangular RVEs with random distributions of uniform spherical or circular particles. The algorithm has the aim of generating RVE-based micro-mechanical models for laminas. Lateral geometrical boundary periodicity is imposed. It is fast, and with the proper number of iterations it is able to represent the randomness of the material and to generate RVEs for laminas with any fiber volume fraction, i.e. from 0 to the maximum value that the combination of width and height the RVE has.

Like Catalanotti (2016), the main idea with the present work is to generate the random distribution, enforcing a perturbation of an ordered disposition of circles regularly arranged. The creation of the RVE also involves passing through three different processes:

- Compact RVE - Densest RVE that has all the circles in a form of a hexagonal packing;
- Initial RVE - Expanded RVE. It delimits all the boundaries of the RVE;
- Final RVE - RVE that suffered a perturbation that places the fibers to a randomly.

The next three sub-sections explain in a detailed way how these three RVEs are generated. The algorithm flowchart is reported in Figure 3.3 and it will be described in detail in the following Sub-sections.

Compact RVE

This compact RVE is formed by a periodic configuration of unit cells. These unit cells are formed by two circles with a radius r and with centers given by the following expressions:

$$\boldsymbol{v}_0 = \left\{ \begin{array}{c} 0 \\ r \end{array} \right\}, \qquad \boldsymbol{v}_1 = \left\{ \begin{array}{c} r \\ r(\sqrt{3}+1) \end{array} \right\} \tag{3.1}$$

After the creation of one unit cell, this one is replicated the same amount of times in the x direction, M, and in the y direction, N. So, a given circle in the compact RVE will have coordinates:

$$\boldsymbol{v}_i^{mn} = \left\{ \begin{array}{c} \boldsymbol{v}_{ix}^{mn} \\ \boldsymbol{v}_{iy}^{mn} \end{array} \right\} = \boldsymbol{v}_i + \left\{ \begin{array}{c} 2r(m-1) \\ 2\sqrt{3}r(n-1) \end{array} \right\} \tag{3.2}$$

where:

$$M = \left\lfloor \frac{H+2r}{4r} \right\rfloor \tag{3.3}$$

$$N = \left\lfloor \sqrt{\frac{Np_{trial}\sqrt{3}}{2}} \right\rfloor + 3 \tag{3.4}$$

H represents the changed width of the RVE, Np_{trial} represents the number of fibers that are in the Compact RVE according to its area and fiber volume fraction input, $m = 1, ..., M$ and $n = 1, ..., N$. The operator $\lfloor \cdot \rceil$ represents the Matlab round function.

Finally, the real number of fibers inside the RVE is given by:

$$N_p = 2.M.N \tag{3.5}$$

The following scheme explains the formation of the compact RVE:

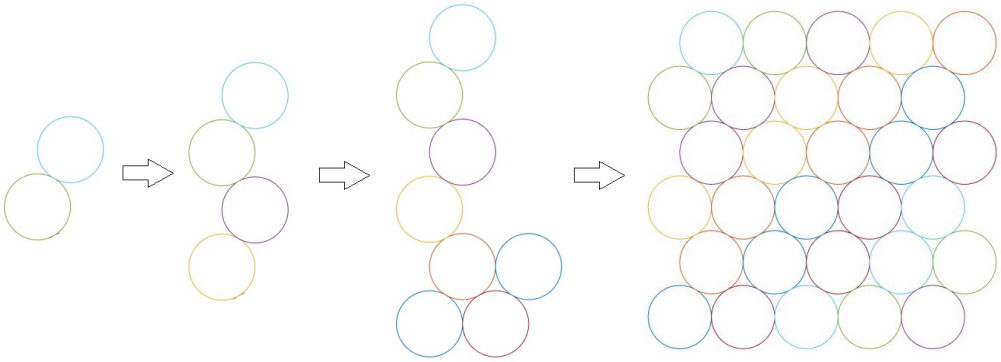

Figure 3.1: Scheme explaining the steps of the creation of the compact RVE.

Initial RVE

The RVE has dimensions (H, h), so, the coordinates of the circles inside the Initial RVE are obtained by multiplying the "compact" coordinates by two correction factors, one for the coordinate in x and another for y:

$$f_x = \frac{H}{L_x}, \qquad f_y = \frac{h - r}{L_y} \tag{3.6}$$

where:

$$L_x = 2rM, \qquad L_y = 2r\sqrt{3}N \tag{3.7}$$

So, a given circle in the initial RVE will have coordinates:

$$\bar{\boldsymbol{v}}_i^{mn} = \left\{ \begin{array}{c} \bar{v}_{ix}^{mn} \\ \bar{v}_{iy}^{mn} \end{array} \right\} = \left\{ \begin{array}{c} f_x v_{ix}^{mn} \\ f_y v_{iy}^{mn} \end{array} \right\} \tag{3.8}$$

It is important to notice that when the width of the RVE is larger than its height, i.e., a not so square RVE, the number of repetitions of the unit cells in the y direction, (N) can be too high for the RVE in question. In order to correct this, the algorithm is going to lower by one the Equation (3.4), until the combination of M by N becomes possible for the generation of the RVE. If N reaches zero, then the input of the fiber volume fraction is too high for the dimensions of the RVE that is being generated. The maximum theoretical value of the fiber volume fraction of a lamina depends strongly on its dimensions. Figure 3.2 shows the polynomial regression curve of the maximum fiber volume fraction *vs* the ratio h/H, considering H equal to $30r$:

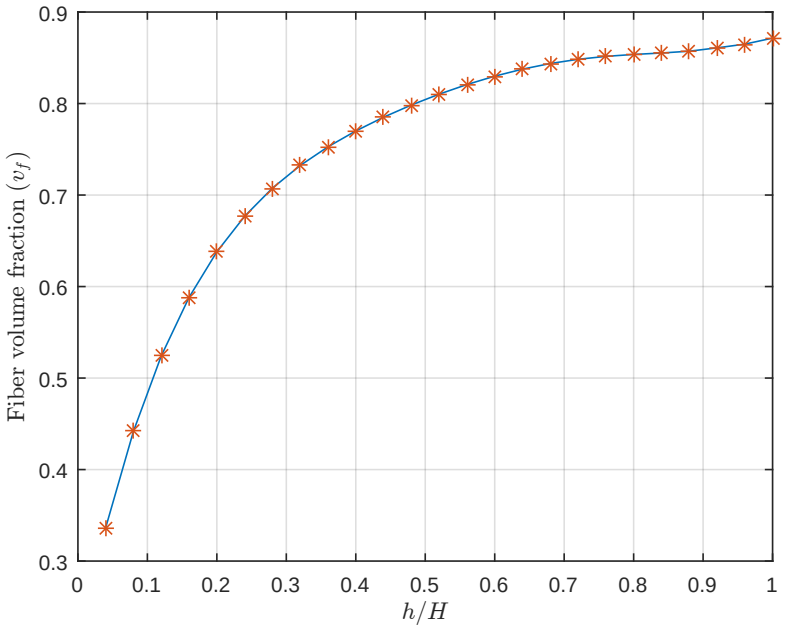

Figure 3.2: Dimensions of the RVE vs maximum fiber volume fraction.

With this said, it is possible that an input of the fiber volume fraction (v_f) is too high for the RVE in question. In order to avoid this whilst not stopping the algorithm from running, it is necessary to lower the input of the fiber volume fraction until it reaches a possible value for the configuration of the RVE.

Final RVE

The "Final RVE" represents the result of applying to all the fibers inside the Initial RVE a random displacement that is iterated K times. According to Catalanotti (2016) the fibers distribution, for a periodic RVE, is completely random for a number of iterations higher than ten, but since this RVE represents a lamina, i.e., with only periodic side boundaries, it is considered a completely random distribution of fibers with a number of iterations higher than twenty ($K \geq 20$). For every iteration, all the particles are randomly selected and moved according to a random displacement u that is defined by:

$$\boldsymbol{u} = \left\{ \begin{array}{c} u_x \\ u_y \end{array} \right\} = \left\{ \begin{array}{c} \rho \cos\theta \\ \rho \sin\theta \end{array} \right\} \tag{3.9}$$

where ρ represents the radial coordinate and $\theta = [0; 2\pi]$ the azimuthal angle in terms of polar coordinates. This ensures that all the bi-dimensional possible directions of the displacement are possible to achieve.

A condition is necessary to ensure that the fibers cannot interpenetrate and for that the euclidean distance (Equation (3.10)) between fibers (d_{ij}) cannot be higher than two times the radius.

$$d_{ij} = \sqrt{(\min\{|\bar{v}_i^x - \bar{v}_j^x|,\, H - |\bar{v}_i^x - \bar{v}_j^x|\})^2 + (\min\{|\bar{v}_i^y - \bar{v}_j^y|,\, h - |\bar{v}_i^y - \bar{v}_j^y|\})^2} \tag{3.10}$$

where $\bar{v}_i^x$, $\bar{v}_i^y$, $\bar{v}_j^x$ and $\bar{v}_j^y$ represent the x and y coordinates of the ith and jth fiber, respectively.

$$\rho = \rho - \Delta_\rho$$

Basically, the algorithm for the perturbation and formation of the "Final RVE" works in the following way:

- 1st - A value is defined for the variable ρ_{max} and for K;
- 2nd - The perturbation begins by choosing a random fiber inside the RVE and assigns the value $r/2$ and 0 to the variables $\Delta\rho$ and $\bar{\rho}$, respectively;
- 3rd - While $\bar{\rho} < \rho_{max}$, the variable $\bar{\rho}$ is increased by $\Delta\rho$ and it creates an initial displacement according to Equation (3.9) (with $\rho = \bar{\rho}$). It computes thee distance according to Equation (3.10) between the fiber in question and the others around it. If $d_{ij} < 2r$, then the variable $\bar{\rho}$ is decreased by $\Delta\rho$ and the value of $\Delta\rho$ is lowered by a desired increment (by default is 2). The "while" cycle finishes when $\bar{\rho}$ is higher than ρ_{max};
- 4th - The radial displacement variable ρ has a value between the interval $[0; \bar{\rho}]$ and the displacement is defined according to Equation (3.9);
- 5th - If the displacement plus the coordinates of the fiber in question is greater than the boundaries of the RVE, the displacement, $\boldsymbol{u}$ takes its maximum value, i.e.:

$$u_x = \begin{cases} h + r - \bar{v}_{ix}^{mn}, & \text{if } \bar{v}_{ix}^{mn} + u_x > H + r \\ -(\bar{v}_{ix}^{mn} + r), & \text{if } \bar{v}_{ix}^{mn} + u_x < -r \end{cases} \tag{3.11}$$

$$u_y = \begin{cases} h - r - \bar{v}_{iy}^{mn}, & \text{if } \bar{v}_{iy}^{mn} + u_y > h - r \\ -(\bar{v}_{iy}^{mn} - r), & \text{if } \bar{v}_{iy}^{mn} + u_y < r \end{cases} \tag{3.12}$$

- 6th - Finally, the coordinates of the "perturbated" fiber are given by:

$$\bar{\bar{\boldsymbol{v}}}_i^{mn} = \left\{ \begin{array}{c} \bar{\bar{v}}_{ix}^{mn} \\ \bar{\bar{v}}_{iy}^{mn} \end{array} \right\} = \left\{ \begin{array}{c} u_x \\ u_y \end{array} \right\} + \left\{ \begin{array}{c} \bar{v}_{ix}^{mn} \\ \bar{v}_{iy}^{mn} \end{array} \right\} \tag{3.13}$$

The flowchart of the presented algorithm is evidenced in Figure 3.3.

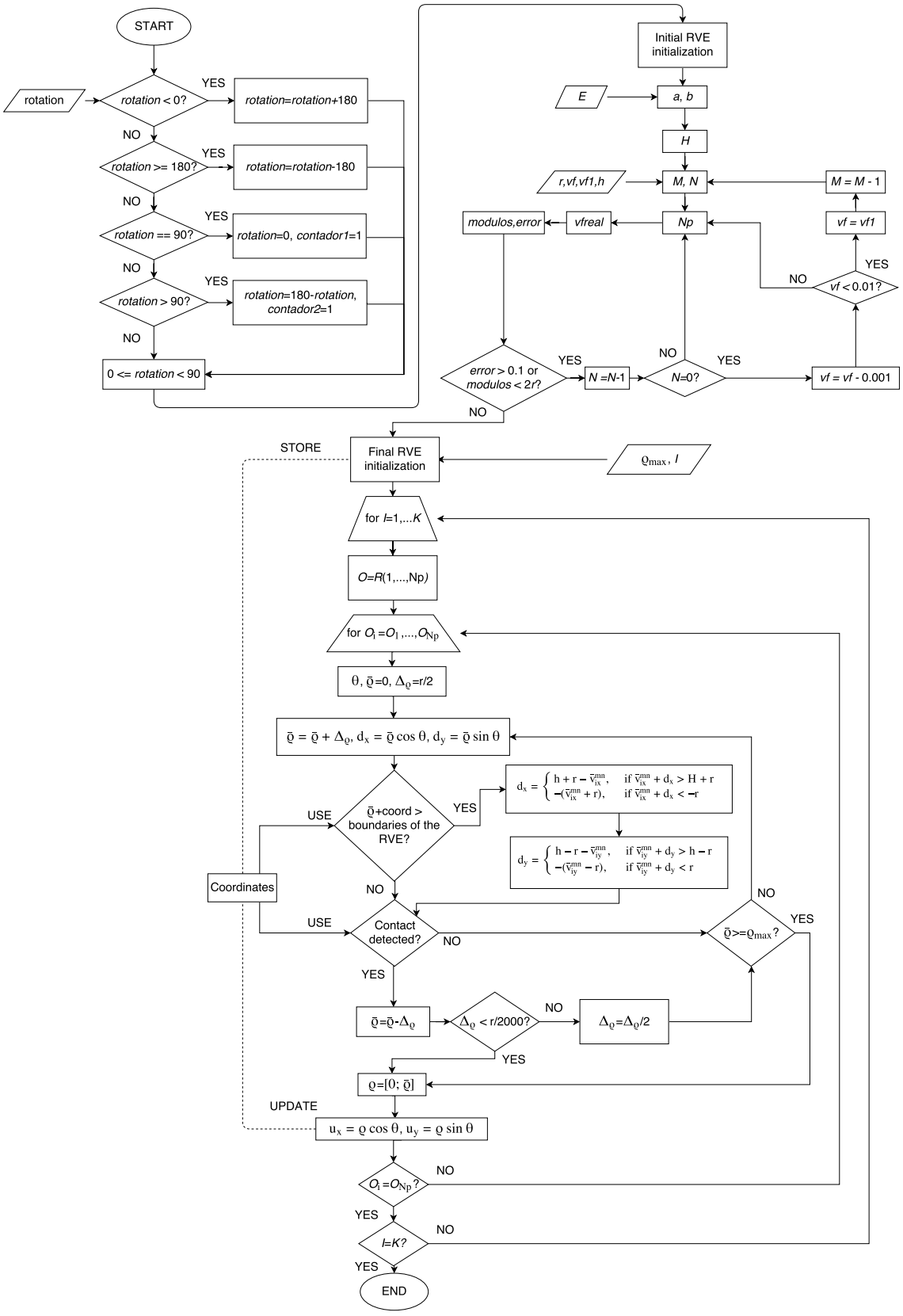

Figure 3.3: Flowchart of the Matlab algorithm.

In Figures 3.4 - 3.12, it is possible to see the differences between the Compact RVE, the Initial RVE and the Final RVE with a number of iterations equal to 25, a radius of the fibers equal to 8 μm, a width and height equal to 240 μm and 80 μm, respectively and for three different fiber volume fractions: 30%, 50% and 70%.

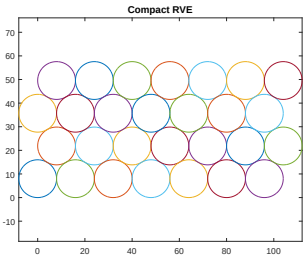

Figure 3.4: Compact RVE $v_f = 30\%$.

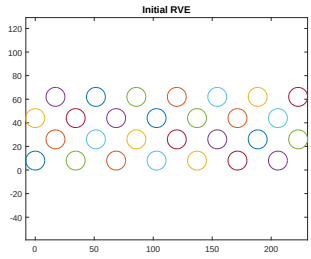

Figure 3.5: Initial RVE $v_f = 30\%$.

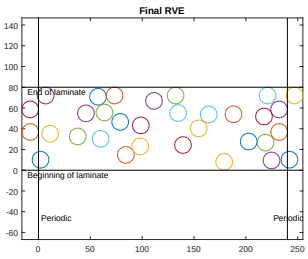

Figure 3.6: Final RVE $v_f = 30\%$.

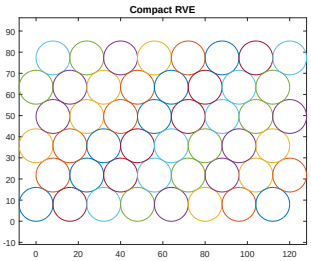

Figure 3.7: Compact RVE $v_f = 50\%$.

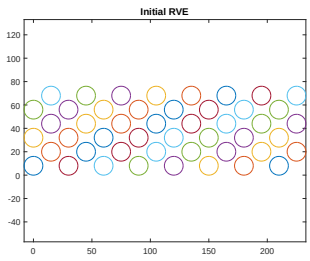

Figure 3.8: Initial RVE $v_f = 50\%$.

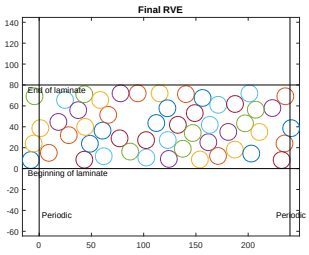

Figure 3.9: Final RVE $v_f = 50\%$.

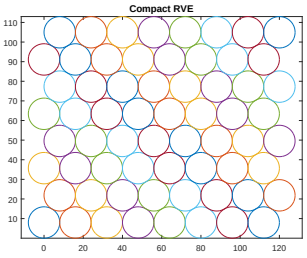

Figure 3.10: Compact RVE $v_f = 70\%$.

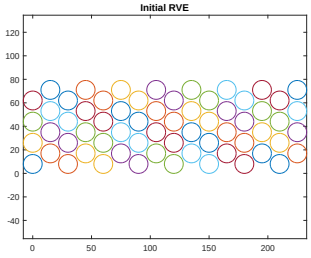

Figure 3.11: Initial RVE $v_f = 70\%$.

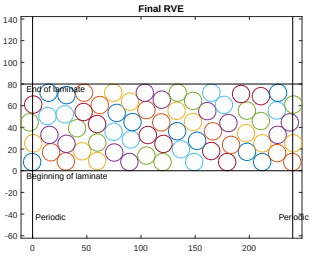

Figure 3.12: Final RVE $v_f = 70\%$.

3.1.2 Three-dimensional RVE

Initiation of the algorithm

After the geometry of the RVE is defined in a Matlab environment, it needs to be imported to the commercial software Abaqus® in order to run the proper simulations. For creating this "connection" between these two interfaces it is necessary to store the desired outputs that come from Matlab in a txt file. For this, it is used the "dlmwrite" Matlab command, which allows the creation of txt files with the variables needed, a delimiter between them and a desired decimal precision. The txt files generated are:

- *new_coordinates*.txt - file containing the (x, y) coordinates of the center of each fiber;
- *variables*.txt - file containing variables such as the radius of the fibers (r), number of the fibers (num_lines), the height (h), width (E), extrusion depth (DE) and the orientation $(rotation)$ of the RVE;

rotation is an input variable in the Matlab algorithm that characterizes the ply orientation. It is changed according to the beginning of the flow-chart presented in Figure 3.3. This variable is defined following a negative convention as it is evidenced in Figure 3.13,

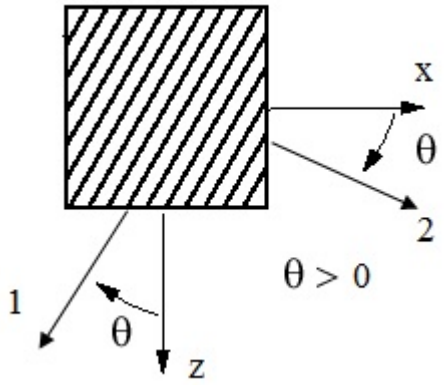

Figure 3.13: Convention used for the rotation variable.

where direction 1 represents the fiber direction, direction 2 the direction transversal to 1 and θ the *rotation* variable.

Now that the desired variables are stored, it needs to be written a Python script that loads these variables. Abaqus uses Python scripting to communicate between modules. Therefore, it is possible to use Python scripts to avoid using graphical interfaces (CAE and viewer) (ABAQUS, 2011). The script is made using the record of Abaqus CAE and Python programing.

In order to load the variables into the Abaqus environment, it is used the Python command ”open” in read only mode, where:

- f - variable that reads the *new_coordenadas*.txt;
- p - variable that reads the *variables*.txt

After this, it is possible to extract the desired information from these variables with the Python command ”readline()”. This command allows the extraction of the information following a certain order. It reads line by line the information stored in the read only variables. For example, if the first variable stored in the txt file is the radius of the fibers and the second the number of the fibers, the correct way to assign these two values to two variables in the Python script would be:

$$r = \text{float}(p.\text{readline}()) \qquad \text{and} \qquad num\_lines = \text{int}(p.\text{readline}())$$

These variables come from the txt file in a string numeric type. In order to turn them into a number it is used the ”float” or ”int” operation.

Geometry

Henceforth, it is evidenced how the 3D geometry is made for any value of the *rotation* input variable.

The Figures that appear in this chapter are of a RVE with a fiber volume fraction of 60%, a fiber radius of 3.5 μm, an extrusion depth of 35 μm, and the width and height are 105 μm and 35 μm, respectively.

The model involves the creation of four parts:

- Fibers_Prototype;
- Matrix_Prototype;
- Fibers;
- Matrix;

The first two are created in order to obtain the final parts, i.e. the last two. Fibers_Prototype represents the direct extrusion in the O_{xy} plane of the coordinates of the fibers (Figure 3.14). The creation of this part is developed disregarding the orientation of the ply.

The next step involves the creation of the Matrix_Prototype part. To avoid unwanted computation time, the algorithm regarding the creation of the geometry of the RVE is divided by four ”if” conditions. These conditions are intended to separate the RVEs that have different orientations, specifically, for $rotation = 0$, $0 < rotation < 90$, $rotation = 90$ and $90 < rotation < 180$.

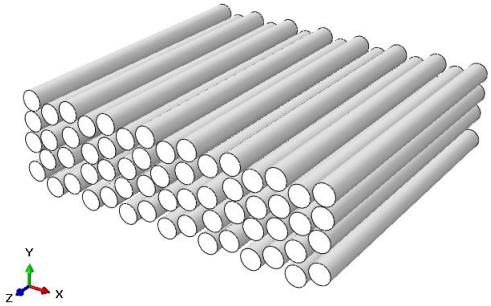

Figure 3.14: Fibers_Prototype part.

In the Matlab algorithm there is a condition that increases the rotation of the lamina by an angle of 180° if the variable is lower than 0.

$$\boldsymbol{rotation = 0}$$

For this case, the Matrix_Prototype part represents a simple parallelepiped with dimensions of (E, h, DE).

The Matrix and Fibers parts are generated using Boolean operations provided by Abaqus/Python programming. The Matrix part (Figure 3.16) is formed by a Boolean operation between the Matrix_Prototype and the Fibers_Prototype part. Fibers part (Figure 3.15) is formed by another Boolean operation between the Matrix and the Matrix_Prototype part.

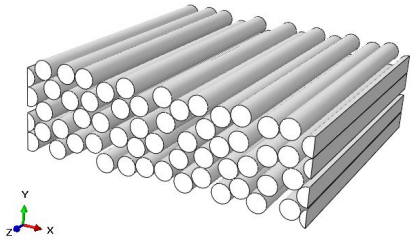

Figure 3.15: Fibers part (0°).

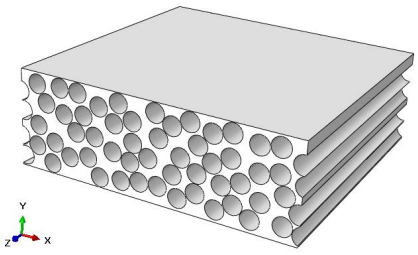

Figure 3.16: Matrix part (0°).

The final assembly is evidenced in Figure 3.17.

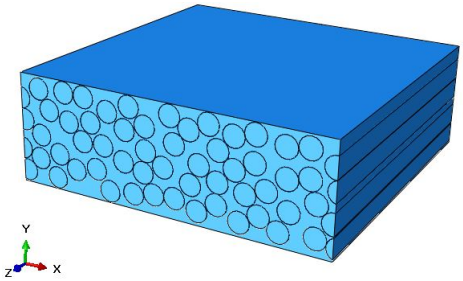

Figure 3.17: Assembly of the 0° *part.*

$0 < rotation < 90$

For this case, the Matrix_Prototype part is created using a rectangle in the O_{xy} plane with the dimensions (H, DE), (where H is defined bellow) and inside of it, another, but slightly smaller rectangle with the same center is created (Figure 3.18). This smaller rectangle is now positively rotated by an angle equal to the *rotation* input variable (Figure 3.19) and then the lower three vertices of the smaller rectangle are to be coincident with the sides of the first one, as it is evidenced in Figure 3.20.

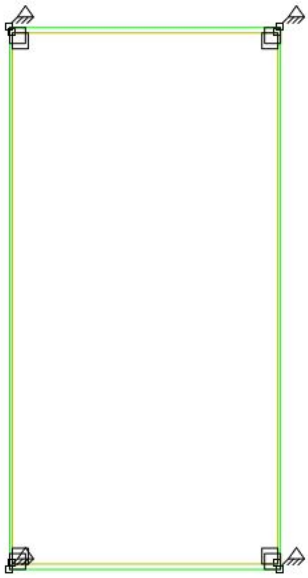

Figure 3.18: First sketch.

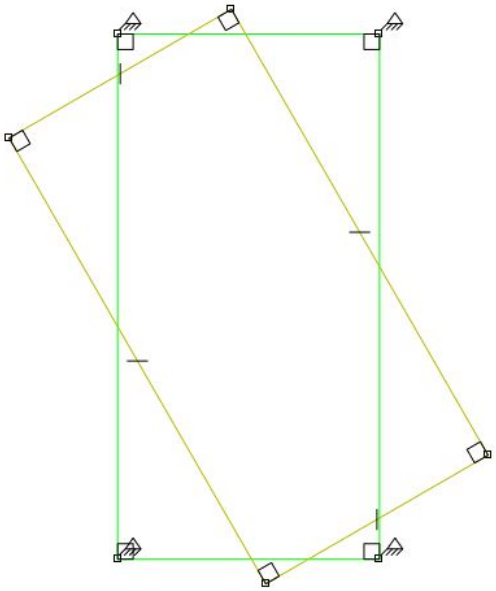

Figure 3.19: Second sketch.

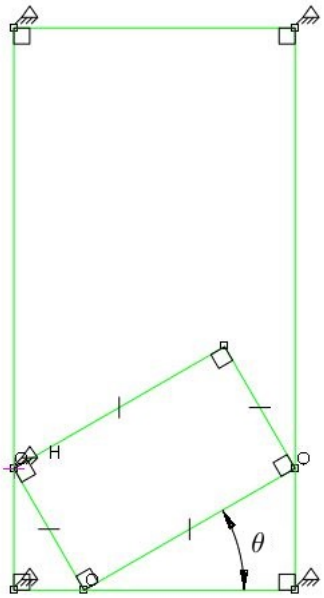

Figure 3.20: Third sketch.

The larger rectangle is deleted and the small one represents the new sketch for the creation of the RVE (Figure 3.21) with the following variable relations:

$$a = E\cos(\theta) \tag{3.14}$$

$$b = a\frac{\tan(\theta)}{\tan(\frac{\pi}{2} - \theta)} \tag{3.15}$$

$$H = a + b \tag{3.16}$$

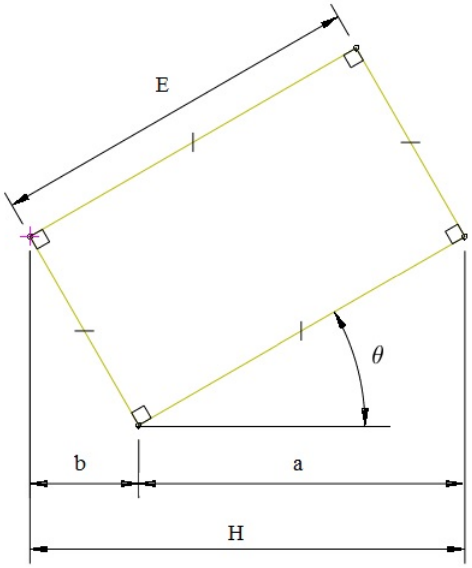

Figure 3.21: Fourth sketch.

The Equations (3.14), (3.15) and (3.16) are all defined *a priori* in the Matlab algorithm.

After the sketch is created it is extruded with an extrusion depth equivalent to the height (h) of the lamina and rotated 90°, because now the base of the part is in the O_{xy} plane and not in the O_{xz} plane (Figure 3.22 - 3.23).

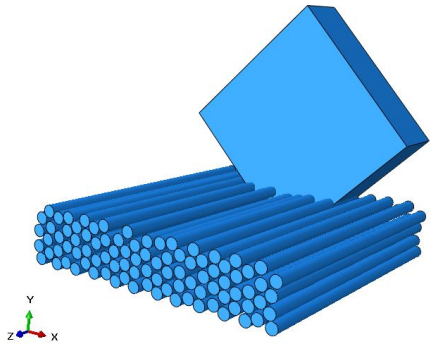

Figure 3.22: Assembly before the 90° rotation.

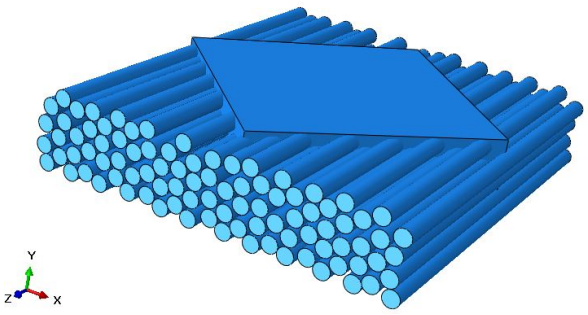

Figure 3.23: Assembly after the 90° rotation.

To create the Matrix and Fibers part, the same logic is applied for the case of $rotation = 0$, i.e. the parts are generated using the same Boolean operations.

Figures 3.24 - 3.26, represent the Matrix and Fibers parts of RVEs with a orientation of 30, 45 and 60 degrees:

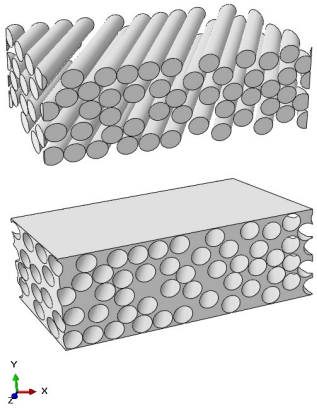

Figure 3.24: 30° *parts.*

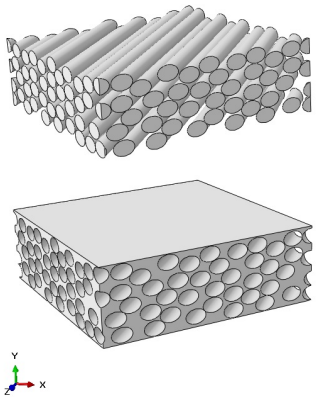

Figure 3.25: 45° *parts.*

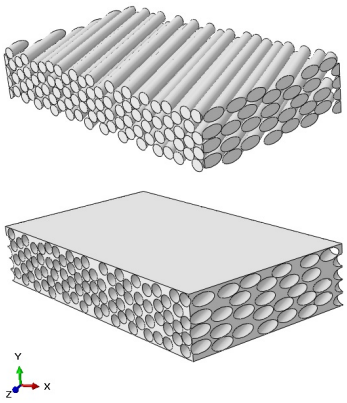

Figure 3.26: 60° *parts.*

The final assemblies can be evidenced in Figures 3.27 - 3.29:

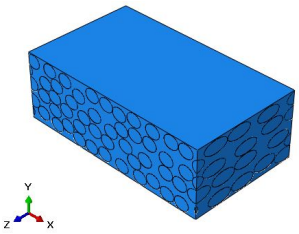

Figure 3.27: Assembly of the 30° *parts.*

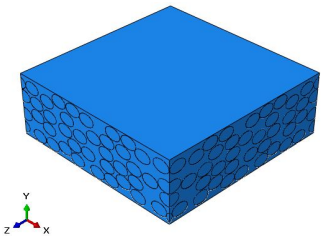

Figure 3.28: Assembly of the 45° *parts.*

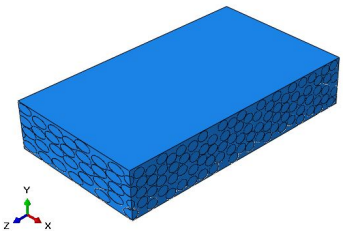

Figure 3.29: Assembly of the 60° *parts.*

***rotation* = 90**

The difference between this case and the case of $rotation = 0$ resides in the Python algorithm. The Fibers_Prototype part is rotated 90°. For the creation of the Matrix_Prototype part, it is created a parallelepiped in the O_{xy} plane with dimensions (E, h). In this case, the RVE has to have a quadrangular base, otherwise it is not possible to have a RVE with all the generated fibers, so the extrusion depth of the parts has to be equal to the width of the RVE.

After doing the same Boolean operations the parts are obtained as follows:

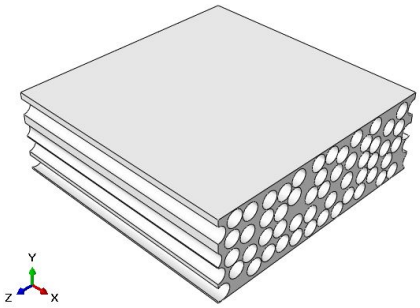

Figure 3.30: Matrix part (90°).

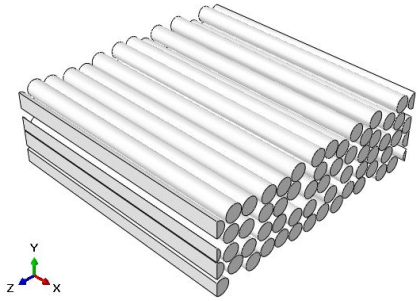

Figure 3.31: Fibers part (90°).

The final assembly is represented in the following figure:

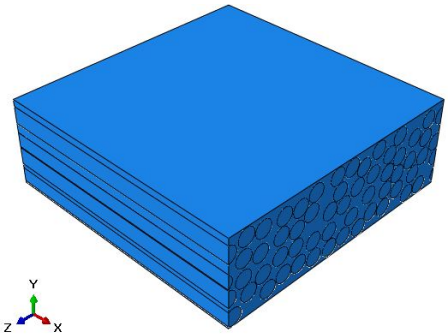

Figure 3.32: Final assembly (90°).

$90 < rotation < 180$

For this case, the creation procedure of the geometry of the RVE is exactly the same as for the case of $0 < rotation < 90$. The only difference lays on the rotation that the final assembly is submitted to, i.e., a rotation of $-180°$ around the z axis. In terms of how the algorithm works, the *rotation* input variable is defined in Matlab as an angle higher than 90 degrees but, as soon as the algorithm identifies it, the variable becomes equal to $180 - rotation$. This way, the generation of the RVE in the Matlab algorithm is the same as for the case of $0 < rotation < 90$, but in the Python algorithm the *rotation* variable has its original value in order to enter in the proper "if" condition. After entering the proper condition, the *rotation* variable is now, again, equal to $180 - rotation$. At this point, the RVE is created following the logic used for the case of $0 < rotation < 90$, but in the end it is rotated $-180°$. Figure 3.33 summarizes the previous explanation for the case of $rotation = 130$.

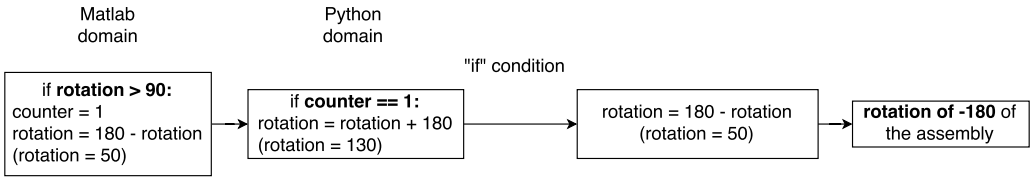

Figure 3.33: Scheme explaining the phases of the rotation variable of a RVE with a orientation higher than 90°.

Figures 3.34 and 3.35 represent the ply before and after the −180° rotation, respectively.

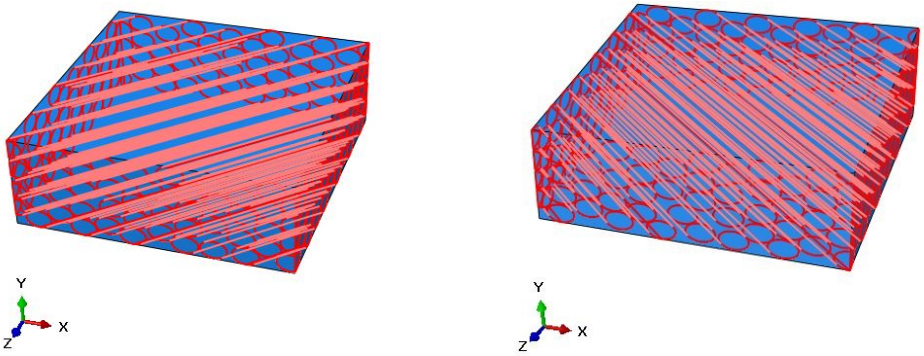

Figure 3.34: Assembly before the −180° *rotation. Figure 3.35: Assembly after the* −180° *rotation.*

This single-ply RVE is used for the creation of the hybrid models, however, the ply alone is not used in any simulations in this thesis. Some works may involve the study of the single-ply RVE, so the algorithm to generate it, as well as the identification of all the surfaces regarding the interactions between the fibers and matrix is at disposal in a different file of the hybrid models (see Appendix B).

3.2 Generation of the Hybrid Models

All the models presented are composed by a RVE that describes the inhomogeneities of the micro-structure and homogenized parts that are intended to simulate the mesoscopic elastic behavior of the RVE. In this case, in order to simulate inter-laminar damage, this RVE is composed of two plies with a $-\theta°/\theta°$ orientation. Figures 3.36 - 3.41 represent the Fibers and Matrix parts of double-ply RVE for the cases of stacking orientation of 0°/0°, 0°/90° and −45°/45°.

The development of the $-\theta°/\theta°$ RVE is done by creating a copy of the Matrix and Fibers part, translating them above the existent RVE and rotating them with an angle correspondent to 180° in the O_{xy} plane.

The homogenized parts are modeled as simple blocks that have the meso-mechanical effective properties of the constituents at the micro-scale. They are considered to be transversal isotropic materials and their properties are justified in Chapter 5.

The double-ply RVE RVE is connected to the homogenized parts by tie constraints. These constraints simulate fully constrained contact behavior between the parts.

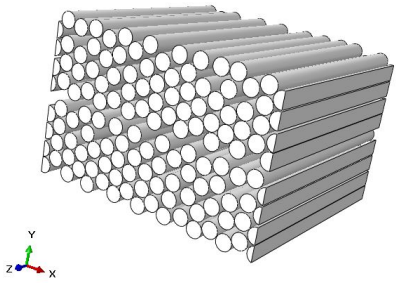

Figure 3.36: $0°/0°$ *Fibers part.*

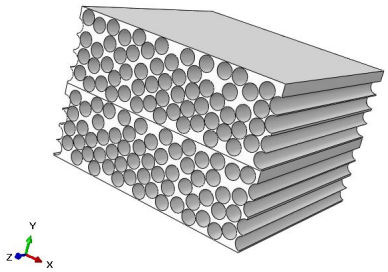

Figure 3.37: $0°/0°$ *Matrix part.*

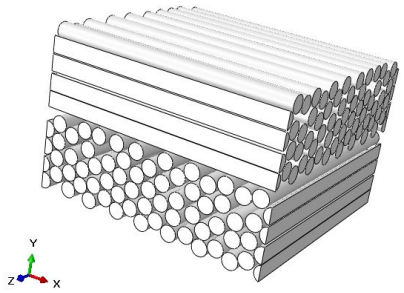

Figure 3.38: $0°/90°$ *Fibers part.*

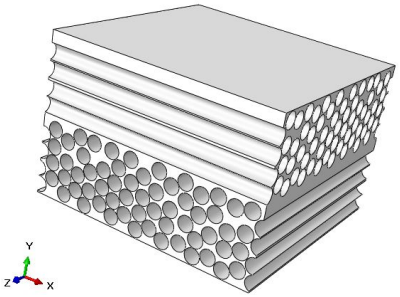

Figure 3.39: $0°/90°$ *Matrix part.*

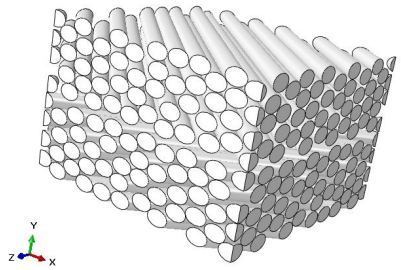

Figure 3.40: $-45°/45°$ *Fibers part.*

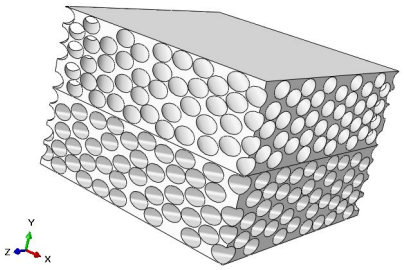

Figure 3.41: $-45°/45°$ *Matrix part.*

The algorithm is capable of identifying all surfaces needed to complete the model, such as the locations to apply all the boundary conditions, all the fibers/matrix interfaces, and is capable to generate the mesh for all the parts in the assembly, with a desired size for the elements in cause. Since the matrix represents a complex geometrical part, the type of elements used to mesh it are tetrahedrons and due to the existing interactions between the fibers and the matrix, the type and size of elements used to mesh both parts have to be the same, and all the existing nodes in the interfaces of the parts need to be coincident (Figure 3.42), i.e. the mesh must be conform. These models involve large deformations, thus implicating possible element distortions, another reason to chose this type of element is that they are less sensitive to distortion (ABAQUS, 2011).

The homogenized parts are simple geometrical ones, so the elements used are structured hexahedrons. They have the same width and height of the RVE, however, their length depend on a input variable named *dcb_depth*.

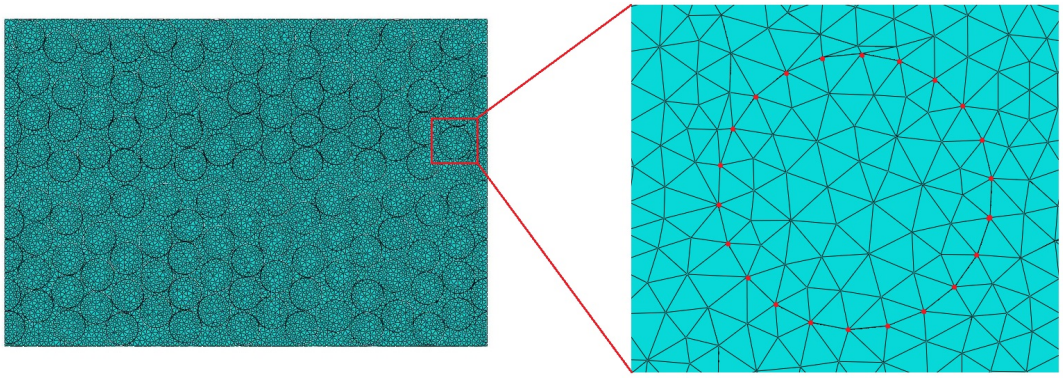

Figure 3.42: Evidence of a conform mesh.

3.2.1 DCB

Because the DCB test evaluates mode I fracture, the model most apply an appropriate normal opening load. To accomplish this, a normal displacement is applied to the upper edge and all displacements are fixed in the lower edge (Figure 3.43).

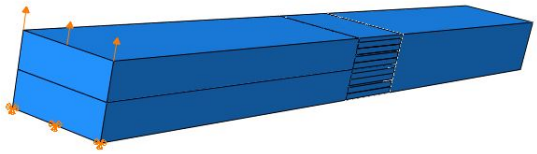

Figure 3.43: Boundary conditions applied to the DCB model.

Figures 3.44 - 3.46 show how the model deforms with the applied loading conditions.

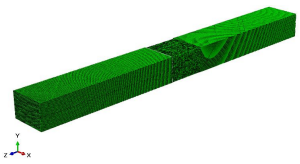

Figure 3.44: Initial position (DCB).

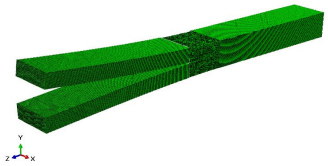

Figure 3.45: Intermediate position (DCB).

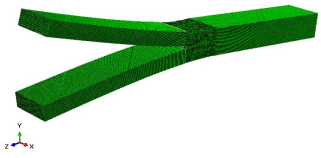

Figure 3.46: Final position (DCB).

3.2.2 ENF

The ENF is an experimental test that evaluates mode II fracture. The model is subjected to a vertical displacement at its middle length. The initial crack length is higher than 70% of half of its total length ($\frac{a_0}{L} > 0.7$) (Carlsson et al. (1986)). The displacements are fixed in the bottom edges, except in the longitudinal direction in

one of the edges(right-hand side in Figure 3.47), so the model csn deform freely in the longitudinal direction (Figure 3.47).

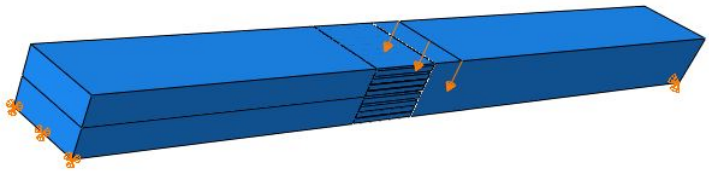

Figure 3.47: Boundary conditions applied to the ENF model.

Figures 3.48 - 3.50 show how the ENF model deforms with the applied loading conditions.

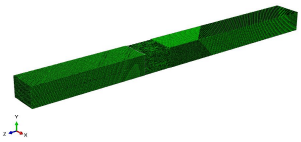

Figure 3.48: Initial position (ENF).

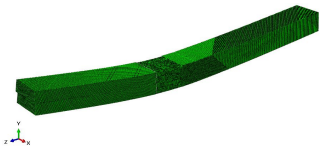

Figure 3.49: Intermediate position (ENF).

Figure 3.50: Final position (ENF).

3.2.3 MMB

The MMB test evaluates mixed-mode behavior, i.e. a combination of mode I and II simultaneously. An opening displacement is applied at the pre-cracked end of the model, while at the center, a vertical displacement conducts to the desired shearing loading at the crack tip. Like the ENF model, the displacements are fixed in the bottom edges, except in the longitudinal direction in one of the edges, so the model is able to deform freely in that direction (Figure 3.51).

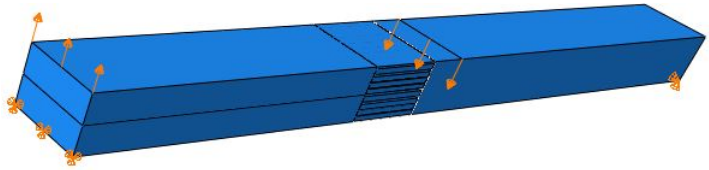

Figure 3.51: Boundary conditions applied to the MMB model.

Figures 3.52 - 3.54 show how the MMB model deforms with the applied loading conditions.

Figure 3.52: Initial position (MMB).

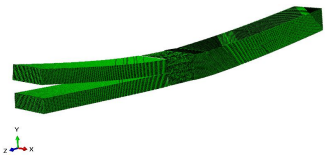

Figure 3.53: Intermediate position (MMB).

Figure 3.54: Final position (MMB).

Chapter 4

Constitutive Models

To simulate the micro-mechanical behavior of composite materials it is necessary to develop material models that are able to represent the behavior of the constituents in the composite. This chapter will be dedicated to the analytical definition and description of the damage and material modeling of the matrix, i.e., the surrounding material, as well as the interface between the fibers and matrix.

In this thesis, a simple transversely isotropic, linear-elastic constitutive model is used to simulate the individual reinforcing carbon fibers. The fibers are assumed to be linear-elastic and without any damage model, because the case in study treats delamination and in this type of failure mechanism, what can happen is the debond between the fibers and matrix, the crack of the matrix material or both, so there is no need to treat the reinforcing material as a different type.

The material model used for the matrix is the one developed by Bai et al. (2015), which is a damage model with plasticity based on a modified paraboloid yield criteria, able to capture the thermal and strain-rate dependency in the matrix behavior. The damage model for the matrix is based on the work of Melro et al. (2013a).

4.1 Matrix

4.1.1 Elasto-plastic model

Linear elastic behavior

The initial elastic behavior is defined by a linear relation between the stress tensor, $\boldsymbol{\sigma}$, and the elastic strain, $\boldsymbol{\varepsilon}^e$:

$$\boldsymbol{\sigma} = \boldsymbol{D}^e : \boldsymbol{\varepsilon}^e, \tag{4.1}$$

where $\boldsymbol{D^e}$ is the elasticity fourth-order tensor. For an isotropic matrix and in terms of the deviatoric stress tensor, $\boldsymbol{S}$, and hydrostatic stress, $p = \frac{1}{3}tr(\boldsymbol{\sigma})$, the elasticity law reads:

$$\boldsymbol{S} = 2G\boldsymbol{\varepsilon}_d^e \quad \text{and} \quad p = K\varepsilon_\nu^e, \tag{4.2}$$

where G is the shear modulos, K is the bulk modulus and $\boldsymbol{\varepsilon}_d^e$ and ε_ν^e, are, respectively, the elastic deviatoric strain tensor and elastic volumetric strain.

It is possible to write the elasticity law in a matrix form. Due to the symmetry relations of the deformation strain and stress tensors, $\boldsymbol{\sigma} = \boldsymbol{\sigma}^T$ and $\boldsymbol{\varepsilon}^e = \boldsymbol{\varepsilon}^{eT}$, the elasticity fourth-order tensor have a lower symmetry and considering the density function of the deformation energy in the elastic domain,

$$\mathscr{G} = \frac{1}{2}\boldsymbol{D}^e : \boldsymbol{\varepsilon}^e : \boldsymbol{\varepsilon}^e, \tag{4.3}$$

and with the property

$$\boldsymbol{\sigma} = \frac{\partial \mathscr{G}}{\partial \boldsymbol{\varepsilon}^e} \tag{4.4}$$

it is possible to write the elasticity law for an isotropic material utilizing *Voigt* notation:

$$\begin{Bmatrix} \sigma_{11} \\ \sigma_{22} \\ \sigma_{33} \\ \sigma_{23} \\ \sigma_{13} \\ \sigma_{12} \end{Bmatrix} = \begin{bmatrix} C_{11} & C_{12} & C_{12} & 0 & 0 & 0 \\ & C_{11} & C_{12} & 0 & 0 & 0 \\ & & C_{11} & 0 & 0 & 0 \\ & & & C_{44} & 0 & 0 \\ & & & & C_{44} & 0 \\ \text{sym.} & & & & & C_{44} \end{bmatrix} \begin{Bmatrix} \varepsilon_{11} \\ \varepsilon_{22} \\ \varepsilon_{33} \\ \gamma_{23} \\ \gamma_{13} \\ \gamma_{12} \end{Bmatrix}, \tag{4.5}$$

For isotropic materials, the elastic behavior it is independently of the direction. The following relationships are verified for isotropic materials:

$$E_1 = E_2 = E_3 = E; \qquad \nu_{12} = \nu_{13} = \nu_{23} = \nu; \qquad G_{12} = G_{13} = G_{23} = G \tag{4.6}$$

In total, the elastic behavior of an isotropic material is simply defined by two elastic constants, since

$$G = \frac{E}{2(1+\nu)} \tag{4.7}$$

So, the elastic tensor components, C_{ij} are defined by:

$$\begin{aligned} C_{11} &= \frac{E(1-\nu)}{(1+\nu)(1-2\nu)}, \\ C_{12} &= \frac{E\nu}{(1+\nu)(1-2\nu)}, \\ C_{44} &= G \end{aligned} \tag{4.8}$$

Thermo-visco-plastic behavior

The constitutive law for the matrix material is based on the recent work by Bai et al. (2015) that presented a micro-scale analysis of a new constitutive law for the matrix material taking into account the pressure dependence of the material as well as strain-rate and temperature dependence. It is based on an extension to the classical paraboloidal yield criterion proposed by Tschoegl (1971), so that the

predictive ability of the micro-scale analysis is improved. This modification takes into account the shear yield behavior and is defined by the following expression:

$$f(\boldsymbol{\sigma}, \sigma_{Y_C}, \sigma_{Y_T}, \sigma_{Y_S}) = a(J_2^3 + bJ_3^2)^{\frac{1}{3}} + 2(\sigma_{Y_C} - \sigma_{Y_T})I_1 - 2\sigma_{Y_C}\sigma_{Y_T} \tag{4.9}$$

where σ_{Y_C} and σ_{Y_T} are the absolute values of compressive and tensile yield, $I_1 = tr(\boldsymbol{\sigma}_{ij})$ is the first stress invariant, $J_2 = \frac{1}{2}\boldsymbol{s}_{ij}\boldsymbol{s}_{ij}$ and $J_3 = \det(\boldsymbol{s}_{ij})$ are the second and third invariant of the deviatoric stress tensor and a and b are two interdependent parameters that can be determined with only one additional experimental test. By considering $\sigma_2 = \sigma_3 = 0$ (uniaxial tensile test in Equation 4.9 it is possible to obtain the relationship between a and b:

$$a = 6\left(\frac{27}{4b + 27}\right)^{\frac{1}{3}} \tag{4.10}$$

And it is possible to obtain the relation between the parameter b with the shear yield strength σ_{Y_S} by considering the pure shear stress state ($\sigma_1 = -\sigma_2$) and $\sigma_3 = 0$ in Equation (4.9):

$$b = \frac{1}{4}\left(\frac{(3\sigma_{Y_S})^6}{(\sigma_{Y_C}\sigma_{Y_T})^3} - 27\right) \tag{4.11}$$

For more information about the derivation of a or b see Bai et al. (2015).
It is observed that the variation of b has no effect on the compressive, tensile and biaxial yield strengths, but has on the shear yield strength. A non-associative flow rule (Melro et al. (2013a)) was used allowing for a correct definition of the volumetric deformation in plasticity:

$$\mathrm{g} = \sigma_{vm}^2 + \alpha p^2 \tag{4.12}$$

where $\sigma_{vm} = \sqrt{3J_2}$ is the Von Mises equivalent stress, $p = \frac{1}{3}I_1$ is the hydrostatic pressure and α is a material parameter responsible for the correct definition of the volumetric component of the plastic flow and it is given by the following equation:

$$\alpha = \frac{9}{2}\frac{1 - 2\nu_p}{1 + \nu_p} \tag{4.13}$$

with ν_p being the plastic Poisson's ration. It is possible to write the increment in plastic deformation via the flow rule that used the plastic potential given in Equation 4.12:

$$\Delta\varepsilon^p = \Delta\lambda\frac{\partial \mathrm{g}}{\partial\sigma} \tag{4.14}$$

with $\Delta\lambda$ being the plastic multiplier, subjected to the Kuhn-Tucker consistency conditions and to be updated via the return mapping algorithm (de Souza Neto et al., 2008).

The criterion depends on the compressive, tensile and shear yield strengths, so these values need to be updated according to the corresponding hardening laws that depend on the equivalent plastic strain:

$$\sigma^*_{Y_i} = h_i(\varepsilon^p_e), \quad i = C,T \text{ or } S \tag{4.15}$$

where the superscript * is used to indicate that these yield strengths are calculated for reference values of strain-rate and temperature.
The equivalent plastic strain ε^p_e is defined as:

$$\varepsilon^p_e = \sqrt{\frac{1}{1+2\nu_p^2}\varepsilon^p : \varepsilon^p} \tag{4.16}$$

After the hardening behavior is defined for the reference conditions, Bai et al. (2015) proposed phenomenological scaling laws to account for the influence of temperature and strain-rate on the material response:

$$\sigma_{Y_i} = \sigma^*_{Y_i}\left(1+\alpha_i \log\frac{\dot{\varepsilon}^p_e}{\dot{\varepsilon}^{p*}_e}\right)\left(1+\beta_i \log\frac{T}{T^*}\right), \quad i = C,T \text{ or } S \tag{4.17}$$

where σ_{Y_i} are the predicted yield stresses at the desired temperature T and strain-rate $\dot{\varepsilon}^p_e$ and T^* are the reference temperature strain-rate, respectively. The material constants α_i and β_i are determined experimentally by scaling back to the reference state each stress-strain curve that is obtained for the different strain-rates and temperatures.

This material model provided by Bai et al. (2015) was implemented in a VUMAT subroutine of the commercial finite element analysis software Abaqus®.

4.1.2 Damage model

The constitutive law to model the damage of the matrix part is based on the work by Melro et al. (2013a) that presented a pressure dependent, elasto-plastic thermodynamically consistent damage model. This model only uses one damage variable, d_m, that affects the stiffness of the material once activated. The authors of this article proposed the following definition for the complementary free energy density of the material,

$$\mathscr{G}_m = \frac{\sigma_{11}^2+\sigma_{22}^2+\sigma_{33}^2}{2E_m(1-d_m)} - \frac{\nu_m}{E_m}(\sigma_{11}\sigma_{22}+\sigma_{22}\sigma_{33}+\sigma_{33}\sigma_{11}) + \\ + \frac{1+\nu_m}{E_m(1-d_m)}(\sigma_{12}^2+\sigma_{13}^2+\sigma_{23}^2) + \mathscr{G}^p_m \tag{4.18}$$

where, E_m, ν_m and d_m are the Young's modulus, the Poisson's ratio of the matrix and the damage variable for the matrix, respectively. According to Malvern (1969), this function must be a scalar one, positive definite and it must be zero at the origin with respect to the stresses. The quantity $\mathscr{G}^p_m$ represents the contribution of plastic flow to the stored energy. To ensure that the damage process is irreversible it is necessary to guarantee that the rate of change of the complementary free energy density is greater than the externally applied stress:

$$\dot{\mathscr{G}} - \dot{\boldsymbol{\sigma}} : \boldsymbol{\varepsilon} \geq 0 \tag{4.19}$$

which can be written as

$$\left(\frac{\partial \mathscr{G}_m}{\partial \boldsymbol{\sigma}} - \boldsymbol{\varepsilon}\right) : \dot{\boldsymbol{\sigma}} + \frac{\partial \mathscr{G}_m}{\partial d_m}\dot{d}_m \geq 0. \tag{4.20}$$

To ensure a positive dissipation of mechanical energy it is necessary that the strain tensor to be equal to the derivative of the complementary free energy density with respect to the stress tensor,

$$\boldsymbol{\varepsilon} = \frac{\partial \mathscr{G}_m}{\partial \boldsymbol{\sigma}} = \frac{\boldsymbol{\sigma}}{2G_m(1-d_m)} - \frac{\nu_m d_m}{E_m(1-d_m)}\boldsymbol{I}\cdot\boldsymbol{I} : \boldsymbol{\sigma} - \frac{\nu_m}{E_m} I_1 \boldsymbol{I} \tag{4.21}$$

where G_m is the shear stiffness of the matrix. The terms in Equation (4.21) can be rearranged in order to obtain the compliance tensor of the material:

$$\boldsymbol{H}_m = \frac{\partial^2 \mathscr{G}_m}{\partial \boldsymbol{\sigma}^2} = \begin{bmatrix} \frac{1}{E_m(1-d_m)} & -\frac{\nu_m}{E_m} & -\frac{\nu_m}{E_m} & 0 & 0 & 0 \\ & \frac{1}{E_m(1-d_m)} & -\frac{\nu_m}{E_m} & 0 & 0 & 0 \\ & & \frac{1}{E_m(1-d_m)} & 0 & 0 & 0 \\ & & & \frac{1}{G_m(1-d_m)} & 0 & 0 \\ & & & & \frac{1}{G_m(1-d_m)} & 0 \\ \text{sym.} & & & & & \frac{1}{G_m(1-d_m)} \end{bmatrix} \tag{4.22}$$

where the stiffness tensor, $\boldsymbol{C}_m$ can be defined inverting the compliance tensor:

$$\boldsymbol{C}_m = \begin{bmatrix} G_d & \lambda_d & \lambda_d & 0 & 0 & 0 \\ & G_d & \lambda_d & 0 & 0 & 0 \\ & & G_d & 0 & 0 & 0 \\ & & & G_m(1-d_m) & 0 & 0 \\ & & & & G_m(1-d_m) & 0 \\ \text{sym.} & & & & & G_m(1-d_m) \end{bmatrix} \tag{4.23}$$

where the parameters G_d and λ_d are given by:

$$\begin{aligned} G_d &= \frac{E_m(1-d_m)(1-\nu_m(1-d_m))}{(1+\nu_m(1-d_m))(1-2\nu_m(1-d_m))}, \\ \lambda_d &= \frac{E_m\nu_m(1-d_m)^2}{(1+\nu_m(1-d_m))(1-2\nu_m(1-d_m))} \end{aligned} \tag{4.24}$$

Damage onset is defined by the following damage activation function,

$$F_m^d = \phi_m^d - r_m \tag{4.25}$$

where ϕ_m^d represents the loading function and r_m is an internal variable related with the damage variable and it is equal to one before damage activation and higher than one if damage is activated.

The loading function is defined by:

$$\phi_m^d = \frac{3\tilde{J}_2}{X_m^c X_m^t} + \frac{\tilde{I}_1(X_m^c - X_m^t)}{X_m^c X_m^t} \tag{4.26}$$

where X_m^c and X_m^t represent the compressive and tensile strengths of the material, while the invariants $\tilde{J}_2$ and $\tilde{I}_1$ are determined using the effective stress tensor according to:

$$\tilde{\boldsymbol{\sigma}} = (\boldsymbol{H}_m^0)^{-1} : \boldsymbol{\varepsilon} \tag{4.27}$$

where $\boldsymbol{H}_m^0$ is the compliance tensor of the undamaged material, which can be obtained by forcing the damage variable to be equal to zero, d_m=0.

The internal variable r_m is defined by

$$r_m = \max\left\{1, \max\{\phi_{m,t}^d\}\right\} \tag{4.28}$$

After damage onset, the evolution of damage can be measured by the rate of energy dissipation per unit volume:

$$\Xi_m = \frac{\partial \mathscr{G}}{\partial d_m}\dot{d}_m = Y_m \dot{d}_m \geq 0 \tag{4.29}$$

The damage activation function (Equation (4.25)) it has a value lower than zero if the model is in the elastic-plastic regime and when the damage criterion is activated it is zero. It is similar to the paraboloidal yield criterion used in this article (Melro et al., 2013a), but it is used the final compressive and tensile strengths of the epoxy matrix instead of yield strengths and the concept of effective stress tensor, i.e., the stress tensor calculated using the undamaged stiffness tensor.

To avoid damage localization (mesh size dependency), Bažant's crack band model (Oh and B., 1983) was implemented along with the definition of the damage evolution law. By making use of the characteristic length of the finite element and the fracture toughness, it is possible to regularize the amputated dissipated energy of the matrix, as the following:

$$\Psi_m = \int_0^\infty Y_m \dot{d}_m \, \mathrm{d}t = \int_1^\infty \frac{\partial \mathscr{G}_m}{\partial d_m}\frac{\partial d_m}{\partial r_m} \, \mathrm{d}r_m = \frac{\mathcal{G}_m}{l^e} \tag{4.30}$$

where $\mathcal{G}_m$ is the energy release rate of the matrix, l^e is the characteristic element length and Y_m is the thermodynamic force associated with the variable d_m. Using the complementary free energy for the matrix, given by Equation (4.18), it is possible to define Y_m as:

$$Y_m = \frac{\partial \mathscr{G}_m}{\partial d_m} = \frac{\sigma_{11}^2 + \sigma_{22}^2 + \sigma_{33}^2}{2E_m(1-d_m)^2} + \frac{\sigma_{12}^2 + \sigma_{13}^2 + \sigma_{23}^2}{2G_m(1-d_m)^2} \geq 0 \tag{4.31}$$

that is always positive. The damage evolution law defined for the matrix is given by:

$$d_m = 1 - \frac{e^{A_m(3-\sqrt{7+2r_m^2})}}{\sqrt{7+2r_m^2}-2} \tag{4.32}$$

where the parameter A_m needs to be computed from solving Equation (4.30) as a function of the characteristic element length, therefore, this parameter must be computed for each element of the mesh. This damage evolution law has been chosen in order to force damage localization and strain softening on the material under a tensile load. The derivative of the damage law in order to r_m is given by:

$$\frac{\partial d_m}{\partial r_m} = \frac{2r_m e^{A_m(3-\sqrt{7+2r_m^2})}}{\sqrt{7+2r_m^2}(\sqrt{7+2r_m^2}-2)}\left(A_m + \frac{1}{\sqrt{7+2r_m^2}-2}\right) \tag{4.33}$$

The energy dissipated per unit volume for an uniaxial stress condition is obtained by integrating the rate of energy dissipation given by Equation (4.29). But first the relation between the effective stress and the real stress in a uniaxial case must be established. This is achieved by imposing the principle of strain equivalence (Rui Melro (2011)):

$$\left.\begin{aligned}\boldsymbol{\sigma} &= \boldsymbol{C}_m : \boldsymbol{\varepsilon}\\ \tilde{\boldsymbol{\sigma}} &= \boldsymbol{C}_m^0 : \boldsymbol{\varepsilon}\end{aligned}\right\} \boldsymbol{\sigma} = \boldsymbol{C}_m : (\boldsymbol{C}_m^0)^{-1} : \tilde{\boldsymbol{\sigma}} = \boldsymbol{C}_m : \boldsymbol{H}_m^0 : \tilde{\boldsymbol{\sigma}}$$

where $\boldsymbol{C}_m^0$ is the undamaged stiffness tensor. For the isotropic material in analysis, the relation between the stress tensor and the effective stress tensor is:

$$\boldsymbol{\sigma} = (1-d_m)\tilde{\boldsymbol{\sigma}} + \frac{d_m(1-d_m)\nu_m}{1+\nu_m(1-d_m)}\boldsymbol{I_4} : \left(\tilde{\boldsymbol{\sigma}} - \frac{\tilde{\boldsymbol{I_1}}}{1-2\nu_m(1-d_m)}\boldsymbol{I}\right) \tag{4.34}$$

where the fourth-order tensor $\boldsymbol{I}_4$ is defined in *Voigt* notation by:

$$\boldsymbol{I}_4 = \begin{bmatrix} 1 & 0 & 0 & 0 & 0 & 0\\ 0 & 1 & 0 & 0 & 0 & 0\\ 0 & 0 & 1 & 0 & 0 & 0\\ 0 & 0 & 0 & 0 & 0 & 0\\ 0 & 0 & 0 & 0 & 0 & 0\\ 0 & 0 & 0 & 0 & 0 & 0 \end{bmatrix} \tag{4.35}$$

Defining now the particular case of an uniaxial tensile load applied to the material, where the effective stress tensor is defined by:

$$\tilde{\boldsymbol{\sigma}} = \begin{bmatrix} \tilde{\sigma}_{11}\\ 0\\ 0\\ 0\\ 0\\ 0 \end{bmatrix} \tag{4.36}$$

For this stress state the three normal components of the real stress tensor are:

$$\sigma_{11} = \frac{(1-d_m)[1-\nu_m(1-d_m)(1+2\nu_m)]}{[1+\nu_m(1-d_m)][1-2\nu_m(1-d_m)]}\tilde{\sigma}_{11} \tag{4.37a}$$

$$\sigma_{22} = \sigma_{33} = \frac{-\nu_m d_m(1-d_m)}{[1+\nu_m(1-d_m)][1-2\nu_m(1-d_m)]}\tilde{\sigma}_{11} \tag{4.37b}$$

The remaining shear components of the stress tensor are equal to zero. Using Equations (4.37) in Equation (4.31) results in:

$$\frac{\partial \mathscr{G}_m}{\partial d_m}^{UN} = \frac{1}{2E_m} \frac{2\nu_m^2 d_m^2 + [1-\nu_m(1-d_m)(1+2\nu_m)]^2}{[1+\nu_m(1-d_m)]^2[1-2\nu_m(1-d_m)]^2} \tilde{\sigma}_{11} \tag{4.38}$$

Finally, the damage activation function defined for the uniaxial tensile case is given by:

$$F_m^{d^{UN}} = \frac{\tilde{\sigma}_{11}^2}{X_m^c X_m^t} + \frac{X_m^c - X_m^t}{X_m^c X_m^t} \tilde{\sigma}_{11} - r_m \leq 0 \tag{4.39}$$

As it has been said before, for damage to propagate, this equation needs to be equal to zero. Solving this equation in order to the applied effective stress results in:

$$\tilde{\sigma}_{11} = \frac{1}{2}\left[X_m^t - X_m^c + \sqrt{(X_m^c X_m^t)^2 + 4X_m^t X_m^c r_m}\right] \tag{4.40}$$

Using Equations (4.37), (4.38) and (4.40) in Equation (4.30) results in:

$$\begin{aligned} &\int_1^\infty \frac{1}{2E_m}\left(\frac{X_m^t - X_m^c + \sqrt{(X_m^c - X_m^t)^2 + 4X_m^t X_m^c r_m}}{2}\right)^2 \times \\ &\frac{2\nu_m^2 d_m^2 + [1-\nu_m(1-d_m)(1+2\nu_m)]^2}{[1+\nu_m(1-d_m)]^2[1-2\nu_m(1-d_m)]^2} \times \\ &\frac{2r_m e^{A_m(3-\sqrt{7+2r_m^2})}}{\sqrt{7+2r_m^2}(\sqrt{7+2r_m^2}-2)}\left(A_m + \frac{1}{\sqrt{7+2r_m^2}-2}\right) \mathrm{d}r_m = \frac{\mathcal{G}_m}{l^e} \end{aligned} \tag{4.41}$$

This equation must now be solved numerically using the secant method for non-linear equations, along with the definition of the damage evolution law in Equation (4.32), in order to solve it for the parameter A_m.

This damage model provided by Melro et al. (2013a) was implemented in a VUMAT subroutine of the commercial finite element analysis software Abaqus®.

4.2 Fibrous reinforcements

The fibers are assumed to have a linear-elastic behavior only, namely they represent a transversely isotropic material. This means that the elastic properties of the material in a symmetry it is independent of the direction. Starting in Equation (4.1) and doing the same operations that were done in Sub-section 4.1.1 for the matrix material, for a transversely isotropic material, the constitutive elastic tensor is characterized by five elastic constants. So, in this case, utilizing *Voigt* notation, the elasticity law can be defined in the following matrix form,

$$\begin{Bmatrix}\sigma_{11}\\ \sigma_{22}\\ \sigma_{33}\\ \sigma_{23}\\ \sigma_{13}\\ \sigma_{12}\end{Bmatrix} = \begin{bmatrix} C_{11} & C_{12} & C_{13} & 0 & 0 & 0 \\ & C_{11} & C_{13} & 0 & 0 & 0 \\ & & C_{33} & 0 & 0 & 0 \\ & & & C_{44} & 0 & 0 \\ & & & & C_{44} & 0 \\ \text{sym.} & & & & & \frac{1}{2}(C_{11}-C_{12}) \end{bmatrix} \begin{Bmatrix}\varepsilon_{11}\\ \varepsilon_{22}\\ \varepsilon_{33}\\ \gamma_{23}\\ \gamma_{13}\\ \gamma_{12}\end{Bmatrix}, \tag{4.42}$$

The constitutive elastic tensor has the same shape as the constitutive equivalent elastic tensor for transversely isotropic materials defined in Equation (2.25).

The elastic constants admit the following properties,

$$\begin{aligned} &E_1 = E_t, && E_2 = E_3 = E_p, \\ &\nu_{21} = \nu_{31} = \nu_{pt}, && \nu_{23} = \nu_p, \\ &G_{21} = G_{31} = G_{pt}, && G_{23} = G_p \end{aligned} \tag{4.43}$$

that allows to establish the following property

$$G_{23} = \frac{E_3}{2(1+\nu_{23})} \tag{4.44}$$

So, the elastic tensor components, C_{ij} are defined by:

$$\begin{aligned} C_{11} &= \frac{1-\nu_{pt}\nu_{tp}}{E_p E_t \Delta}, & C_{22} &= \frac{1-\nu_{pt}\nu_{tp}}{E_p E_t \Delta}, \\ C_{33} &= \frac{1-\nu_p^2}{E_p^2 \Delta}, & C_{12} &= \frac{\nu_p + \nu_{pt}\nu_{tp}}{E_p E_t \Delta}, \\ C_{13} &= \frac{\nu_{tp} + \nu_p \nu_{tp}}{E_p E_t \Delta}, & C_{44} &= G_{pt} \end{aligned} \tag{4.45}$$

where the subscript "p" and "t" denotes in "plane" and "transversal" to the isotropy plane, respectively and Δ is the determinant of the stiffness matrix.

4.3 Fibers/Matrix interface

Interface is the key region which determines, to a great extent, the set of properties of all heterogeneous systems, including composite materials. In a composite material, the fibers ensure the strength of the material, while the matrix helps to keep the shape of the part. The interface, as a key element of the composite, transfers the load from the matrix to the fibers and, thus, it is responsible for the effect of "reinforcement".

This interface is modeled using the cohesive surfaces of the FE commercial software Abaqus®. The cohesive surface behavior in terms of damage initiation is monitored by the quadratic stress criterion (Equation (2.31)) and in terms of damage evolution it is based on the energy that is dissipated as a result of the damage process, i.e. the fracture energy (or critical energy release rate) with an exponential softening (Figure 2.22), where the damage variable is defined in Equation (2.37).

Basically, before delamination appeared, the interaction was considered to have a linear behavior, once the damage criterion was satisfied, the cohesive stiffness degrades exponentially. According to Eliasson and Lundberg (2015) using an exponential softening model, the calculations are perceived to converge faster. The linear softening has a good convergence as well but not as good. The fracture energy of the cohesive surface is evaluated under mode I, mode II, or mixed-mode, according to the BK law (Benzeggagh and Kenane, 1996).

The initial stiffness K is set to maintain the continuity of the stress and strain fields between fibers and matrix. The traction-separation behavior is assumed to be uncoupled, i.e., all non-diagonal terms of the elasticity matrix in Equation (2.29) are null and the diagonal terms are assumed to be equal, ($K_{11} = K_{22} = K_{33}$). The values of the interface fracture energies $\mathcal{G}_{I_C}$, $\mathcal{G}_{II_C}$ and $\mathcal{G}_{III_C}$ that are used in the next chapter are justified not only by experimental evidence (Varna et al., 1997), but also from previous micro-mechanical numerical analysis, (Melro et al. (2013b) and Vaughan and McCarthy (2011)), which have demonstrated that the brittle behavior in transverse tension typical of composites is only captured for such low values of interfacial toughness (Arteiro et al., 2014).

Chapter 5

Numerical Simulations - Interlaminar Damage

This chapter is dedicated to the numerical simulations of single (I or II) and mixed-mode delamination on Abaqus®. It is analyzed the ply orientation of (0°/0°) and (0°/90°) for each hybrid model (DCB, ENF and MMB). However, the results presented are much more qualitative, rather than quantitative.

The purpose of these simulations reside on the analyze and evaluation of the degradation of the material of the epoxy matrix. The FE models consist of five main parts, namely a micro-mechanical two oriented ply RVE, composed by the fibers and matrix, and three homogenized parts. Each ply is composed by a random distribution of fibers generated using the algorithm presented in Chapter 3.

Table 5.1: Homogenized parts properties

Material property	Value
Young's moduli	
E_{11} (MPa)	171420
E_{22} (MPa)	9090
Poisson's ratio	
ν_{12}	0.32
Shear moduli	
G_{12} (MPa)	5290
G_{23} (MPa)	4000
Density	
ρ (kg.mm^{-3})	1.6×10^{-9}

The homogenized parts are intended to simulate the mesoscopic elastic behavior of the RVE and are assumed to be of a IM7/8552 carbon-epoxy composite, as the corresponding material properties are available in several publications (Wisnom et al. (2008) or Camanho and Lambert (2006)). These parts are homogenized in order to simplify the computational time. Table 5.1 shows the relevant material properties.

A simple transversely isotropic, linear-elastic constitutive model is used to simulate the individual reinforcing carbon fibers. The diameter of the individual fibers is considered constant in the entire RVE and the fiber volume fraction is the same in all of the simulations. Table 5.2 shows the material properties of standard carbon fibers used in the present models.

The material and damage behavior of the matrix is based on the model presented in Section 4.1, with the damage variable defined in Equation (4.32). This model is implemented on a VUMAT routine. The material properties of the epoxy matrix are presented in Table 5.3.

Table 5.2: Fiber material properties

Material property	Value
Fiber diameter $2r$ (mm)	0.0035
Fiber volume fraction v_f %	70
Young's moduli E_{11} (MPa) E_{22} (MPa)	276000 15000
Poisson's ratio ν_{12}	0.2
Shear moduli G_{12} (MPa) G_{23} (MPa)	15000 7000
Density ρ (kg.mm^{-3})	1.78×10^{-9}

Table 5.3: Matrix material properties

Material property	Value
Young's modulus E (MPa)	3760
Poisson's ratio ν	0.39
Coefficient of thermal expansion α ($^{\circ}C^{-1}$)	58×10^{-6}
Plastic Poisson's ratio ν_p	0.3
Tension failure stress X^t (MPa)	94.9
Compression failure stress X^c (MPa)	220
Fracture toughness $\mathcal{G}_C$ (N/mm)	0.09
Density ρ (kg.mm^{-3})	1.3×10^{-9}

The interface between fiber and matrix is modeled using the cohesive surfaces of the FE commercial software Abaqus® and the properties are presented in Table 5.4.

Table 5.4: Fiber/matrix interface properties

Material property	Value
Interface stiffness	
K (N/mm^3)	10^8
Friction coefficient	
μ_τ	0.3
Interface maximum strengths	
τ_0^1 (MPa)	75
τ_0^2 (MPa)	75
τ_0^3 (MPa)	50
Interface critical energy release rates	
$\mathcal{G}_{I_C}$ (N/mm)	0.002
$\mathcal{G}_{II_C}$ (N/mm)	0.006
$\mathcal{G}_{III_C}$ (N/mm)	0.006
Mixed-mode interaction parameter*	
η	1.45

*BK law (Benzeggagh and Kenane, 1996)

For these analysis, the RVE composed by two plies has a width and a height of 105 μm and 71 μm, respectively.

The Figures that involve the degradation of the epoxy matrix evaluate a variable named SDV3. This variable represents the damage variable defined in Equation (4.32).

5.1 DCB

The displacement applied to the model is presented in Figure 5.1.

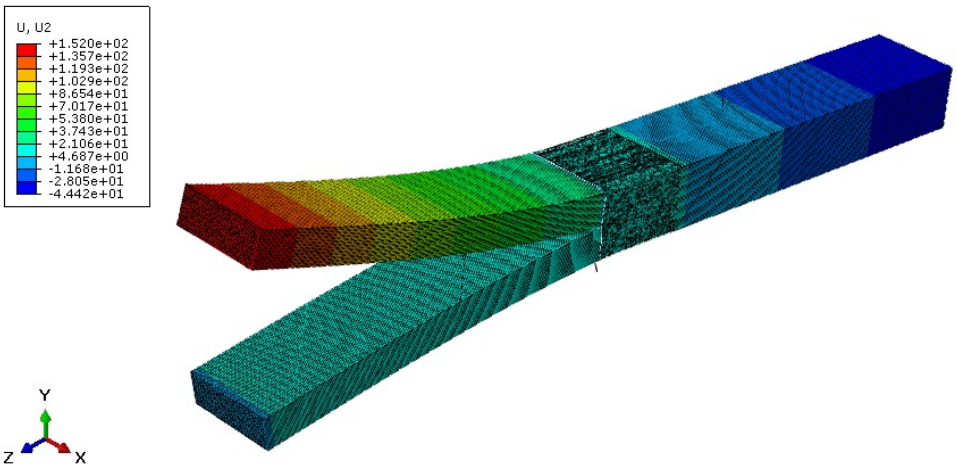

Figure 5.1: Displacement applied to the DCB model.

5.1.1 0°/0°

In the DCB model, the delamination front can be easily identified. Figures 5.2 - 5.3 represent the evolution of damage in the matrix for a relative displacement ($d_r = \Delta/h$, where Δ is the applied displacement) of approximately 0.45 and 0.9, respectively. This relative displacement represents the displacement divided by the height of a single ply of the RVE.

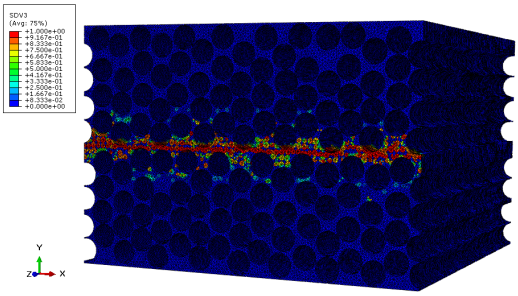

Figure 5.2: DCB - Damage at $d_r = 0.45$.

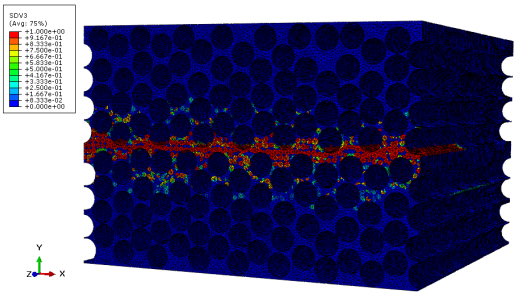

Figure 5.3: DCB - Damage at $d_r = 0.9$.

Figure 5.2 represents the initiation of interlaminar damage propagation, corresponding to the development of damage in the matrix at the crack tip. In Figure 5.3 the delamination front becomes clear, propagating stably along the resin rich area at the interface between plies.

5.1.2 0°/90°

Figures 5.4 - 5.8 represent the evolution of damage in the matrix for relative displacements of approximately 0.2, 0.31, 0.48, 1.15 and 2.17, respectively. For this case, a crack migration process starting from the initial crack tip can be observed (Figure 5.4). The interface between plies remains practically intact, as the interlaminar crack deflects towards the 90° ply, conducting to intralaminar crack propagation.

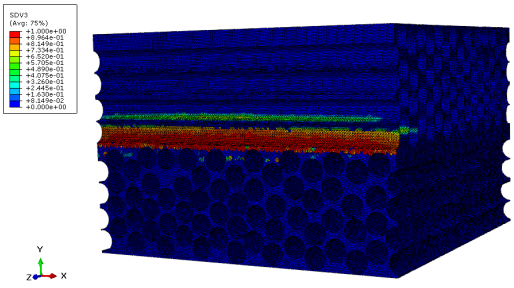

Figure 5.4: DCB - Damage at $d_r = 0.2$.

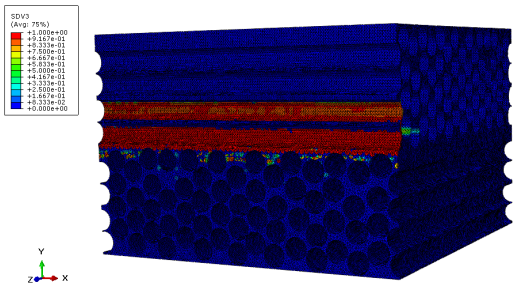

Figure 5.5: DCB - Damage at $d_r = 0.31$.

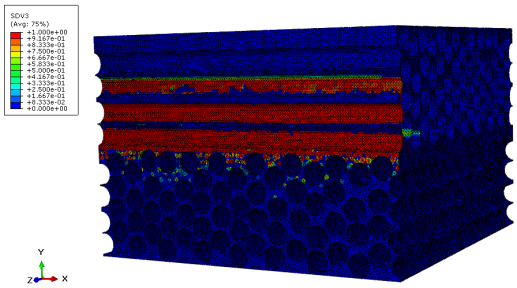

Figure 5.6: DCB - Damage at $d_r = 0.48$.

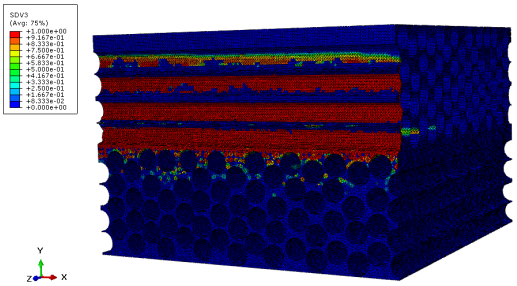

Figure 5.7: DCB - Damage at $d_r = 1.15$.

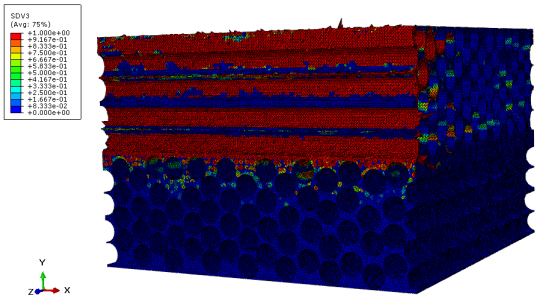

Figure 5.8: DCB - Damage at $d_r = 2.01$.

5.2 ENF

The displacement applied to the model is presented in Figure 5.9.

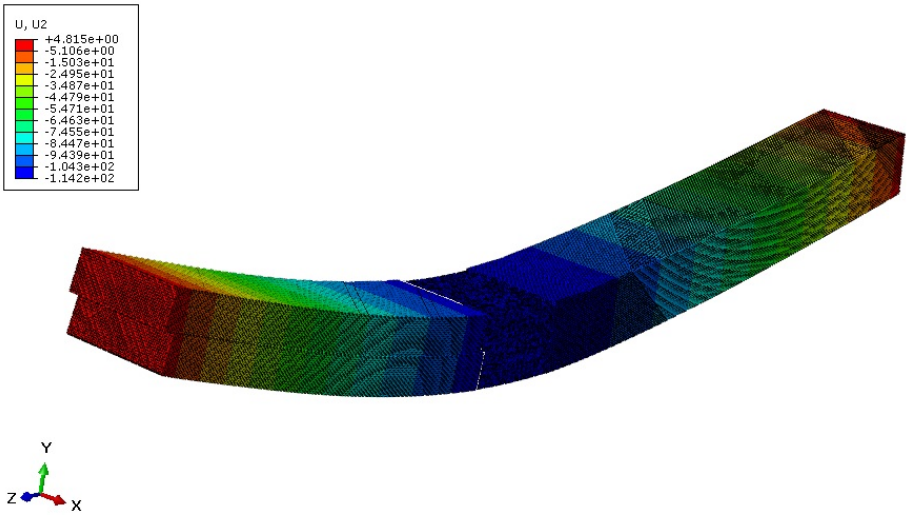

Figure 5.9: Displacement applied to the ENF model.

5.2.1 0°/0°

Figures 5.10 - 5.12 represent the evolution of damage in the matrix for a relative displacement of approximately 0.21, 0.45 and 0.65.

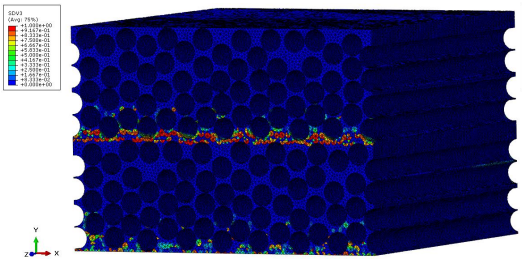

Figure 5.10: ENF - Damage at $d_r = 0.21$.

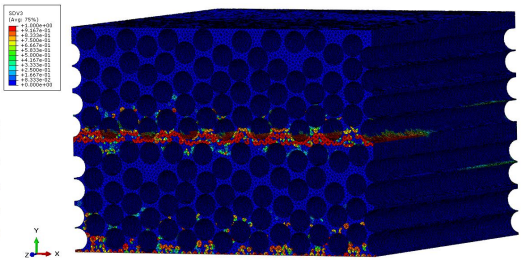

Figure 5.11: ENF - Damage at $d_r = 0.45$.

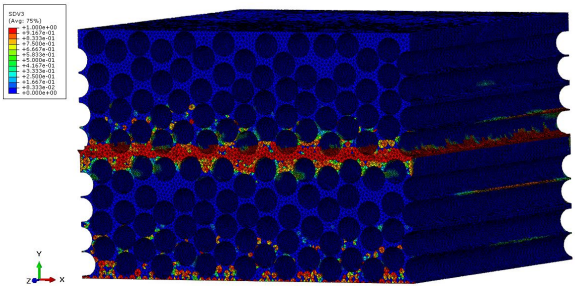

Figure 5.12: ENF - Damage at $d_r = 0.65$.

Figure 5.10 shows the initiation of damage in the matrix, corresponding to the onset of delamination propagation. The interlaminar crack propagates stably along the fiber direction until complete penetration of the interlaminar region (Figures 5.11 - 5.12).

5.2.2 0°/90°

Figures 5.13 - 5.17 show the evolution of damage in the matrix for a relative displacement of approximately 0.45, 0.9, 1.2, 1.46 and 2.53. In this case, the delamination deflects from the interlaminar region, conducting to intralaminar crack propagation at the 90° ply.

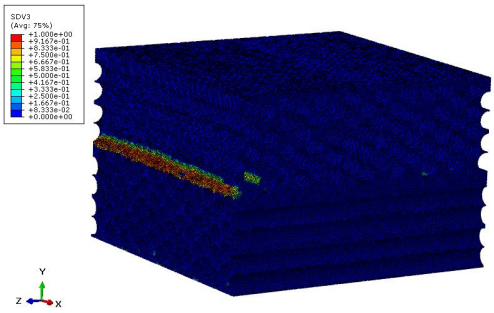

Figure 5.13: ENF - Damage at $d_r = 0.45$.

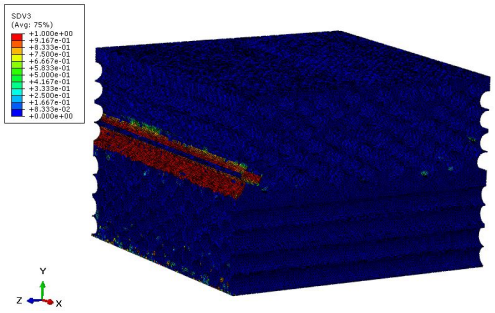

Figure 5.14: ENF - Damage at $d_r = 0.9$.

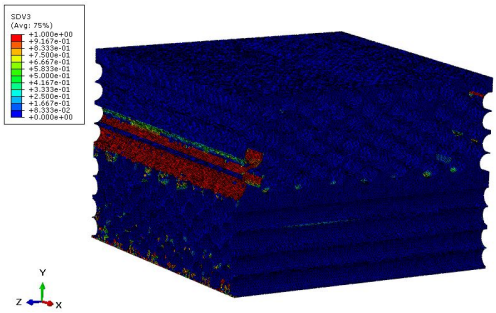

Figure 5.15: ENF - Damage at $d_r = 1.2$.

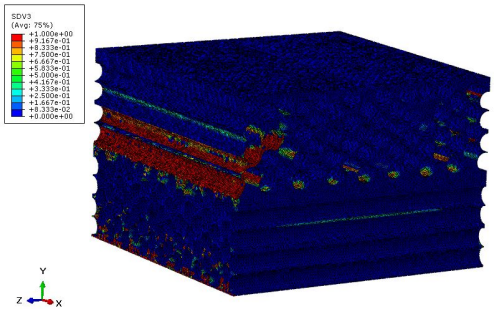

Figure 5.16: ENF - Damage at $d_r = 1.46$.

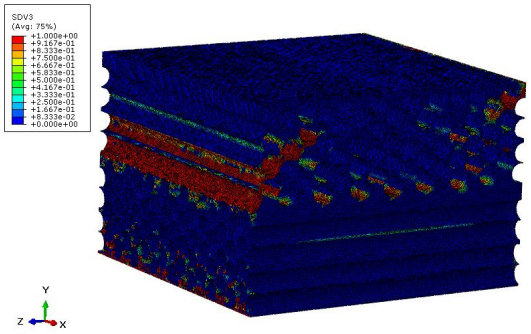

Figure 5.17: ENF - Damage at $d_r = 2.53$.

5.3 MMB

The displacement applied to the model is presented in Figure 5.18.

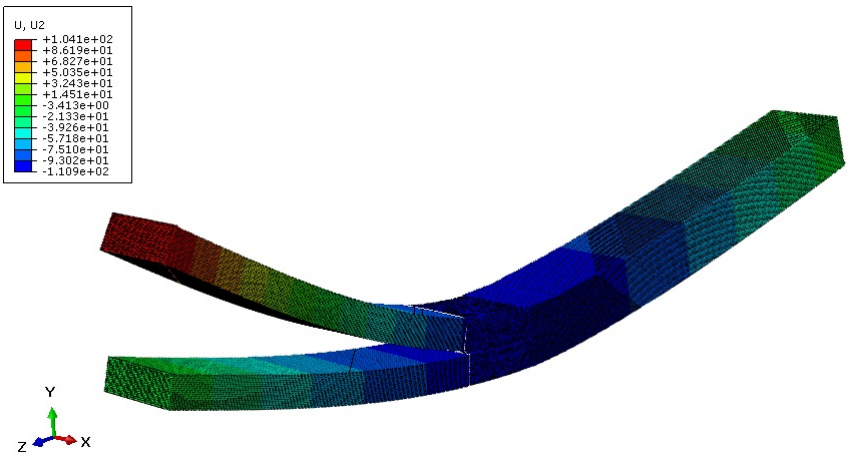

Figure 5.18: Displacement applied to the MMB model.

5.3.1 0°/0°

Figures 5.19 - 5.21 represent the evolution of damage in the matrix for a relative displacement of approximately 0.2, 0.45 and 0.7. Interlaminar cracking initiates at the initial crack tip, forming a delamination front that extends through the interlaminar region along the fiber direction.

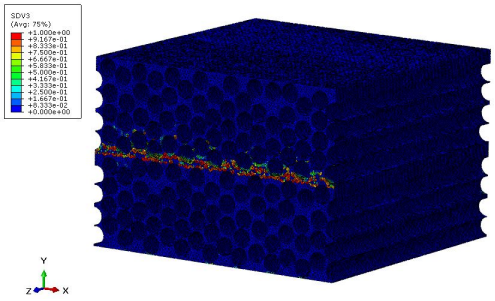

Figure 5.19: MMB - Damage at $d_r = 0.2$.

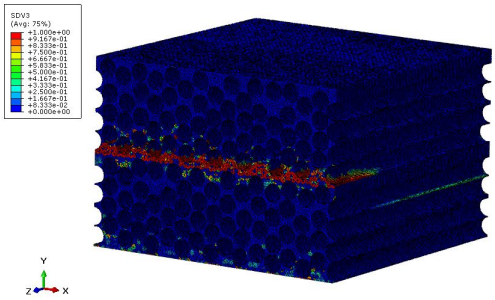

Figure 5.20: MMB - Damage at $d_r = 0.45$.

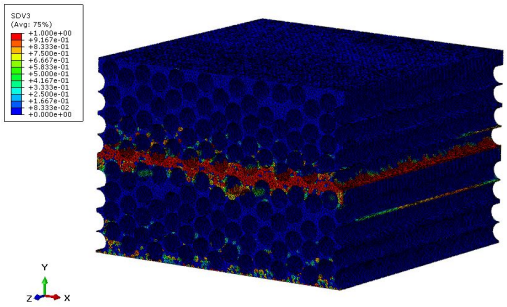

Figure 5.21: MMB - Damage at $d_r = 0.7$.

5.3.2 0°/90°

Figures 5.22 - 5.26 show the evolution of damage in the matrix for a relative displacement of approximately 0.4, 0.82, 0.96, 1.23 and 1.94. A fracture migration process is observed, with the interlaminar crack deflecting towards the 90° ply, forming an intralaminar crack.

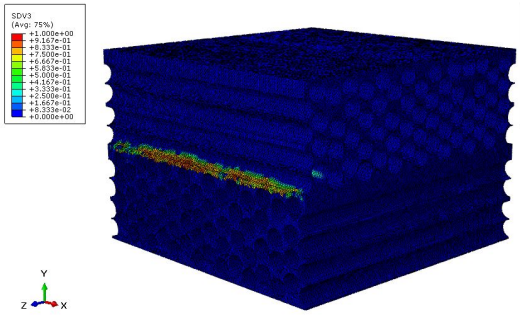

Figure 5.22: MMB - Damage at $d_r = 0.4$.

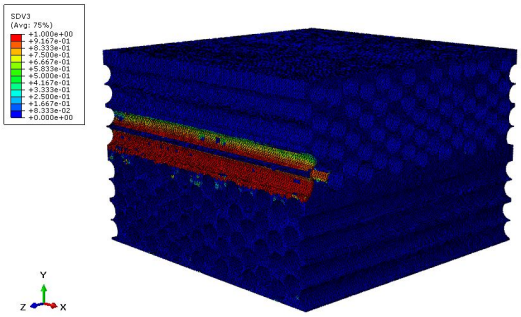

Figure 5.23: MMB - Damage at $d_r = 0.82$.

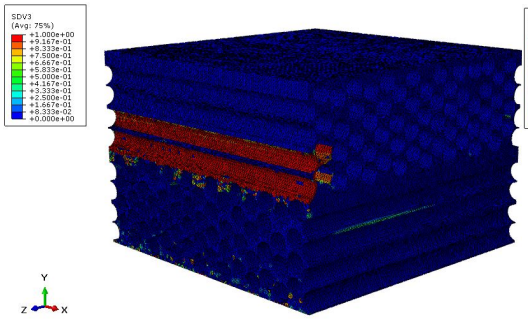

Figure 5.24: MMB - Damage at $d_r = 0.96$.

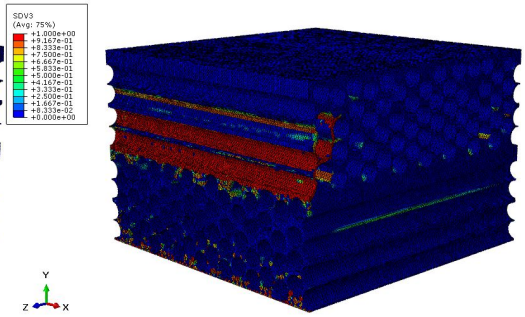

Figure 5.25: MMB - Damage at $d_r = 1.23$.

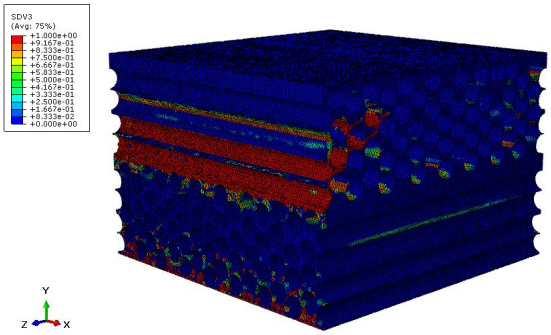

Figure 5.26: MMB - Damage at $d_r = 1.94$.

Chapter 6

Conclusions and Future Work

This chapter is intended to summarize the main conclusions of the thesis, as well as to recommend future work to improve the understanding of interlaminar fracture mechanisms using computational micro-mechanics.

6.1 Conclusions

With the objective of studying the sequence of mechanisms leading to interlaminar failure in composite materials, a micro-mechanical model was developed to represent single- and mixed-mode delamination models at the micro-scale.

First, a special focus is given to delamination. A review of the different experimental tests for evaluating the interlaminar fracture toughness was given, as well as the analysis and evaluation of damage between the interfaces of the constituents. An overview of micro-mechanical modeling was given by introducing some concepts about the different modeling scales, Representative Volume Elements, homogenization and hybrid models. A literature review of the different response of epoxy resins in the plastic domain was also presented.

An algorithm capable of generating bi-dimensional RVEs with a random distribution of fibers was proposed. Lateral geometrical boundary periodicity is imposed so that periodic boundary conditions can be applied on the representative volume elements generated. Using this algorithm, it was possible to develop a sequential and automatic procedure to generate not only the random fiber distributions, but also a complete three-dimensional single- or double-ply RVE, as well as the addition of parts that represent the mesoscopic behavior of the RVE, in order to have hybrid models that simulate single- (DCB and ENF) and mixed-mode (MMB) delamination.

The analytical definition and description of the damage and material models of the constituents and interfaces between them were describe. The elastic-plastic with a damage model applied to the matrix followed the work of Melro et al. (2013a) and included the ability to capture the thermal and strain-rate dependency, following Bai et al. (2015). Because the objective was to model interlaminar damage, were assumed to be linear-elastic. The interface between the constituents was modeled using cohesive surfaces implemented in an FE commercial software. The damage

initiation was monitored by the quadratic stress criterion and the damage evolution was modeled using an exponential traction-separation law.

The simulations performed showed that the models proposed for the single- and mixed-mode delamination are capable of representing the interlaminar damage propagation, in the direction of the fibers, throughout the interface between layers with the same orientation (i.e. 0°/0°). The models are as well capable of representing the process of interlaminar crack migration from the interface between layers with different orientations (e.g. 0°/90°) through the development of intralaminar cracks in the epoxy matrix.

6.2 Future work

This thesis presented a development on the modeling of the interlaminar failure of polymer composites, however, there are still developments to be made, either in terms of the micro-mechanical modeling or in terms of experimental validation.

Since the algorithm developed is able to generate RVEs with other orientations rather than the ones that have been discussed in Chapter 5, in the future, it is intended to study and model the mechanisms that originate the appearance of the crack migration phenomenas, by changing the orientation of the fibers and by changing the dimensions of the RVE. It is also important to study the effect of the properties and nature of the constituents (e.g. thermoset vs thermoplastic matrix), the effect of the fiber volume fraction, the effect of the introduction of toughening systems (e.g. particles, stitching, etc.), the introduction of more complex stress states in the model besides single mode or mixed-mode, as well as the study of potential strategies that prevent or restrict migration phenomena.

The interface between the fibers and the matrix greatly affects the performance and behavior of composite materials. This interface was represented using cohesive surfaces in the micro-mechanical models, however, it is necessary to gather more information in relation to the properties of the interfaces to guarantee a correct modeling of this constituent.

Since voids are a typical defect that can occur during the fabrication of composite materials, it is important to consider their contribution to the degradation of the material. In the future, it is intended to study interlaminar fracture mechanisms, but considering voids inside the representative volume element and evaluate how the increase in porosity changes the mechanical properties.

The generation of the hybrid models did not take into account all dimensional characteristics of the delamination test methods. In the future there is the interest to study the space introduced by the teflon sheet affects the numerical results.

In addition to the virtual tests based on computational micro-mechanics, future work should also include detailed experimental studies to help understanding the failure mechanisms and the controlling factors that govern interlaminar fracture and its interaction with other failure mechanisms.

Bibliography

ABAQUS (2011). ABAQUS 6.11 Document. © Dassault Systemes, IV.

Alberti, M., Enfedaque, A., Gálvez, J., and Ferreras, A. (2016). Pull-out behaviour and interface critical parameters of polyolefin fibres embedded in mortar and self-compacting concrete matrixes. Construction and Building Materials, 112:607–622.

Anderson, T. L. (2012). Fracture Mechanics: Fundamentals and Applications, volume 58.

Andersons, J. and Konig, M. (2004). Dependence of fracture toughness of composite laminates on interface ply orientations and delamination growth direction. Composites Science and Technology, 64(13-14):2139–2152.

Arteiro, A., Catalanotti, G., Melro, A. R., Linde, P., and Camanho, P. P. (2014). Micro-mechanical analysis of the in situ effect in polymer composite laminates. Composite Structures, 116(1):827–840.

Arteiro, A., Catalanotti, G., Melro, A. R., Linde, P., and Camanho, P. P. (2015). Composites : Part A Micro-mechanical analysis of the effect of ply thickness on the transverse compressive strength of polymer composites. COMPOSITES PART A, 79:127–137.

Asp, L. E., Berglund, L. A., and Gudmundson, P. (1995). Effects of a composite-like stress state on the fracture of epoxies. Composites Science and Technology, 53(1):27–37.

Asp, L. E., Berglund, L. A., and Talreja, R. (1996). A criterion for crack initiation in glassy polymers subjected to a composite-like stress state. Composites Science and Technology, 56(11):1291–1301.

Bai, X., Bessa, M. A., Melro, A. R., Camanho, P. P., Guo, L., and Liu, W. K. (2015). High-fidelity micro-scale modeling of the thermo-visco-plastic behavior of carbon fiber polymer matrix composites. Composite Structures, 134:132–141.

Bakis, C. E. (2013). Proceedings of the American Society for Composites. pages 713–715. State College, PA, Pennsylvania.

Benzeggagh, M. L. and Kenane, M. (1996). Measurement of mixed-mode delamination fracture toughness of unidirectional glass/epoxy composites with mixed-mode bending apparatus. Composites Science and Technology, 56(4):439–449.

Böhm, H. J. (2004). A Short Introduction to Continuum Micromechanics, pages 1–40. Springer Vienna, Vienna.

Camanho, P. and Davila, C. (2002). Mixed-Mode Decohesion Finite Elements in for the Simulation Composite of Delamination Materials. Nasa, TM-2002-21(June):1–37.

Camanho, P. P. and Lambert, M. (2006). A design methodology for mechanically fastened joints in laminated composite materials. Composites Science and Technology, 66(15):3004–3020.

Carlsson, L., Gillespie, J., and Pipes, R. (1986). On the Analysis and Design of the End Notched Flexure (ENF) Specimen for Mode II Testing. Journal of Composite Materials, 20(6):594–604.

Catalanotti, G. (2016). On the generation of RVE-based models of composites reinforced with long fibres or spherical particles. Composite Structures, 138:84–95.

Charalambides, M. N., Olusanya, A. (1997). The Constitutive Models Suitable for Adhesives in some Finite Element Codes and Suggested Methods of Generating the Appropriate Materials Data The Constitutive Models Suitable for Adhesives in some Finite Element Codes and Suggested Methods of Generating. Measurement, (April):1–33.

Cook, A. M. (2001). Characterization of Interlaminar Fracture in Composite Materials - A Case Study Appr PhD thesis, Montana State University - Bozeman.

Cui, W. C., Wisnom, M. R., and Jones, M. (1992). A comparison of failure criteria to predict delamination of unidirectional glass/epoxy specimens waisted through the thickness. Composites, 23(3):158–166.

De Morais, A. B. (2003). Double cantilever beam testing of multidirectional laminates. Composites Part A: Applied Science and Manufacturing, 34(12):1135–1142.

de Moura, M. F. S. F., Silva, M. A. L., de Morais, A. B., and Morais, J. J. L. (2006). Equivalent crack based mode II fracture characterization of wood. Engineering Fracture Mechanics, 73(8):978–993.

de Souza Neto, E., Peric, D., and Owen, D. R. J. (2008). Computational Methods for Plasticity, volume 55.

Della, C. N. and Shu, D. (2007). Vibration of Delaminated Composite Laminates: A Review. Applied Mechanics Reviews, 60(1):1.

Donaldson, S. L. (1988). Mode III interlaminar fracture characterization of composite materials. Composites Science and Technology, 32(3):225–249.

Drzal, L., Madhukar, M., and Waterbury, M. (1992). Proceeding of the Adhesion Society, 15th Annual Meeting. page 144.

Duncan, B. C., Dean, G. D., and Read, B. E. (1998). Project PAJ2 Dynamic Performance of Adhesively Bonded Joints Report No 4 , January 1998 Prediction of the Performance of Adhesives Under Impact Loading. (4).

Eliasson, S. and Lundberg, A. (2015). Investigation and Comparison of Cohesive Zone Models for Simulation of Crack Propagation.

Fiedler, B., Hojo, M., Ochiai, S., Schulte, K., and Ando, M. (2001). Failure behavior of an epoxy matrix under different kinds of static loading. Composites Science and Technology, 61(11):1615–1624.

Fu, S. Y., Feng, X. Q., Lauke, B., and Mai, Y. W. (2008). Effects of particle size, particle/matrix interface adhesion and particle loading on mechanical properties of particulate-polymer composites. Composites Part B: Engineering, 39(6):933–961.

Garg, A. C. (1988). Delamination-a damage mode in composite structures. Engineering Fracture Mechanics, 29(5):557–584.

Ghorbel, E. (2008). A viscoplastic constitutive model for polymeric materials. International Journal of Plasticity, 24(11):2032–2058.

Greenhalgh, E. S., Rogers, C., and Robinson, P. (2009). Fractographic observations on delamination growth and the subsequent migration through the laminate. Composites Science and Technology, 69(14):2345–2351.

Gusev, A. A., Hine, P. J., and Ward, I. M. (2000). Fiber packing and elastic properties of a transversely random unidirectional glass/epoxy composite. Composites Science and Technology, 60(4):535–541.

Hallett, S. R., Green, B. G., Jiang, W. G., and Wisnom, M. R. (2009). An experimental and numerical investigation into the damage mechanisms in notched composites. Composites Part A: Applied Science and Manufacturing, 40(5):613–624.

Hashin, Z. (1983). Analysis of Composite Materials.

He, M.-Y., Bartlett, A., Evans, A. G., and Hutchinson, J. W. (1991). Kinking of a Crack out of an Interface: Role of In-Plane Stress. Journal of the American Ceramic Society, 74(4):767–771.

Hill, R. (1963). Elastic properties of reinforced solids: Some theoretical principles. Journal of the Mechanics and Physics of Solids, 11(5):357–372.

Hill, R. (1964). Theory of mechanical properties of fibre-strengthened materials: I. Inelastic behaviour. Journal of the Mechanics and Physics of Solids, 12(4):213–218.

Hojo, M., Matsuda, S., Tanaka, M., Ochiai, S., and Murakami, A. (2006). Mode I delamination fatigue properties of interlayer-toughened CF/epoxy laminates. Composites Science and Technology, 66(5):665–675.

Hu, N. (2006). Identification of Delaminations in Composite Laminates. Journal of Intelligent Material Systems and Structures, 17(8-9):671–683.

Hu, N., Shimomukai, T., Yan, C., and Fukunaga, H. (2008). Identification of delamination position in cross-ply laminated composite beams using S0 Lamb mode. Composites Science and Technology, 68(6):1548–1554.

Hu, X. and Duan, K. (2008). Size effect and quasi-brittle fracture: The role of FPZ. International Journal of Fracture, 154(1-2):3–14.

Huang, Y. and Kinloch, A. J. (1992). The sequence of initiation of the toughening micromechanisms in rubber-modified epoxy polymers. Polymer, 33(24):5338–5340.

Joseph, T., Sun, F., and Rogers, C. (1996). Local-area health monitoring of aircraft via piezoelectric actuator/sensor patches. SPIE: Smart Structures and Materials, 2443:268–276.

Launey, M. E. and Ritchie, R. O. (2009). On the fracture toughness of advanced materials. Advanced Materials, 21(20):2103–2110.

Lee, S. (1997). Mode II delamination failure mechanisms of polymer matrix composites. Journal of materials science, 2:1287–1295.

Malvern, L. (1969). Introduction to the Mechanics of a Continuos Medium. Engineering if the Physical Sciences, 33(1):238.

Martin, E., Peters, P. W. M., Leguillon, D., and Quenisset, J. M. (1998). Conditions for matrix crack deflection at an interface in ceramic matrix composites. Materials Science and Engineering A, 250(2):291–302.

Mascarenhas, W. N., Ahrens, C. H., and Ogliari, A. (2004). Design criteria and safety factors for plastic components design. Materials and Design, 25(3):257–261.

MATLAB (2015). version 8.5.1 (R2015a). The MathWorks Inc., Natick, Massachusetts.

Matsuda, T., Ohno, N., Tanaka, H., and Shimizu, T. (2003). Effects of fiber distribution on elastic-viscoplastic behavior of long fiber-reinforced laminates. International Journal of Mechanical Sciences, 45(10):1583–1598.

Melro, A. R., Camanho, P. P., Andrade Pires, F. M., and Pinho, S. T. (2013a). Micromechanical analysis of polymer composites reinforced by unidirectional fibres: Part I-Constitutive modelling. International Journal of Solids and Structures, 50(11-12):1897–1905.

Melro, A. R., Camanho, P. P., Andrade Pires, F. M., and Pinho, S. T. (2013b). Micromechanical analysis of polymer composites reinforced by unidirectional fibres: Part II-Micromechanical analyses. International Journal of Solids and Structures, 50(11-12):1906–1915.

Melro, A. R., Camanho, P. P., and Pinho, S. T. (2008). Generation of random distribution of fibres in long-fibre reinforced composites. Composites Science and Technology, 68(9):2092–2102.

Miller, B., Muri, P., and Rebenfeld, L. (1987). A Microbond Method for Determination of the Shear Strength of a Fiber/ Resin Interface. Composites Science and Technology, 28(1):17–32.

Ming-Yuan He and Hutchinson, J. W. (1988). Crack deflection at an interface between dissimilar elastic materials. International Journal of Fracture, 102(4):355–370.

Nemat-Nasser, S., Lori, M., and Datta, S. K. (1996). Micromechanics: Overall Properties of Heterogeneous Materials. Journal of Applied Mechanics, 63:561.

Oh, Z. B. and B. (1983). Crack band theory for fracture of concrete.

Pagano, N. J. and Brown, H. W. (1993). The full-cell cracking mode in unidirectional brittle-matrix composites. Composites, 24(2):69–83.

Parthasarathy, T. A., Jefferson, G. J., and Kerans, R. J. (2007). Analytical evaluation of hybrid ceramic design concepts for optimized structural performance. Materials Science and Engineering A, 459(1-2):60–68.

Pasquali, M. and Lacarbonara, W. (2015). Delamination detection in composite laminates using high-frequency P- and S-waves - Part I: Theory and analysis. Composite Structures, 134:1095–1108.

Penn, L. S., Jump, J. R., Greenfield, M. J., and Blandford, G. E. (1999). Use of the Free Vibration Spectrum to Detect Delamination in Thick Composites. Journal of Composite Materials, 33(1):54–72.

Pernice, M. F., De Carvalho, N. V., Ratcliffe, J. G., and Hallett, S. R. (2015). Experimental study on delamination migration in composite laminates. Composites Part A: Applied Science and Manufacturing, 73:20–34.

Reeder, J. R. and Crews, J. H. (1990). Mixed-Mode Bending Method for Delamination Testing. Aiaa Journal, 28(7):1270–1276.

Robinson, P. and Song, D. Q. (1994). The development of an improved mode III delamination test for composites. Composites Science and Technology, 52(2):217–233.

Rui Melro, A. (2011). Analytical and Numerical Modelling of Damage and Fracture of Advanced Composites. (February):1–316.

Scheibe, T. D., Tartakovsky, a. M., Tartakovsky, D. M., Redden, G. D., and Meakin, P. (2007). Hybrid numerical methods for multiscale simulations of subsurface biogeochemical processes. Journal of Physics: Conference Series, 78:012063.

Sela, I. V. and Ishai, O. (1989). Interlaminar fracture toughness and toughening of laminated composite materials : a review. Composites, 20(5):423–435.

Shang, S., Yun, G. J., and Qiao, P. (2010). Delamination identification of laminated composite plates using a continuum damage mechanics model and subset selection technique. Smart Materials and Structures, 19(5):055024.

Sharif, F., Kortschot, M. T., and Martin, R. H. (1995). Mode III delamination using a split cantilever beam. (1230):85–99.

Singh, S. and Partridge, I. K. (1995). Mixed-mode fracture in an interleaved carbon-fibre/epoxy composite. Composites Science and Technology, 55(4):319–327.

Staszewski, W. J., Lee, B. C., Mallet, L., and Scarpa, F. (2004). Structural health monitoring using scanning laser vibrometry: I. Lamb wave sensing. Smart Materials and Structures, 13(2):251–260.

Tschoegl, N. W. (1971). Failure surfaces in principal stress space. Journal of polymer science Part C: Polymer symposia, 32(1):239–267.

Varna, J., Berglund, L. A., and Ericson, M. L. (1997). Transverse single-fibre test for interfacial debonding in composites: 2. Modelling. Composites Part A: Applied Science and Manufacturing, 28(4):317–326.

Vaughan, T. J. and McCarthy, C. T. (2011). Micromechanical modelling of the transverse damage behaviour in fibre reinforced composites. Composites Science and Technology, 71(3):388–396.

Wagner, H. D. and Lustiger, A. (1994). Effect of water on the mechanical adhesion of the glass/epoxy interface. Composites, 25(7):613–616.

Wagner, H. D., Nairn, J. A., and Detassis, M. (1995). Toughness of interfaces from initial fiber-matrix debonding in a single fiber composite fragmentation test. Applied Composite Materials: An International Journal for the Science and Application of Composite Materials, 2(2):107–117.

Wisnom, M. R., Khan, B., and Hallett, S. R. (2008). Size effects in unnotched tensile strength of unidirectional and quasi-isotropic carbon/epoxy composites. Composite Structures, 84(1):21–28.

Wongsto, A. and Li, S. (2005). Micromechanical FE analysis of UD fibre-reinforced composites with fibres distributed at random over the transverse cross-section. Composites Part A: Applied Science and Manufacturing, 36(9):1246–1266.

Wu, E. M. and Reuter Jr., R. C. (1965). Crack Extension in Fiberglass Reinforced Plastics. Sponsored by US Bureau of Naval Weapons, Report No. 275, Illinois University at Urbana Dept. of Theoretical and Applied Mechanics, (2):32.

Yasaee, M., Bond, I. P., Trask, R. S., and Greenhalgh, E. S. (2012). Mode II interfacial toughening through discontinuous interleaves for damage suppression and control. Composites Part A: Applied Science and Manufacturing, 43(1):121–128.

Ye, Y., Chen, H., Wu, J., Chan, C., and Ye, L. (2010). Properties of advanced fiber composites with halloysite nanotube toughened epoxy matrix. No info, (August).

Yuan, Z., Li, F., Zhang, P., Chen, B., and Xue, F. (2014). Mechanical properties study of particles reinforced aluminum matrix composites by micro-indentation experiments. Chinese Journal of Aeronautics, 27(2):397–406.

Zamanian, M., Mortezaei, M., Salehnia, B., and Jam, J. E. (2013). Fracture toughness of epoxy polymer modified with nanosilica particles: Particle size effect. Engineering Fracture Mechanics, 97(1):193–206.

Zhandarov, S. and Mader, E. (2005). Characterization of fiber/matrix interface strength: Applicability of different tests, approaches and parameters. Composites Science and Technology, 65(1):149–160.

Zhandarov, S. F., Pisanova, E. V., and Dovgyalo, V. A. (1992). Fragmentation of a single filament during tension in a matrix as a method of determining adhesion. Mechanics of Composite Materials, 28(3):270–286.

Zuev, V. V. (2012). The mechanisms and mechanics of the toughening of epoxy polymers modified with fullerene C60. Polymer Engineering and Science, 52(12):2518–2522.

Appendix A

MATLAB® Script for Generation of 2D RVEs

Appendix A contains the code of the MATLAB® script that creates 2D RVEs for a single ply.

As it has been previously said, the script is fast an can be used to generate random distribution of fibers according to the dimensions of the RVE and the input of fiber volume fraction. Section (3.1.1) details its flowchart and input variables.

The whole script has one main file named "bidim_RVE.m", a function that checks if the fibers are interpenetrating named "distance_lamina.m" and another functions such as "vline.m", "hline.m" and "circle.m". All these three functions were downloaded from the reference MATLAB (2015).

A folder named "Matlab" with the files can be found on the CD attached.

Appendix B

PYTHON Scripts for Generation of 3D RVEs & Hybrid Models

Appendix B contains the codes used in the developed PYTHON script that uses the outputs of the previously developed algorithm, namely the overall variables and the coordinates of each fiber to create a 3D RVE with a desired orientation. The algorithms are to be used on the commercial software Abaqus®.

The first algorithm named "threedim_RVE.py" is capable of generating RVEs that represent a single ply of a composite with a desired orientation from 0° to 180°. The algorithm is detailed in section 3.1.2.

The second algorithm named "hybrid_model.py" is capable of generating RVEs with $-\theta^\circ/\theta^\circ$ ply orientation, as well as the homogenized parts in order to model the double cantilever beam, end notched flexure or the mixed mode bending experimental test.

These algorithms are able to identify all the surfaces needed to complete the model, such as the locations to apply all the boundary conditions, all the fibers-matrix interfaces, and is capable to generate the mesh for all the parts in the assembly, with a desired size for the elements in cause.

A folder named "Python" with the files can be found on the CD attached.